A peridynamic model for sleeved hydraulic fracture

by
Carel Wagener van der Merwe

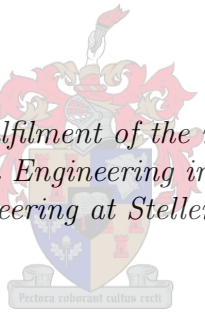

Thesis represented in fulfilment of the requirements for the degree of Master in Engineering in the Faculty of Civil Engineering at Stellenbosch University

Supervisor: Dr D.Z. Turner
Co-supervisor: Dr J.A.vB. Strasheim

December 2014

Declaration of Authorship

By submitting this thesis electronically, I declare that the entirety of the work contained therein is my own, original work, that I am the authorship owner thereof (unless to the extent explicitly otherwise stated) and that I have not previously in its entirety or in part submitted it for obtaining any qualification.

Signed:

_____

Date:

_____

Abstract

Current numerical methods in the field of hydraulic fracturing are based mainly on continuum methods, such as the Finite Element Method (FEM) and the Boundary Element Method (BEM). These methods are governed by Linear Elastic Fracture Mechanics (LEFM) criteria, which suffer from the inherent flaw of a non-physical stress representation at the fracture tip. In response to this, a non-local method is proposed, namely the peridynamic theory, to model sleeved hydraulic fracture. A 2D implicit quasi-static ordinary state based peridynamic formulation is implemented on various benchmark problems, to verify the ability to capture constitutive behaviour in a linear elastic solid, as well as, the quantification of adverse effects on the accuracy of the displacement solution, due to the nature of the non-local theory. Benchmark tests consist of a plate in tension, where convergence to the classical displacement solution, non-uniform refinement and varying cell sizes are tested, as well as, a thick walled cylinder with internal pressure, where three different loading techniques are tested. The most accurate loading technique is applied to the sleeved fracture model, in order to simulate fracture initiation and propagation. This model is then verified and validated by using the Rummel & Winter hydraulic fracturing model and experimental results, respectively. Displacement error minimisation methods are implemented and as a result, the displacement solutions for a plate in tension converges to the analytical solution, while the thick walled cylinder solutions suffer from inaccuracies due to an applied load on an irregularly discretized region. The fracture initiation test captures the fracture tip behaviour of the Rummel & Winter model and the fracture propagation test show good correlation with experimental results. This research shows that the peridynamic approach to sleeved hydraulic fracture can yield a realistic representation of fracture initiation and propagation, however, further research is needed in the area of a pressure load application on a solid using the peridynamic approach.

Opsomming

Huidige numeriese metodes in die veld van hidrouliese breking is hoofsaaklik gebaseer op kontinuum metodes, soos die Eindige Element Metode (EEM) en die Rand Element Metode (REM). Hierdie metodes word beheer deur Linieêre Elastiese Breukmeganika (LEB) kriteria, wat ly aan die inherente gebrek van 'n nie-fisiese voorstelling van die spanning by die fraktuur punt. Om hierdie probleme aan te spreek, word 'n nie-lokale metode voorgestel, naamlik die peridinamiese teorie, om gehulsde hidrouliese breking te modelleer. 'n 2D implisiete kwasi-statiese ordinêre toestand gebaseerde peridinamika formulering word geïmplimenteer op verskeie norm probleme, om te verifieer of dit oor die vermoë beskik om die konstitutiewe gedrag van 'n linieêre elastiese soliede materiaal te modeleer, asook die kwantifisering van nadelige effekte op die verplasings oplossing as gevolg van die natuur van die nie-lokale teorie. Normtoetse bestaan uit 'n plaat in trek spanning, waar konvergensie na die klassieke verplasings oplossing, nie-uniforme verfyning en variêerende sel groottes getoets word, asook 'n dikwandige silinder onder interne druk, waar drie verskillende belasting aanwendingstegnieke getoets word. Die mees akkurate belasting aanwendingstegniek word dan gebruik in die gehulsde hidrouliese breking model, om fraktuur aanvangs en uitbreiding na te boots. Die model word dan geverifieer deur die Rummel & Winter hidrouliese breking model en eksperimentele resultate, onderskeidelik. Fout minimering metodes word toegepas en as 'n resultaat, konvergeer die verplasing oplossing vir die plaat na die analitiese oplossing, terwyl die oplossing van die dikwandige silinder onakuraathede toon as gevolg van 'n toegepaste belasting op 'n onreëlmatig gediskretiseerde gebied. Die modellering van die fraktuur inisiëring by die fraktuur punt, stem goed ooreen met die Rummel en Winter voorspelling en die fraktuur uitbreiding stem goed ooreen met eksperimentele resultate. Hierdie navorsing toon dat die peridinamiese benadering tot gehulsde hidrouliese breking wel die fraktuur inisiëring en uitbreiding realisties kan modelleer, maar nog navorsing word wel benodig in die area waar 'n druk belasting op 'n peridinamiese soliede model toegepas word.

Acknowledgements

First and foremost, I would like to thank my heavenly Father, for without His marvellous creation, there would be nothing to research.

I would also like to express the deepest appreciation and gratitude for the following persons, for their continued support, assistance and knowledge shared, during the course of this study.

- My supervisor Dr. Daniel Z. Turner, for introducing me to the field of peridynamics and delivering endless help and support on the topic.
- My co-supervisor, Dr. J.A.vB. Strasheim, for some valuable last minute insights and revising.
- Dr. Rich Lehoucq, for some valuable discussions on peridynamics.
- All my friends, family and my two colleagues, Johan Conradie and Leroi Pols, for many laughs and their continued support.
- Kirstie Nel, for her continued support.
- Lastly, my parents, Marthinus and Juliana van der Merwe, for giving me the opportunity to complete my tertiary education.

Contents

List of Figures

List of Tables

Abbreviations

ADR	**A**daptive **D**ynamic **R**elaxation
ASTM	**A**merican **S**ociety for **T**esting and **M**aterials
BEM	**B**oundary **E**lement **M**ethod
CENRBB	**C**hevron **E**dge **N**otched **R**ound- **B**ar-in-**B**ending
CG	**C**onjugate **G**radient
CZE	**C**ohesive **Z**one **E**lements
DDM	**D**isplacement **D**iscontinuity **M**ethod
DEM	**D**iscrete **E**lement **M**ethod
DS(T)	**D**isc **S**haped Compact Specimen
EPFM	**E**lastic-**P**lastic **F**racture **M**echanics
FEA	**F**inite **E**lement **A**nalysis
FEM	**F**inite **E**lement **M**ethod
FPZ	**F**racture **P**roccess **Z**one
GMRES	**G**eneral **M**inimal **RES**idual
KGD	**K**ristianovic-**G**eertsma-de **K**lerk
LEFM	**L**inear **E**lastic **F**racture **M**echanics
LSY	**L**arge **S**cale **Y**ielding
MD	**M**ollecular **D**ynamics
MF	**M**ini **F**racture
SMF	**S**leeved **M**ini **F**racture
SR	**S**hort **R**od
SSY	**S**mall **S**cale **Y**ielding
SIF	**S**tress **I**ntensity **F**actor
XFEM	e**X**tended **F**inite **E**lement **M**ethod

Symbols

Symbol	Meaning	SI Unit
General:		
A	area	m^2
B	breadth	m
D	average grain size	m
E	modulus of elasticity	N/m^2
E'	E for plane strain	N/m^2
k	bulk modulus	N/m^2
L	length of $\mathcal{R}$	m
L_c	length of $\mathcal{R}_c$	m
L_l	length of $\mathcal{R}_l$	m
m	order of magnitude	
M	p-wave modulus	N/m^2
P	point load	N
p_i	internal pressure	N/m^2
p_o	external pressure	N/m^2
p_c	pressure on crack face	N/m^2
r_i	inner radius	m
r_o	outer radius	m
$\mathcal{R}$	material region	m^3
$\mathcal{R}_l$	loading region	m^3
$\mathcal{R}_c$	constraint region	m^3
$\mathcal{R}_d$	damage region	m^3
V	volume	m^3
v_p	p-wave velocity	m/s
W	strain energy density	J
s	surface	m^2
ϵ	strain	m/m
$\boldsymbol{\epsilon}$	second order strain tensor	m/m
κ	bulk modulus	N/m^2
μ	shear modulus	N/m^2
ν	poison ratio	
ρ_d	dry density	kg/m^3
σ	stress	N/m^2
$\boldsymbol{\sigma}$	second order stress tensor	N/m^2
Fracture mechanics:		

a	crack half length	m
b	crack width	m
c_s	loading strip	m
f	dimensionless function	
$f(\beta)$	weight function for σ_H loading	
g	dimensionless function	
$g(\beta)$	weight function for σ_h loading	
G	strain energy release rate	J/m^2
G_C	critical strain energy release rate	J/m^2
$G_{\mathrm{I}}\, G_{\mathrm{II}}\, G_{\mathrm{III}}$	Mode I, II and III energy release rate	MPa $\sqrt{\mathrm{m}}$
$G_{\mathrm{Ic}}\, G_{\mathrm{IIc}}\, G_{\mathrm{IIIc}}$	Mode I, II and III critical energy release rate	MPa $\sqrt{\mathrm{m}}$
h_m	weight function	
h_{Im}	weight function for Mode I loading	
$h(\beta)$	weight function for p_i loading	
$h_c(\beta)$	weight function for p_c loading	
K	stress intensity factor	MPa $\sqrt{m}$
K_c	critical stress intensity factor	MPa $\sqrt{m}$
$K_{\mathrm{I}}\, K_{\mathrm{II}}\, K_{\mathrm{III}}$	Mode I, II and III SIF	MPa $\sqrt{\mathrm{m}}$
$K_{\mathrm{Ic}}\, K_{\mathrm{IIc}}\, K_{\mathrm{IIIc}}$	Mode I, II and III critical SIF	MPa $\sqrt{\mathrm{m}}$
$p_b\, P_{AE}$	breaking pressure	N/m^2
P_b	ultimate failure pressure	N/m^2
r	crack tip radius	m
U	total energy	J
U_t	elastic energy	J
U_c	elastic strain energy release	J
U_p	potential energy	J
W_e	external work	J
β	ratio of a to r_b	
λ_s	surface energy for unit crack extension	J/m^2
σ_f	fracture stress	N/m^2
σ_h	secondary far field stress	N/m^2
σ_H	primary far field stress	N/m^2
σ_θ	hoop stress	N/m^2
τ_i	in plane shear stress	N/m^2
τ_o	out of plane shear stress	N/m^2

Peridynamics:

$\mathbf{b}$	body force density vector	N/m^3
c	stiffness micropotential	N/m
c_f	fictitious damping coefficient	
$\mathbf{D}$	fictitious diagonal density matrix	kg/m^3
$\underline{e}$	extension scalar state	m
$\underline{e}^i$	dilitation extension scalar state	m
$\underline{e}^d$	deviatoric extension scalar state	m
f_s	critical stretch factor	
$\mathbf{f}$	body force density	N/m^3
$\mathbf{f}_e$	force density error stencil	N/m^3
$\mathbf{f}_s$	internal force density stencil	N/m^3
$\mathbf{y}$	material point in deformed state	m

$\mathcal{H}_{\mathbf{x}}$	family of $\mathbf{x}$	m^3
k'	peridynamic bulk modulus 2D	N/m^2
$\mathbf{K}$	system stiffness matrix	N/m^4
$\mathbb{K}$	stiffness double state	N/m^4
$\mathbf{L}$	sum of force densities over a region	N/m^3
m	ratio of δ to r_c	
$\underline{\mathbf{M}}$	unit vector state	
$\mathbf{n}$	normal vector	
p	peridynamic pressure $(-\theta k)$	N/m^2
p_f	pore pressure	N/m^2
P_i	eigenvalue of acoustic tensor	N/m^4
$\mathbf{P}$	acoustic tensor	N/m^4
q	weighted volume	m^5
r	cell radius	m
s	stretch in a bond vector	m/m
s_c	critical stretch	m
s_c	corrected critical stretch	m
t	time	s
$\underline{t}$	force scalar state	N/m^3
$\mathbf{t}$	force density vector	N/m^3
T	kinetic energy	J
$\underline{\mathbf{T}}$	force vector state	N/m^3
U	potential energy	J
$\boldsymbol{u}\,\dot{\boldsymbol{u}}\,\ddot{\boldsymbol{u}}$	displacement, velocity and acceleration vector	m
$\mathbf{U}\,\dot{\mathbf{U}}\,\ddot{\mathbf{U}}$	system displacement, velocity and acceleration	m
$\mathbf{U}_0$	initial system displacements	m
w	micropotential	J/m^6
$\underline{x}$	reference scalar state	m
$\boldsymbol{x}$	material point coordinates in reference state	m
$\mathbf{X}$	system reference positions	m
$\underline{\mathbf{X}}$	reference vector state	m
$\underline{y}$	deformed scalar state	m
$\boldsymbol{y}$	material point coordinates in deformed state	m
$\underline{\mathbf{Y}}$	deformed vector state	m
Z	stability index	
α	peridynamic shear parameter	
δ	horizon radius	m
Δ	grid spacing	m
$\boldsymbol{\zeta}$	deformed bond vector	m
θ	dilatation	m/m
λ	pressure coefficient	
μ_d	damage boolean function	
$\boldsymbol{\xi}$	bond vector	m
ρ	mass density	kg/m^3
ϕ	damage	
ω	influence function	
∇	Frêchet derivative	

To my Mother:

*Juliana Maryna van der Merwe (**née** van der Hoven)*
**27/02/1956 - †04/07/2010*

Chapter 1

Introduction

With increasing demand for energy in South Africa, the Whitehill shale in the Karoo basin has recently been identified as a formation that is rich in natural gas (Branch et al., 2007). The extraction of this gas is only done through unconventional techniques, such as hydraulic fracturing (Montgomery and Smith, 2010). According to prospects, the amount of natural gas contained in the Whitehill shale is enough to make South Africa energy independent in terms of gas (Xiphu, 2011), as most of the South African natural gas supply is imported. If allowed, the hydraulic fracturing of the Whitehill formation will be the first of its kind in South Africa. To date, there is no robust application that can simulate fluid induced fracture related problems. Moreover the efficient and safe design of future hydraulic fracturing operations will rely heavily on the ability to numerically predict possible outcomes for the physical processes involved, especially when an operation like this is conducted in an area where the environment is sensitive to pollution and water scarcity.

Current numerical models are mostly based on continuum methods, like the Finite Element Method (FEM) and the Boundary Element Method (BEM). FEM approaches to fracture simulation can be categorized in two groups, namely the element degradation method, which incorporates smeared crack modelling (Rashid, 1968), and the boundary breaking method, which incorporates Cohesive Zone Elements (CZE) (Hilleborg et al., 1976). Although these two groups where widely used to model rock and concrete fracture, recent developments in the FEM were especially focussed on dealing with fracture propagation. These developments consist of the eXtended Finite Element Method (XFEM) (Belytschko and Black, 1999), which gives the ability for cracks to move through elements, and a large family of meshless methods. When considering application to hydraulic fracture, recent work by Weber et al. (2013), based on the XFEM, shows the ability to couple fluid flow and fracture propagation, where explicit

functions are implemented to update fracture criteria. Apart from this, Chen (2013) showed that fluid coupled XFEM models, available in ABAQUS software, compare well with theoretical models, like the Kristianovic-Geertsma-de Klerk (KGD) (Geertsma and de Klerk, 1969) solution for hydraulic fractures. The BEM approach is also common for fracture simulation. This method is advantageous in the sense that the governing equation is based on an integral and simple mesh generation makes it computationally less expensive. Recent work by Jo and Hurt (2013) utilised the displacement discontinuity method (DDM) (Crouch and Starfield, 1983), which is a sub method of the BEM, to show the ability of these displacement discontinuity elements to reproduce stress intensity behaviour at the crack tip, which is often ignored in literature produced from the oil and gas industry.

All of the above mentioned methods provide accurate solutions for displacement, stress and strain. With the ability to operate at a very large length scale and when considering fracture operations that can span thousands of metres, it seems logical to develop these continuum methods in order to model hydraulic fracture operations. There is however, an inherent flaw, when considering FEM or BEM as a numerical approach to model fracture propagation in geologic materials. Both of these methods rely on external criteria, based on Linear Elastic Fracture Mechanics (LEFM), to govern fracture growth. Crack nucleation is an unsolved problem in LEFM, therefore the governing fracture algorithms tend to become more and more complex in order to simulate problems where new cracks form in the absence of initial cracks, for instance crack bifurcation (Kazerani, 2011; Madenci and Oterkus, 2014).

Various discontinuum methods have been introduced in order to more accurately capture the process of fracture. These include the Discrete Element Method (DEM) (Cundall, 1971), the lattice model (Brandtzaeg, 1927) and the Molecular Dynamics (MD) (Alder and Wainwright, 1959). The DEM can be seen as an assemblage of interacting rigid particles with the ability to include contact detection while in the calculating process. These interactions can be seen as springs between rigid particles that characterise the constitutive behaviour of the material. This method can accurately represent bonded material grains if it is applied in the same length scale and is more useful in simulations with either small geometries or large grain sizes, such as large blocks of rock material. The lattice model can be seen as a network of bar elements that represents a continuum. This method is especially useful when the effects of dynamic loading is considered. Lastly, the MD is a computer simulation that models interaction forces between atoms, where the interactions are not based on the constitutive properties of the material, but rather a micro-potential that characterises the forces between atoms in the material. Moreover, the MD and lattice model can both be expressed as non-local models, since

interaction between material points extends further than their nearest neighbours. Non-local theory of continuous media can be seen as the connection between local classical continuum mechanics, where material point interactions only occur with other points in their immediate vicinity, and non-local continuum mechanics, like the MD and lattice model.

Most non-local models use strain averaging, or strain derivatives, to include non-locality in the stress and strain relation, in effect retaining the spatial derivative (Eringen et al., 1977). Kunin (1983) and Rogula (1983) used a different approach, where displacements instead of spatial derivatives are used in an integral based governing equation, where the continuous medium is represented by a discrete lattice structure. Silling (2000) introduced the peridynamic theory, where no spatial derivatives are required, similar to that of Rogula (1983), but where damage is included in the material response and where a non-linear material response can be implemented. The peridynamic theory is essentially capable of simulating fracture in length scales ranging from the nano to macro scale without the need for external fracture criteria. In addition it has the ability to adapt to non-local, or local continuum theories, without any alteration to the governing equation. In effect, this enables the peridynamic model to capture non-local microscopic phenomena, like micro cracking at the crack tip, while simultaneously capturing local macroscopic phenomena, like deformation of a continuous body.

The peridynamic theory is in essence, independent from mathematical artefacts introduced by continuum mechanics, such as the non-physical infinite stress at the onset of crack nucleation, according to LEFM. In contrast to this, the usage of LEFM, when a crack is already present, still yields an accurate representation of stress intensities at the crack tip and in this sense, LEFM can be used as a verification tool. A truly robust model for fluid induced fracture can be defined as a model that can capture an accurate displacement solution, as well as, capture the nucleation and propagation of fractures, in the form of damage. In addition, this should all be achieved under one governing equation, without the need for external criteria to steer fracture growth, which inherently increases numerical complexity. A robust numerical model for fluid induced fracture is essential to the design of safer and more efficient techniques in the field of fluid induced fracture.

1.1 Research objectives

The aim of this research is to obtain a robust peridynamic model that can accurately predict fluid induced fracture behaviour and to lay the building blocks for a numerical model that can easily deal with complex fracture related problems. These include

problems such as hydraulic fracturing, dam wall fracture and pumping in pavements. In order to reach this main objective, a few sub objectives were identified i.e.:

- Successful application of the peridynamic theory to 2D plane strain peridynamic models with block and cylindrical geometries, while accurately capturing the constitutive behaviour of the material.
- Quantification of adverse affects when non-uniform refinement, as well as alternative cell (element) shapes are implemented.
- Verification of crack tip behaviour by using LEFM.
- Successful fracture propagation through a standard hydraulic fracture core specimen through the implementation of an implicit quasi-static solution under an internal pressure loading.

1.2 Methodology

In this study, the peridynamic theory is chosen as a research tool. Therefore, various peridynamic models will implement the theory, to demonstrate that the theory can accurately capture the constitutive relationship for a specific material. Secondly, to capture the effect of stress intensity around the crack tip, as well as, the effect of initial crack size according to LEFM. The detailed approach in chronological order can be described in the following steps:

- Apply the peridynamic theory to a model with a cube geometry in 3D under a tensile stress loading. Verify the constitutive behaviour of the model, by analysing the displacement solution.
- Derive a 2D plane strain peridynamic formulation based on the 3D state based peridynamic formulation. Apply this formulation to a model with a square plate geometry with unit thickness and affine uniform discretization. Again verify the constitutive behaviour of the model, by analysing the displacement solution.
- Due to the nature of non-local theories, the solution can exhibit defects when non-uniform refinement and different cell shapes are implemented. These defects will be quantified in order to make calculated decisions on these aspects, when more complex geometries are considered.
- Apply the 2D plane strain formulation to a model with a thick walled cylinder geometry, in order to verify if the correct radial displacement solution can be captured.

- Verify fracture initiation by applying the 2D plane strain formulation to a model with geometry based on theoretical hydraulic fracture models. The breaking pressure will be verified as a function of initial crack size.
- Validate fracture propagation of above mentioned model, by means of comparison to experimental results obtained from various sources in the literature.

1.3 Thesis layout

The structure of this thesis is intended to create a continuous flow in order to explain the stepwise research process taken to obtain a good understanding of the analytical problem, as well as, the peridynamic theory. The peridynamic theory will ultimately be applied, to obtain the outlined objective. By following this approach, the literature study will be divided in two chapters, firstly discussing the analytic mechanics behind the problem, followed by a thorough discussion on the numerical approach. The implementation of the numerical approach and the results obtained will be presented in the next three chapters. Lastly, a thorough discussion will be conducted on some key aspects of the numerical approach, as well as a conclusion to state whether the objective has been reached.

Literature study

Chapter 2 will give an overview of LEFM and discuss assumptions that had to be made in order to ensure validity for the physical problem under consideration. In addition, the link to rock fracture mechanics will be discussed and how it is implemented in analytic hydraulic fracturing models, like the Rummel & Winter hydraulic fracturing model. Lastly the Rummel & Winter hydraulic fracturing model will be discussed in detail, which will serve as the analytic framework from which the peridynamic model will be verified.

Following the review on the analytic approach, Chapter 3 will discuss the peridynamic theory, starting with a brief introduction on the bond based theory. Then an in depth discussion on the ordinary state based peridynamic theory will be conducted, as this will be the numerical framework on which this research is based. Lastly, general issues regarding the application of the peridynamic theory will be discussed in order to create a better understanding of how the theory can be practically implemented.

Model description and implementation

Chapter 4 will describe the peridynamic model that will be used in this research, to

simulate sleeved hydraulic fracture. Firstly, an introduction will be given to the physical model regarding geometry, discretization, material properties and general boundary conditions. Thereafter, various loading schemes will be introduced and the reason why alternate forms of loading need to be implemented. This will be followed by a range of issues that will need special attention when modelling in the peridynamic framework i.e.; numerical convergence, model dimension and mesh dependency.

Following a thorough description on all practical aspects of the peridynamic model, Chapter 5 will involve verification by means of different benchmark tests, that will be done in order to ensure a robust end-product. Displacement tests for simple block geometries will be performed, including tests to quantify effects of non-local nature. The results of these tests will be displayed in Chapter 5 and discussed in depth in Chapter 7.

Lastly, Chapter 6 will involve the implementation on the sleeved hydraulic fracture model. Firstly by obtaining a displacement solution for the thick walled cylinder and then a fluid induced, sleeved hydraulic fracture test will be done, to verify fracture initiation and fracture propagation. All test results displayed in Chapter 6 will be the main outcome of this thesis and these results will also be discussed in depth in Chapter 7.

Discussion and conclusion

Chapter 7 will serve as a discussion on the results obtained, as well as, focus on challenging issues that have been encountered, such as convergence to the classic solution, mesh dependency and numerical convergence. Results obtained from fracture initiation tests will also be discussed in detail.

Finally, Chapter 8 will conclude all the main findings of this study and focus on future work to develop a peridynamic model for hydraulic fracture, with the capabilities of also simulating pore pressure in porous materials.

Chapter 2

Fracture Mechanics Approaches

2.1 Linear Elastic Fracture Mechanics

Various approaches exist to understand the mechanics behind fracture propagation and this section will mainly be focussed on LEFM, which serves as the basis for the analytical hydraulic fracturing models that will be used in this research. The reason for starting with the Griffith theory, which is more applicable in the field of EPFM (Elasto-Plastic Fracture Mechanics), is merely due to the simplicity of the energy balance approach to understanding all the contributing factors in the process of fracture propagation, as well as the fact that the damage model for the peridynamic theory (which will be discussed in Chapter 3) is also based on energy density considerations. The following is a detailed discussion of the Griffith energy balance approach as well as why LEFM can be considered when modelling hydraulic fracturing and what assumptions have to be made. Lastly, an introduction to the approach of stress intensity factors and how it can be related to the energy release rate developed by Griffith.

2.1.1 Griffith theory

For a long time, and even in present day, it is accepted in structural design, that a material has a certain critical fracture strength, which is based on the maximum tensile stress that the material can be subjected to before fracture occurs. This is of course based on the assumption that the material in question is perfectly homogeneous and has no microscopic flaws that would inherently weaken the material when loaded. However, it is commonly known, as evidenced by a vast number of tests done on materials, that the material would fail even before the critical fracture stress have been reached.

Evans (1961) showed that the tensile strength of coal was proportional to the test specimen thickness, which indicated that the fracture strength of the material was in fact not a material property. In lieu of this it was discovered that the unit of surface specific energy needed to form a unit of new fracture surface was in fact a material property, independent of the dimensions of the test specimen. To explain this phenomena, Griffith (1921) suggested that especially brittle materials have microscopic cracks. Although Inglis (1913) had already derived a mathematical model for an elliptical crack in a plate, Griffith developed the Griffith energy balance approach that showed the relationship between fracture stress and crack size which served as the starting point of modern day fracture mechanics.

The Griffith energy balance approach is a summation of all energy contributions in a infinite cracked plate with a unit thickness B (see Figure 2.1). A general representation of these contributions can be expressed as:

$$U = U_t + U_c - W_e + U_s = U_p + U_s, \tag{2.1}$$

where U is the total energy in the plate, U_t the total initial elastic strain energy of the uncracked plate, U_c the elastic strain energy release caused by a crack of size $2a$ resulting in a relaxation of the material close to the crack, W_e the work done by external forces, U_s the change of elastic surface energy due to the formation of new crack surfaces and $U_p = U_c - W_e + U_s$ the change in potential energy.

These energy contributions can be derived as follows:
Initial elastic strain energy (U_t) over the volume, where $E' = E/(1-\nu^2)$ is the effective Young's modulus for plane strain.

$$U_t = \frac{1}{2}\int_V \sigma_y \epsilon_y (B dx dy) = \frac{\sigma^2 A}{2E'} \tag{2.2}$$

Elastic strain energy release (U_c) due to displacement v of the crack surfaces perpendicular to each other where $v = (2\sigma\sqrt{a^2 - x^2})/E'$.

$$U_c = 2\int_0^a v(\sigma B dx) = \pm\frac{\pi\sigma^2 a^2}{E'} \tag{2.3}$$

Work (W_e) done by external forces on the plate boundaries in terms of the applied load P and the relative displacement v.

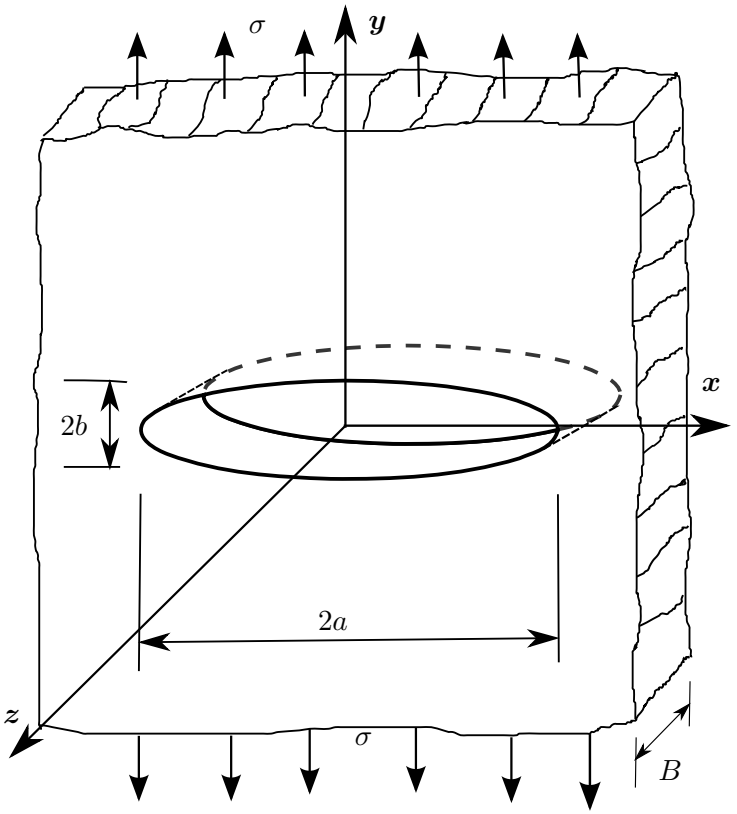

FIGURE 2.1: Elliptical crack in an infinite plate (Whittaker et al., 1992).

$$W_e = \int_V P dy = \frac{\sigma \epsilon A}{2} \tag{2.4}$$

Change in elastic surface energy (U_s), where γ_s is the specific surface energy required to create a unit area of new surface crack.

$$U_s = 2A'\gamma_s = 4a\gamma_s \tag{2.5}$$

By substituting (2.2)-(2.5) into (2.1), the expression for the total energy in the infinite plate can be obtained as in (2.6).

$$U = \frac{\sigma^2 A}{2E'} \pm \frac{\pi \sigma^2 a^2}{E'} - \frac{\sigma \epsilon A}{2} + 4a\gamma_s \tag{2.6}$$

When considering constant displacement, where $W_e = 0$, it can be shown that when the amount of strain energy released (U_c) due to crack extension of Δa is less than the amount of surface energy (U_s) needed for that same extension length, crack propagation will be stable and crack arrest will occur. Clearly, the point where these energy contributions are equal, would be a critical point for fracture initiation and this can

be obtained by differentiating the total energy with respect to a and considering the equilibrium point where all energy rates equal zero.

$$\frac{\partial}{\partial a}\left[\frac{\sigma^2 A}{2E'} - \frac{\pi\sigma^2 a^2}{E'} + 4a\gamma_s\right] = 0 \tag{2.7}$$

After differentiation, the following identity (2.8) can be established and since this is at the critical point, the stress can then be regarded as the fracture stress (σ_f) in (2.9).

$$\sigma\sqrt{\pi a} = \sqrt{2E'\gamma_s} \tag{2.8}$$

$$\sigma_f = \sqrt{\frac{2E'\gamma_s}{\pi a}} \tag{2.9}$$

When rearranging (2.8), (2.10) can be obtained, where the left hand side can be regarded as the elastic energy per unit crack surface that is available for crack extension.

$$\frac{\pi\sigma^2 a}{E'} = 2\gamma_s \tag{2.10}$$

This is then called the strain energy release rate G in (2.11), named after Griffith, and it describes the rate at which strain energy is released due to crack growth.

$$G = \frac{\partial U_c}{\partial a} = \frac{\pi\sigma^2 a}{E'} \tag{2.11}$$

Lastly, the Griffith G for this case is at a critical point and it can be written as:

$$G = G_c, \tag{2.12}$$

where G_c is the critical energy release rate of the material, also known as the fracture toughness of the material. In the case where a load is applied so that G is equal to or greater than G_c of the material, the fracture would propagate and in this sense G_c is a characteristic property of the material.

2.1.2 Assumptions for Linear Elastic Fracture Mechanics

Small scale yielding (SSY)

When considering the stress intensity approach at the crack tip of any material, the

expression for stress fields at the crack tip yields infinitely high stresses for any given loading. This $1/\sqrt{r}$ stress singularity prediction is non-physical in real materials as all flaws have some finite radius r and no material can withstand infinite stress. To account for this there has to be some region that absorbs this high amount of energy before fracture initiation can even take place. This phenomenon has been studied extensively, especially in metals that have elastic-plastic material properties, where it is known that when the yield strength of a material is reached, plastic deformation will occur in order to absorb excess energy. The zone where this happens is known as the plastic zone (see Figure 2.1(b)) and it is situated around the crack tip (Anderson, 2000). In materials with high plasticity, this zone can be rather large, which will eliminate the validity of LEFM and this is called large scale yielding (LSY). However when the plastic zone is sufficiently small compared to the dimensions of the specimen and linear elastic behaviour prevails before failure, it can be called small scale yielding (SSY), where LEFM is still valid in predicting fracture initiation (Whittaker et al., 1992). The American Society for Testing and Materials (ASTM) set standards for limiting plastic zone size in relation to the specimen size for steel specimens (ASTM E 399, 2009). This phenomenon can also be applicable to rock fracture mechanics when considering brittle and quasi-brittle materials. However, since no plasticity is present in these materials, the mechanism in which energy is absorbed is somewhat different. Instead of yielding of the material, small micro cracks develop that fill the volume near the crack tip and research by Hoagland et al. (1973) revealed that the surface specific energy absorbed by these micro cracks can be 100 times the magnitude of the energy absorbed by the initial crack surface. Extensive research has been done on this zone, which is called the fracture process micro cracking zone (FPZ) (see Figure 2.2(b)) (Atkinson, 1991; Hoagland et al., 1973). In some rocks, the FPZ can be large enough in order for the material to behave in a plastic manner and in this case, LEFM will not be valid for fracture prediction. The FPZ is the general factor which decides if LEFM or EPFM should be used to predict fracture initiation (Whittaker et al., 1992).

Fracture process zone (FPZ)

Fracture, or de-cohesion of rock particles can be described in three different length scales, namely the molecular, micro and macro length scale. Irrespective of whether it is observed from micro or macro scale, molecular bonds breaking between rock molecules are the main origin of fracture propagation (Kazerani, 2011). This phenomenon is however too small to model numerically in engineering applications, thus the interest in the micro length scale, where rock particles are discretely modelled as elements cohesively joined together, and the macro scale, where lumps of material are modelled according to a failure criteria. The macro length scale approach is numerically more acceptable

for application to engineering problems, but the FPZ is still governed by the formation of microscopic cracks. In lieu of this, it is important to ensure that the assumptions for LEFM are indeed valid, by investigating the FPZ and microscopic rock behaviour for the type of rock in question.

Micro cracks can be seen as the separation of rock grains and this can be caused by failure of the mineral cement or weak grains. Grain size is an important property to account for, as the FPZ normally depends on the grain size (Hoagland et al., 1973). The nature of loading would also have an effect on the size of the FPZ, but in this research, only quasi-static loading will be considered, rendering this factor as a constant. Sizes for the FPZ are typically found to be within five to ten times the average grain size (Hoagland et al., 1973; Zhang et al., 2000) and when considering rock material with very small average grain size, like shale with an average grain size of $60\,\mu m$ (Stow, 2005), it can be observed that the FPZ is in fact negligibly small compared even to a core sample of $60mm$ in diameter. When considering the size of a hydraulic fracturing operation, it can then be easily assumed that SSY would prevail rendering the use of LEFM as a valid option for fracture prediction.

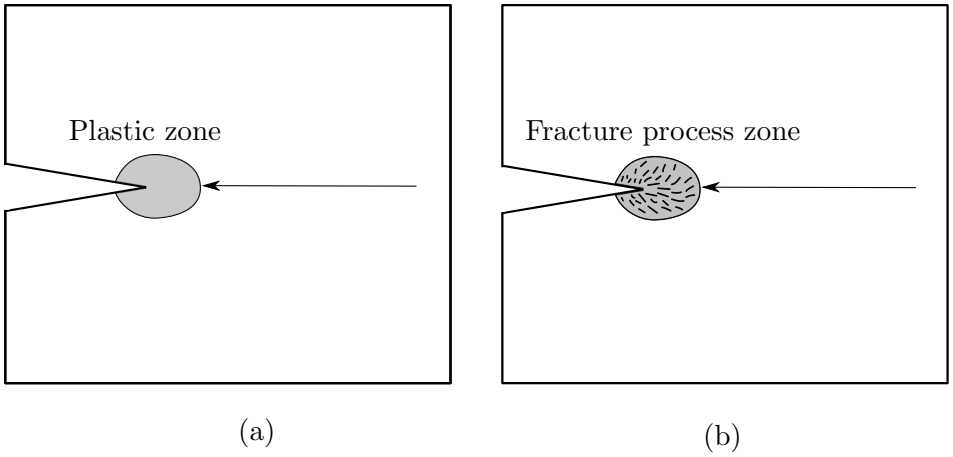

FIGURE 2.2: (a) Plastic zone, for metallic materials and (b) fracture process zone for brittle materials.

2.1.3 Stress intensity factors

When considering an isotropic linear elastic material, there exist analytical expressions for the stress fields (σ_{ij}) in the body and around the crack tip. These expressions were derived by Westergaard (1939), Irwin (1957) and Williams (1957). Since the stress field is best described in terms of the radius around the crack tip, the expression is based in cylindrical coordinates as:

$$\sigma_{ij} = \left(\frac{k}{\sqrt{r}}\right) f_{ij}(\theta) + \sum_{m=0}^{\infty} A_m r^{\frac{m}{2}} g_{ij}^{(m)}(\theta), \tag{2.13}$$

where σ_{ij} is the stress tensor, θ and r the cylindrical coordinates, k a constant, f_{ij} a dimensionless function of θ and the second expression is the higher order terms that are dependent on the geometry, where A_m is the amplitude, m the order of magnitude and g_{ij} a dimensionless function of θ. It should be noted that for any setting, the leading term of $1/\sqrt{r}$ will always cause the stress near the crack tip to tend to infinity, thus the higher order functions can normally be disregarded when attention is given to the near crack tip zone.

The proportionality constant k and the dimensionless function f_{ij} depend on the mode of loading and fracture. It can then be convenient to replace k by the stress intensity factor K. Where $K = k\sqrt{2\pi}$ and essentially becomes the governing parameter for LEFM. The critical stress intensity factor (K_C) can be seen as the material property, similar to the critical energy release rate G_c. For instance, when the stress intensity field around a crack tip exceeds the K_C, the crack will propagate. A linear elastic brittle material can be subjected to three basic modes of loading and deformation that describes the way in which a material can fail in fracture. The three modes include normal stress σ, in-plane shear stress τ_i and out of-plane shear stress τ_o. These are represented graphically in Figure 2.3 and can be described as follows:

- **Mode I**, also called the opening mode, where the crack tip is subjected to a normal stress σ and causes crack surface displacements perpendicular to the crack plane.
- **Mode II**, also called the sliding mode, where the crack tip is subjected to in-plane shear stress τ_i and causes the crack faces to slide relative to each other in the direction perpendicular to the crack front.
- **Mode III**, also called the tearing mode, where the crack tip is subjected to out of plane shear stress τ_o and causes the crack faces to slide relative to each other in the direction parallel to the crack front.

From these three modes of loading, comes three different types of stress intensity factors, namely K_I, K_{II} and K_{III}. These can act together to cause mixed mode loading and every material has a certain toughness against fracture in each of these modes that can be denoted by the critical stress intensity factor (K_{IC}, K_{IIC} and K_{IIIC}) for each mode respectively.

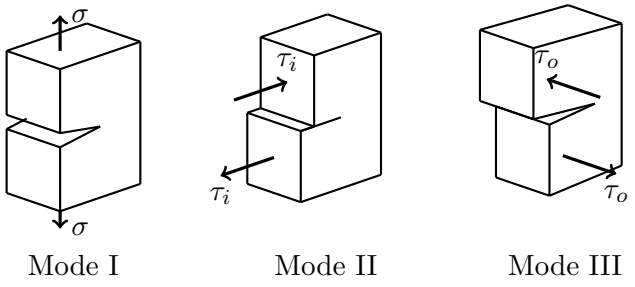

FIGURE 2.3: Modes of loading for a crack and corresponding crack tip displacements (Whittaker et al., 1992).

2.2 Rummel and Winter fracture mechanics model

2.2.1 Weight function method

Consider two loading cases on a cracked plate (see Figure 2.19). Only one of the loading cases has a known load and resulting displacement while the other only has a known load, according to the reciprocal theorem, the unknown displacement can be obtained by a combination of the known values. The same goes for calculating the stress intensity caused by different discrete loads on the plate.

In this case, when the discrete loads are seen as tractions $T(s)$ on the surface s of a cracked body, finding the correct weight function h_m and integrating over the crack length a will yield the stress intensity value for that specific load system.

$$K = \int_a h_m(s,a)T(s)ds \tag{2.14}$$

The first application of h_m was done by Bueckner (1958), when he devised a weight function (h_{Im}) for the simplified case of Mode I loading on an infinite plate, assuming no tractions on the crack tip.

$$h_{Im}(s,a) = \frac{E'}{2K_I}\frac{\delta V(s,a)}{\delta a} \tag{2.15}$$

This weight function is known as the Bueckner weight function, where $V(s,a)$ indicates different variations for the displacement in the direction of the applied traction and $\partial V(s,a)/\partial a$ indicates the variation when differentiated with respect to the crack length a. Consider the crack problem in Figure 2.4, where an infinite plate is subjected to two different loads. The load in Figure 2.4(a) is a standard fracture mechanics problem with a simple analytic solution, where the stress intensity factor ($K_I^{(a)}$) and displacement ($v(s,a)$) in the direction of the stress field σ_y can be obtained by (2.16).

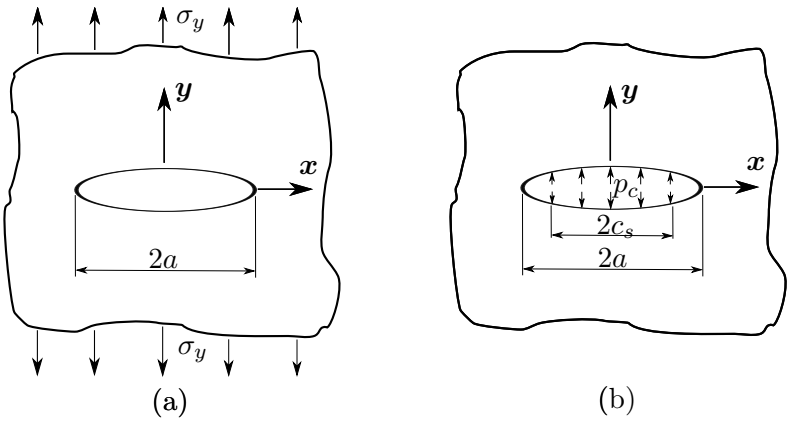

FIGURE 2.4: Two different modes of loading comprising of (a) a far field stress σ_y and (b) a internal pressure $p_c(x) = \sigma_y$ distributed over $2c$ (Whittaker et al., 1992).

$$\left.\begin{aligned} K_I^{(a)} &= \sigma\sqrt{\pi a}, \\ v(x,a) &= \frac{2\sigma\sqrt{a^2-x^2}}{E'} \qquad (-a < x < a) \end{aligned}\right\} \tag{2.16}$$

On the other hand, in Figure 2.4(b) is a much more complex loading in the form of an internal pressure $p_c(x)$ over the strip $2c$ on the face of the crack. Where $p_c(x) = \sigma_y$ for $-c < x < c$. In order to find the stress intensity factor $K_I^{(b)}$ for the internal loading, the known case in Figure 2.4(a) is simply substituted into the weight function yielding:

$$h_{Im}(s,a) = \frac{E'}{2\sigma\sqrt{\pi a}}\frac{2\sigma}{E'}\frac{2}{\sqrt{a^2-x^2}} = \sqrt{\frac{a}{\pi(a^2-x^2)}} \tag{2.17}$$

and now that the weight function for this specific problem is known, it can be used to obtain the stress intensity factor produced by any other loading scheme on the same problem. Subsequently the stress intensity factor for the loading case in Figure 2.4(b) can be defined as:

$$K_I^{(b)} = \int_{-c}^{c}\sqrt{\frac{a}{\pi(a^2-x^2)}}p_c(x)dx. \tag{2.18}$$

2.2.2 Superposition principle

The superposition principle is very convenient when the verification of different aspects of the numerical hydraulic fracturing model is concerned. This gives the ability to verify contributions to fracture extension due to borehole pressure, fluid pressure on crack faces, as well as the influence of far field stresses in the formation in a separated fashion. The stress intensity factor can be superimposed in the following form:

$$K_I(\sigma_H, \sigma_h, p_i, p_c) = K_I(\sigma_H) + K_I(\sigma_h) + K_I(p_i) + K_I(p_c), \tag{2.19}$$

where $K_I(p_i)$ is the contribution by pressure acting on the walls of the borehole, $K_I(p_c)$ the contribution of fluid pressure on the faces of the crack and $K_I(\sigma_H)$ & $K_I(\sigma_h)$ the contribution of the primary and secondary far-field stresses respectively.

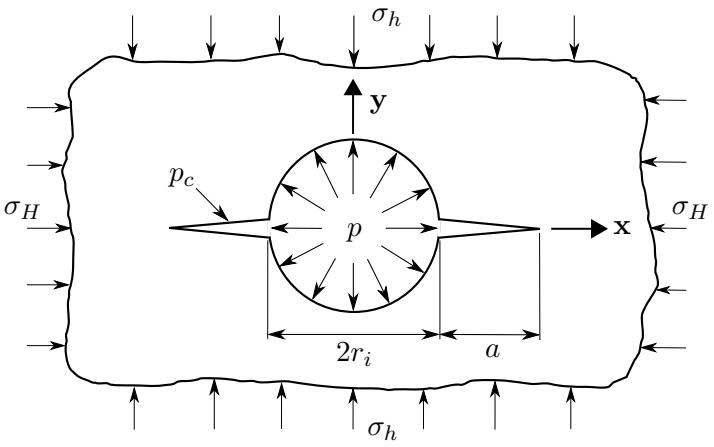

FIGURE 2.5: Rummel & Winter hydraulic fracture model (Whittaker et al., 1992).

From the weight function method, described in Section 2.2.1, a solution can be calculated for each stress intensity contribution by using (2.20), where the distribution of $\sigma_\theta(x, 0)$ is known and σ_θ denotes the hoop stress around the borehole.

$$K_I^{(b)} = \sqrt{\frac{a}{\pi}} \int_{-(a+r_i)}^{a+r_i} \sqrt{\frac{\sigma_\theta(x,0)}{(a+r_i)^2 - x^2}} dx \tag{2.20}$$

These contributions (2.21)-(2.23) can then be calculated by the applied load, the borehole size and the dimensionless weight functions of β ($f(\beta)$, $g(\beta)$, $h(\beta)$ and $h_c(\beta)$), where $\beta = 1 + a/r_i$.

$$K_I(\sigma_H) = -\sigma_H \sqrt{r_i} f(\beta) \tag{2.21}$$

$$K_I(\sigma_h) = -\sigma_h \sqrt{r_i} g(\beta) \tag{2.22}$$

$$K_I(p) = p_i \sqrt{r_i} h(\beta) \tag{2.23}$$

$$K_I(p_c) = p_c \sqrt{r_i} h_c(\beta) \tag{2.24}$$

The following expressions were derived by Rummel and Winter (1982) to calculate the dimensionless weight functions for the various loading cases.

$$f(\beta) = -2\sqrt{\frac{\beta^2 - 1}{\pi\beta^7}} \tag{2.25}$$

$$g(\beta) = \sqrt{\pi\beta}\left(1 - \frac{2}{\pi}\arcsin\frac{1}{\beta}\right) + 2(\beta^2 + 1)\sqrt{\frac{\beta^2 - 1}{\pi\beta^7}} \tag{2.26}$$

$$h(\beta) = 1.3\frac{\beta - 1}{1 + \beta^{\frac{3}{2}}} + 7.8\frac{\sin[(\beta - 1)/2]}{2\beta^{\frac{5}{2}} - 1.7} \tag{2.27}$$

$$h_c(\beta) = \sqrt{\pi\beta}\left(1 - \frac{2}{\pi}\arcsin\frac{1}{\beta}\right) \tag{2.28}$$

It should however be noted that the expression for $h_c(\beta)$ can have many forms, depending on the distribution of pressure on the crack face. In this particular case, the distribution of pressure is assumed constant over the whole crack face. This assumption would not be realistic in practice, due to effects of fluid lag and crack face discontinuities. Fluid lag is the inability of the fluid to penetrate the entire length of the crack, due to a small crack opening width at the fracture tip, causing non-uniform pressure distribution. However, for the purpose of verification and considering the basic nature of the numerical model, it was decided to use the simplest case for the initial verification. The stress intensity factor expression in (2.19) can now be rewritten in terms of the dimensionless weight functions and the applied loadings, to obtain the total stress intensity field from all the contributing factors.

$$K_I = -\left[f(\beta)\sigma_H + g(\beta)\sigma_h\right]\sqrt{r_i} + p_i\sqrt{r_i}\left[h(\beta) + h_c(\beta)\right] \tag{2.29}$$

As discussed in Section 2.1.3, the material will fail when the K_I value becomes greater than the K_{IC} value of the material. The pressure loading at which this will occur is called the breaking pressure p_b. It is then convenient to substitute these values and rewrite the expression in (2.29) to obtain the breaking pressure as a function of the material toughness, far field stresses and geometrical properties of the borehole.

$$p_b = \frac{1}{h(\beta) + h_c(\beta)}\left[\frac{K_{IC}}{\sqrt{r_i}} + f(\beta)\sigma_H + g(\beta)\sigma_h\right] \tag{2.30}$$

Ultimately, p_b can be used in order to verify breaking pressure obtained by the numerical approach for sleeved hydraulic fracture. In addition to this, it will also be used to verify breaking pressure behaviour for small values of a. In essence, the Rummel & Winter approach should deviate from the numerical approach when the initial fracture length tend to zero, due to the non-physical stress value predicted by LEFM, when no initial flaw is present.

Chapter 3

Peridynamic Theory

3.1 Introduction

Peridynamics can be seen as a multi-scale approach to solid mechanics, with the ability to combine the mathematical modelling of continuous and discontinuous media at the nano scale up to macro scale, under one set of governing equations. It has a non-local integral based formulation and instead of assuming a continuous distribution of a solid, like the spatial differential based classical solid mechanics approach, it assumes material point interactions at a finite distance (Silling, 2000; Silling and Lehoucq, 2010b). Since it is multi-scale, material points can resemble molecules (similar to molecular dynamics (Seleson et al., 2009)), where the interaction is governed by molecular bonds, or points resembling lumps of material governed by the constitutive law for the specific type of material. The integral based governing equation eliminates the limiting aspects of the classical differential based theory when discontinuous media, such as cracks, interfaces and particles are concerned. As a result, it can handle fracture problems without any supplemental extensions to the governing equation (Silling et al., 2007).

Three different formulations of the peridynamic theory exist (see Figure 3.1), namely the bond based (Silling, 2000), *ordinary state based* and *non-ordinary state based* theories (Silling et al., 2007). The bond based theory was the first to be developed and is a special simplistic case of the state based theory, where the constitutive law is applied to the bond as a whole. This limits the Poisson ratio to 0.25, because the elastic solid is represented by only two particle interactions, forming a Cauchy crystal. Due to this limit, the state based theory was devised, where the constitutive law is applied on the state of a material point. The state of the material point is defined by all neighbouring material point interactions.

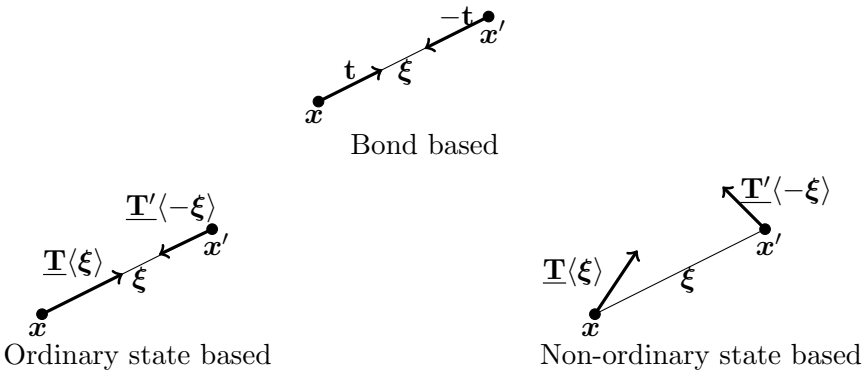

FIGURE 3.1: Three different types of particle interaction theories. (Silling et al., 2007)

An introduction to peridynamics is most easily understood through the bond based theory, by introducing the two-particle force function in (3.1), that describes the interaction between the two particles, by:

$$\rho(\boldsymbol{x})\ddot{\boldsymbol{u}}(\boldsymbol{x},t) = \int_{\mathcal{H}_{\boldsymbol{x}}} \mathbf{t}(\boldsymbol{u}(\boldsymbol{x}',t) - \boldsymbol{u}(\boldsymbol{x},t), \boldsymbol{x}' - \boldsymbol{x}) dV_{\boldsymbol{x}'} + \mathbf{b}(\boldsymbol{x},t), \tag{3.1}$$

where $\boldsymbol{x}$ is a point situated in the centre of the horizon $\mathcal{H}_{\boldsymbol{x}}$, t is the time, ρ is the density, $\boldsymbol{x}'$ is the position of a neighbouring point inside $\mathcal{H}_{\boldsymbol{x}}$, $\mathbf{u}$ is the displacement vector field, $\mathbf{b}$ is the body force and $\mathbf{t}$ is the force density per unit volume that $\boldsymbol{x}'$ exerts on $\boldsymbol{x}$ (Silling et al., 2007).

Since peridynamics is a non-local formulation, the distance that material points interact with each other can be chosen according to the type of material and the length scale which will best capture the physical process that is being modelled. While classical solid mechanics assumes that finite material points only interact with their immediate neighbours, it is known that, especially in solid matter, the inter molecular forces between particles extend beyond the nearest neighbours of each particle (Israelachvili, 1992). In the peridynamic theory, this non-local interaction region can be referred to as the peridynamic horizon $\mathcal{H}$ (see Figure 3.2) and this may be viewed as an effective length scale in which a specific problem is numerically simulated (Bobaru and Wenke, 2012). The peridynamic horizon is mostly taken as spherical (for a 3D solid) and cylindrical (for a 2D solid), which is characterized by the horizon radius δ. All material points that are included in the horizon $\mathcal{H}_{\boldsymbol{x}}$ of a certain material point $\boldsymbol{x}$, are referred to as being in the neighbourhood or being neighbours of $\boldsymbol{x}$. This region is very important, as it determines the length at which material points will effect each other and in turn will determine the characteristics of the material, evolution of damage and the numerical processing demands, in terms of neighbourhood search algorithms, for any physical problem.

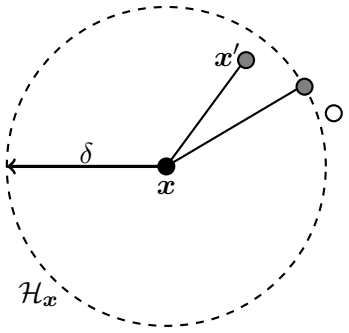

FIGURE 3.2: Spherical neighbourhood $\mathcal{H}_{\boldsymbol{x}}$ of $\boldsymbol{x}$ with a radius δ of all particles $\boldsymbol{x}'$ that interacts with material point $\boldsymbol{x}$.

3.2 Ordinary State Based Theory

The ordinary state based theory is an extension of the bond based theory, where the constitutive law of any ordinary material can be applied through separate parameters, such as dilatation (bulk modulus) and deviatoric (shear modulus) material properties. Material point interactions, in the bond based theory, is seen as independent for each pair of interacting, material points. In the state based theory, the effect of all material point interactions for a single material point can be captured by the use of mathematical objects, called *states* (Silling et al., 2007), to obtain and store the resulting effects of material interactions on each material point. Thus, Silling et al. (2007) called it the *state based* theory. The term, *ordinary state based* theory, refers to ordinary materials and this can be defined as materials where the interaction forces between material points will always be parallel to the bond vector. These include any linear elastic or elastic-plastic materials. On the other hand, the *non-ordinary state based* theory refers to non-ordinary materials and this theory should be able to handle any type of material behaviour (Madenci and Oterkus, 2014). In this research, only linear elastic material properties will be considered and only the *ordinary state based* theory will be discussed and implemented.

3.2.1 States

A state is a very useful mathematical tool in non-local mechanics, as it can capture an infinite number of functions that describe the condition around a material point in a non-local setting. To illustrate the need for the mathematical concept of a state, consider two solid bodies $\mathcal{B}_a$ and $\mathcal{B}_b$ in $\mathbb{R}^2$ and let $\mathcal{L}_m$ denote a set of tensors of order m. When considering Figure 3.3(a), which represents a continuous solid $\mathcal{B}_a$, all stresses can be represented as a function of a second order stress tensor $\boldsymbol{\sigma} \in \mathcal{L}_2$. In contrast, when considering Figure 3.3(b), which represents a continuous solid $\mathcal{B}_b$ through a set

of material points, each with a certain weighted volume, all interaction force densities between material points can be represented by force density vectors $\mathbf{t} \in \mathcal{L}_1$. For a neighbourhood $\mathcal{H}_{\boldsymbol{x}}$ of radius δ centred at material point $\boldsymbol{x}$, the amount of material points $\boldsymbol{x}'$ included in $\mathcal{H}_{\boldsymbol{x}}$ becomes infinite, thus an infinite array of force density vectors $\mathbf{t}$ is needed in order to represent the force density state at material point $\boldsymbol{x}$. This infinite array can then be written as a vector force density state $\underline{\mathbf{T}}\langle\boldsymbol{\xi}\rangle$, that operates on the vector $\boldsymbol{\xi} = \boldsymbol{x}' - \boldsymbol{x}$.

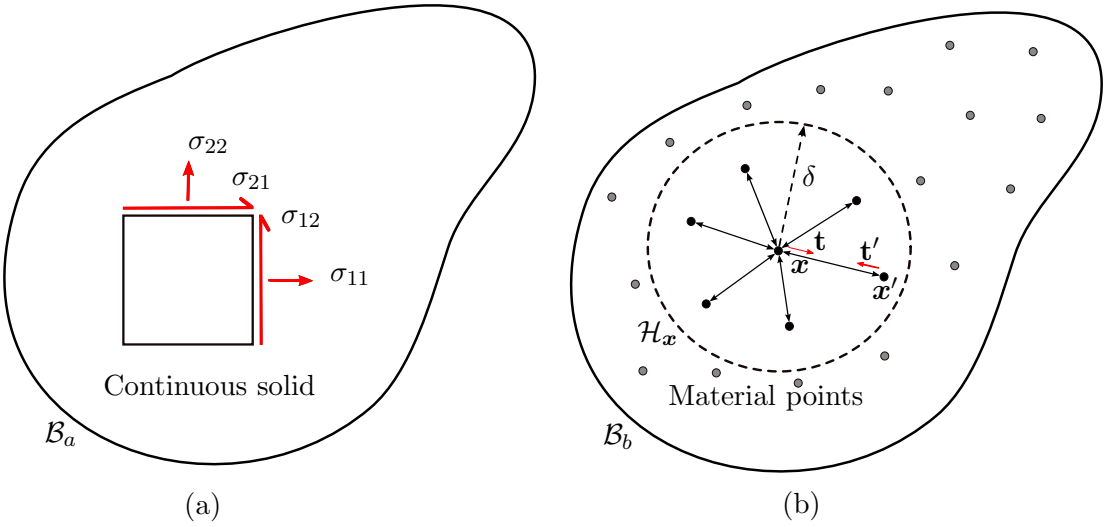

FIGURE 3.3: (a) Stress tensor in a continuous solid vs. (b) peridynamic force functions between material points representing the volume of the solid.

In order to define the notation for states, consider all states of order m to be represented by $\mathcal{A}_m$ and note that these states operate on every material point interaction in the neighbourhood $\mathcal{H}$. Since the neighbourhood consist of bond vectors $\boldsymbol{\xi}$, an image of these vectors under the state $\underline{\mathbf{A}}$ can be denoted as $\underline{\mathbf{A}}\langle\boldsymbol{\xi}\rangle$, where the angle brackets indicate the operation of the state on the vector enclosed in the brackets. A state can also be a function of space and time, $\underline{\mathbf{A}}[\boldsymbol{x}, t]\langle\boldsymbol{\xi}\rangle$, where the square brackets indicate the variables of which $\underline{\mathbf{A}}$ is a function.

A state of order 1 is called a *vector state* and all vector states is denoted $\mathcal{V}$ so that $\mathcal{V} = \mathcal{A}_1$. All states of order $m \geq 1$ are usually written in bold with an underscore, for instance $\underline{\mathbf{A}}$. A state of order 0 is called a *scalar state* denoted $\mathcal{S} = \mathcal{A}_0$, or as $\underline{a}$. These states can represent an infinite number of discrete functions, vectors or higher order terms as in (3.2). A state of order 2 is called a *double state* and is denoted by $\mathcal{D} = \mathcal{A}_2$ or as $\underline{\mathbb{A}}\langle\boldsymbol{\xi}, \boldsymbol{\zeta}\rangle$, where $\underline{\mathbb{A}}$ maps pairs of vectors into a second order tensor (Silling et al., 2010a).

$$\underline{a} = \left\{ \begin{array}{c} a(x_1) \\ \vdots \\ a(x_i) \\ \vdots \\ a(x_\infty) \end{array} \right\}, a \in \mathcal{L}_0, \quad \underline{\mathbf{T}} = \left\{ \begin{array}{c} \mathbf{t}_{(1)} \\ \vdots \\ \mathbf{t}_{(i)} \\ \vdots \\ \mathbf{t}_{(\infty)} \end{array} \right\}, \mathbf{a} \in \mathcal{L}_1 \text{ and } \underline{\underline{\mathbb{A}}} = \left\{ \begin{array}{c} \mathbf{A}_{(1)} \\ \vdots \\ \mathbf{A}_{(i)} \\ \vdots \\ \mathbf{A}_{(\infty)} \end{array} \right\}, \mathbf{A} \in \mathcal{L}_2 \tag{3.2}$$

A state has a close resemblance to a second order tensor in the sense that they both map vectors into vectors, but there are indeed a few very important differences that separate states from tensors. A state is not generally a linear or continuous function of $\boldsymbol{\xi}$ and while the real Euclidean space $\mathcal{V}$ is infinite-dimensional, the real Euclidean space $\mathcal{L}_2$ is of dimension 9, since the second order tensor can only represent 9 different stresses acting on a material point (Silling et al., 2007).

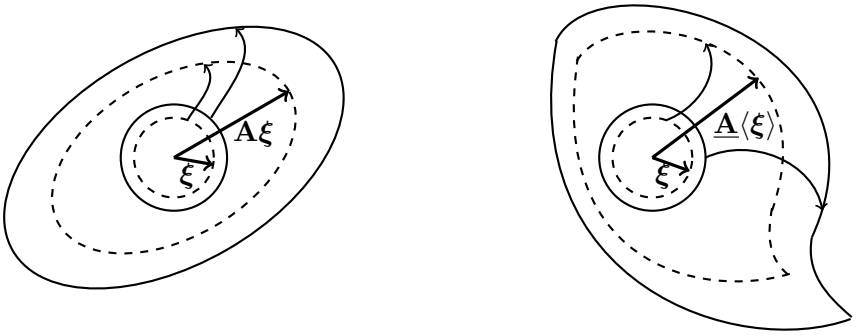

Symmetric tensor $\mathbf{A}$ Vector State $\underline{\mathbf{A}}$

FIGURE 3.4: A symmetric tensor maps a sphere into an ellipsoid, while a state can map a sphere into a complex and discontinuous surface (Silling et al., 2007).

3.2.2 Reference and deformed configuration

The ordinary state based peridynamic theory uses states to represent the referencing and deformation of the bonds between particles. The best way to describe this theory is by looking at the reference and deformed configuration.

The reference positions of $\boldsymbol{x}$ and $\boldsymbol{x}'$ are shown as vectors that point from the origin of the geometry. The bond vector $\boldsymbol{\xi}$ points from the material point under consideration, at $\boldsymbol{x}$, to the material material point $\boldsymbol{x}'$ and $\boldsymbol{\xi}$ can be obtained by subtracting the two reference vectors. It should be kept in mind that $|\boldsymbol{\xi}|$ should always be smaller than δ for the bond vector to be included in the horizon $\mathcal{H}_{\boldsymbol{x}}$.

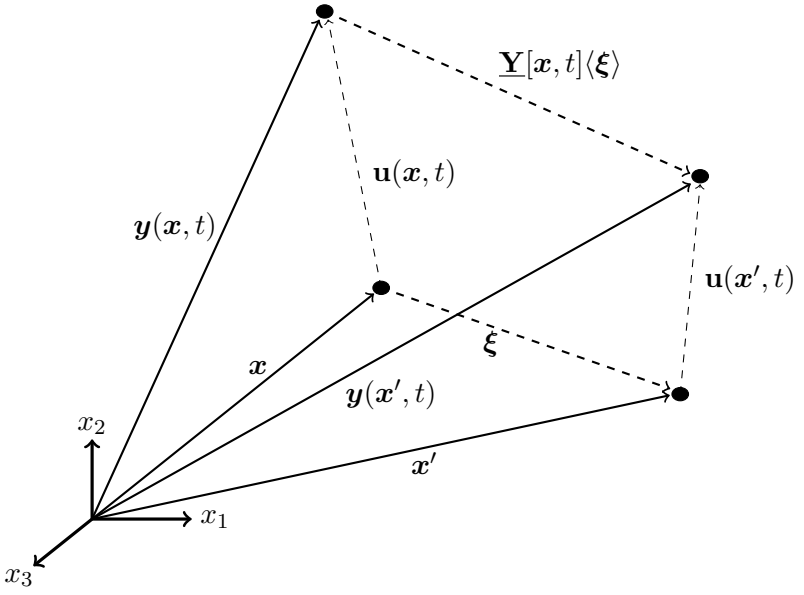

FIGURE 3.5: Reference and deformed configurations of peridynamic states.

$$\boldsymbol{\xi} = \boldsymbol{x}' - \boldsymbol{x} \tag{3.3}$$

The reference position vector state that operates on $\boldsymbol{\xi}$ in the initial configuration can be defined as:

$$\underline{\mathbf{X}}\langle\boldsymbol{\xi}\rangle = \boldsymbol{\xi}. \tag{3.4}$$

The deformed coordinates $\boldsymbol{y}$ as a result of displacement $\mathbf{u}$ can be seen as a function of position and time $\boldsymbol{y}(\boldsymbol{x},t)$, that gives the new coordinates of the displaced material points, which are merely the sum of the initial position vector $\boldsymbol{x}$ and the local displacement vector $\boldsymbol{u}(\boldsymbol{x},t)$.

$$\boldsymbol{y}(\boldsymbol{x},t) = \boldsymbol{x} + \boldsymbol{u}(\boldsymbol{x},t) \tag{3.5}$$

Where the deformation vector state $\underline{\mathbf{Y}}$ that operates on $\boldsymbol{\xi}$ can be represented as the difference between the global deformation functions.

$$\underline{\mathbf{Y}}[\boldsymbol{x},t]\,\langle\boldsymbol{\xi}\rangle = \boldsymbol{y}(\boldsymbol{x}+\boldsymbol{\xi},t) - \boldsymbol{y}(\boldsymbol{x},t) \tag{3.6}$$

3.2.3 Force density in a linear elastic solid

Interactions between pairs of material points can be given in the form of force densities, with a measure of force per unit volume squared. These force densities are obtained by the inter-particle force function $\mathbf{f}$ in (3.1), but for the ordinary state based theory, the force densities for each material point is represented by a scalar state based force function $\underline{t}$. Since $\underline{t}$ is a scalar state and the direction for each quantity differs, a unit vector state $\underline{\mathbf{M}}$ is introduced, which contains the unit directional vectors for each scalar force function. When multiplied with $\underline{t}$ as in (3.7), the vector state based force function $\underline{\mathbf{T}}$ can be obtained.

$$\underline{\mathbf{T}} = \underline{\mathbf{M}}\,\underline{t} \tag{3.7}$$

Where $\underline{\mathbf{M}}(\underline{\mathbf{Y}})\langle \boldsymbol{x} - \boldsymbol{x}' \rangle$ is a unit vector that points from the deformed position of $\boldsymbol{x}$ to the deformed position of $\boldsymbol{x}'$ and from Silling et al. (2007), the force scalar state for a peridynamic linear elastic solid can be taken as:

$$\underline{t} = \frac{-3\rho}{q}\underline{\omega}\,\underline{x} + \alpha\underline{\omega}\,\underline{e}^d, \tag{3.8}$$

where $\rho = -k\theta$ is the peridynamic pressure, q the weighted volume, $\underline{\omega}$ the influence function that can be assumed to be of unit value for the work in this thesis, $\underline{x}$ the reference position scalar state, $\underline{e}^d$ the deviatoric extension scalar state, θ the dilatation and k and $\alpha = 15\mu/q$ the material parameters. The bulk modulus can be represented by k and the shear modulus by μ.

The reference position scalar state, $\underline{x} = |\underline{\mathbf{X}}|$ can simply be seen as the magnitude of the reference vector state. The same holds for the deformation vector state that has a magnitude of $\underline{y} = |\underline{\mathbf{Y}}|$. Moreover, the deviatoric extension scalar state comes from the extension scalar state, $\underline{e} = \underline{y} - \underline{x}$ that can be computed as:

$$\underline{e}^d = \underline{e} - \underline{e}^i = \underline{e} - \frac{\theta\underline{x}}{3}, \tag{3.9}$$

where the dilatation θ is the volumetric strain due to all contributions from the extension scalar state $\underline{e}$ and can be denoted as:

$$\theta(\underline{e}) = \frac{3}{q}(\underline{\omega}\,\underline{x}) \bullet \underline{e}. \tag{3.10}$$

In order to define the dot operator used on peridynamic states, assume two vector states $\underline{\mathbf{A}}$ and $\underline{\mathbf{B}}$. The dot product of these vector states can be obtained by integrating over the point product of all vectors $\underline{\mathbf{A}}\langle\boldsymbol{\xi}\rangle$ and $\underline{\mathbf{B}}\langle\boldsymbol{\xi}\rangle$ contained in the horizon $\mathcal{H}$.

$$\underline{\mathbf{A}} \bullet \underline{\mathbf{B}} = \int_{\mathcal{H}} (\underline{\mathbf{A}}\underline{\mathbf{B}}) \langle\boldsymbol{\xi}\rangle \, dV_{\boldsymbol{\xi}} \tag{3.11}$$

Lastly, the weighted volume q is a function of the distance $\underline{x}$ of material points $\boldsymbol{x}'$ that interact with material point $\boldsymbol{x}$, and can be denoted as:

$$q = (\underline{\omega}\,\underline{x}) \bullet \underline{x} \tag{3.12}$$

Since θ and q are both functions of states, their scalar values for a material point $\boldsymbol{x}$ can be obtained by integrating over the horizon $\mathcal{H}_{\boldsymbol{x}}$.

3.2.4 Strain energy density

In the following two sections a simplistic derivation for the peridynamic governing equation will be given. It should however be noted that this derivation is somewhat unorthodox, due to the fact that it will be approached from the already discretized meshless method by Silling and Askari (2005). Although the peridynamic theory is a continuous non-local theory, the main aim of this derivation is to explain the governing equation in a simplistic manner which can be better understood from the practical discretized point of view.

Due to displacement between material points, a certain micropotential w (Joule per volume squared) develops for each interaction. These micropotentials are a function of the displacements of the material points relative to each other and can be denoted as $w(\underline{y})$. When assuming a material point with a reference configuration of $\boldsymbol{x}$ and a deformed configuration of $\boldsymbol{y}$, all other points in the horizon $\mathcal{H}_{\boldsymbol{x}}$ will then be referred to with a deformed configuration of $\boldsymbol{y}^i$. Then the strain energy density for point $\boldsymbol{x}$ can be obtained by

$$W = \frac{1}{2} \sum_{i=1}^{\infty} \frac{1}{2} \left(w(\underline{y}) + w^i(\underline{y}^i) \right) V_i, \tag{3.13}$$

where all micropotentials of material points in the horizon $\mathcal{H}_{\boldsymbol{x}}$ are summed and multiplied by the volume V_i of each material point (Madenci and Oterkus, 2014). This gives

an expression for the strain energy density W for each point, which will be used in the derivation of the governing equation, as well as, the derivation for the damage model.

3.2.5 Governing equation

The peridynamic equation of motion can be derived from the principle of virtual work:

$$\delta \int_{t_0}^{t_1} (T - U)dt = 0, \tag{3.14}$$

where U is the potential energy and T is the kinetic energy. This can be solved by using Lagrange's equation, where $L = T - U$.

$$\frac{d}{dt}\left(\frac{\partial L}{\partial \dot{\mathbf{u}}_k}\right) - \frac{\partial L}{\partial \mathbf{u}_k} = 0 \tag{3.15}$$

The total potential and kinetic energy in a solid body can be obtained by summing over the energy contributions for all material points in the body. Where the total kinetic energy can be expressed as:

$$T = \sum_{i=1}^{\infty} \frac{1}{2}\rho_i \dot{\mathbf{u}}_i \bullet \dot{\mathbf{u}}_i V_i \tag{3.16}$$

and the total potential energy as:

$$U = \sum_{i=1}^{\infty} W_i V_i - \sum_{i=1}^{\infty} (\mathbf{b}_i \bullet \mathbf{u}_i) V_i. \tag{3.17}$$

When substituting (3.13) into (3.17) for a material point $\boldsymbol{x}_k$ and then substituting (3.16) and (3.17) into (3.15), the Lagrange equation can now be written as:

$$\rho_k \ddot{\mathbf{u}}_k = \sum_{j=1}^{\infty} \frac{1}{2} \frac{\partial w_k}{\partial \underline{y}^j} V_j - \sum_{j=1}^{\infty} \frac{1}{2} \frac{\partial w_j}{\partial \underline{y}^k} V_j + \mathbf{b}_k. \tag{3.18}$$

From Silling et al. (2007), these expressions can then be rewritten in terms of force densities (contained in force scaler states $\underline{t}$) of material point $\boldsymbol{x}_k$ acting on material points $\boldsymbol{x}_j$ and vice versa.

$$\rho_k \ddot{\mathbf{u}}_k = \sum_{j=1}^{\infty} (\underline{t}^k - \underline{t}^j) V_j + \mathbf{b}_k \tag{3.19}$$

When assuming that the volume V_j of each material point is infinitesimally small, the infinite summation can be expressed as an integral over the horizon of $\boldsymbol{x}_k$. When substituting $\boldsymbol{x}_k$ for $\boldsymbol{x}$ and $\boldsymbol{x}_j$ for $\boldsymbol{x}'$, and adding the unit directional term for each force density as in (3.7), the equation of motion can be written as:

$$\rho(\boldsymbol{x})\ddot{\mathbf{u}}(\boldsymbol{x},t) = \int_{\mathcal{H}_{\boldsymbol{x}}} \{\underline{\mathbf{T}}[\boldsymbol{x},t]\langle \boldsymbol{x}' - \boldsymbol{x}\rangle - \underline{\mathbf{T}}[\boldsymbol{x}',t]\langle \boldsymbol{x} - \boldsymbol{x}'\rangle\} dV_{\boldsymbol{x}'} + \mathbf{b}(\boldsymbol{x},t) \tag{3.20}$$

In this paper the focus will be on quasi-static analysis, thus excluding the inertial term $\rho(\boldsymbol{x})\ddot{\boldsymbol{u}}(\boldsymbol{x},t)$ in (3.20). In addition, when assuming static equilibrium, it can be shown that the inertial term can be neglected (Silling et al., 2007).

3.3 Application of the state based peridynamic theory

When applying the peridynamic theory, a variety of factors exist that can cause variations in the final solution and these have to be treated carefully in order to ensure that the physical problem is captured correctly. The following will describe how to apply the peridynamic theory and especially focus on some pitfalls that can be encountered in the process.

3.3.1 Spatial discretization

Peridynamics can be discretized using the meshless approach of Silling and Askari (2005), where the spatial discretization does not have to be in the form of a structured mesh, however, the volume that each material point occupies, needs to be known. In this sense, it is convenient to discretize the geometry into different sub domains or cells, analogous to finite elements. These can be in the form of lines, quadrilaterals, triangles, hexahedrons, tetrahedrons or wedge shaped cells (Madenci and Oterkus, 2014). An algorithm can then be implemented to compute the centroid and volume of each cell, where the centre of each cell will denote the reference position for the material point representing the cell. It should, however, be kept in mind that the chosen shape will have an effect on the amount of immediate neighbours for each material point, especially if the solution must converge to the classical local solution where $\mathcal{H}$ goes to zero. The spacing of these discrete material points is very important, since it defines; the length scale that needs to be used, the amount of processing power required for numerical operations, as well as, the asymmetrical behaviour of fracture propagation (Henke and Shanbhag, 2014).

When dealing with problems that contain stress intensities around crack tip areas, as well as large geometries that will be to computationally intensive for uniform refinement, the need exists for a refinement process where more than one length scale can be implemented and where seamless transition can be obtained from one length scale to the other. The only way to achieve this is by introducing a non-constant horizon (Bobaru and Ha, 2011). In peridynamics, there can be three kinds of numerical convergence with respect to refinement. The first is m-convergence (see Figure 3.6(a)), where δ (the horizon radius) is fixed and $m \to \infty$, where $m = \delta/r$ and r being the cell radius of the material point. This numerical approximation will normally converge to the exact non-local solution. Secondly is δ-convergence (see Figure 3.6(b)), where m stays fixed and $\delta \to 0$. The solution based on δ-convergence, will normally converge to an approximation of the classical solution. Lastly there is (δm)-convergence, where $\delta \to 0$ and m increases as δ decreases. This approximation will normally converge to the analytic peridynamic solution which converges to the classic solution and is especially useful in problems containing regions with stress intensities (Ha and Bobaru, 2010). In other work by **?** it has been shown that when increasing δ faster than r will give less error when uniformly refined discretizations are considered, in this work the relationship between δ and r will be of constant nature due to the inclusion of non-uniform discretizations. In essence, any numerical formulation will show some kind of convergence to a more accurate solution, when the discretization is refined. Thus, the ability to capture convergence to either the classical or non-local solution is vital in developing a robust numerical formulation. Due to this, these different types of convergence will be extensively analysed in this thesis and it will form part of the main discussion, regarding the applicability of the peridynamic formulation for obtaining an accurate displacement solution.

It should be noted that the work mentioned above is mainly based upon the bond-based theory, where the micromodulus of the specific material has to be altered as δ decreases (Bobaru et al., 2009). For the ordinary state based theory, this alteration to the material properties is not needed, since the constitutive law is not applied on individual bonds as in the bond-based theory.

3.3.2 Boundary conditions

The state based peridynamic theory has four different kinds of boundary conditions that can be applied. These include velocity, displacement, uniform pressure through bond interactions and lastly body force density as an external contribution. In this research the focus is on a quasi-static model, thus the velocity boundary condition will not be discussed here. Boundary conditions can either be applied in the force vector state term

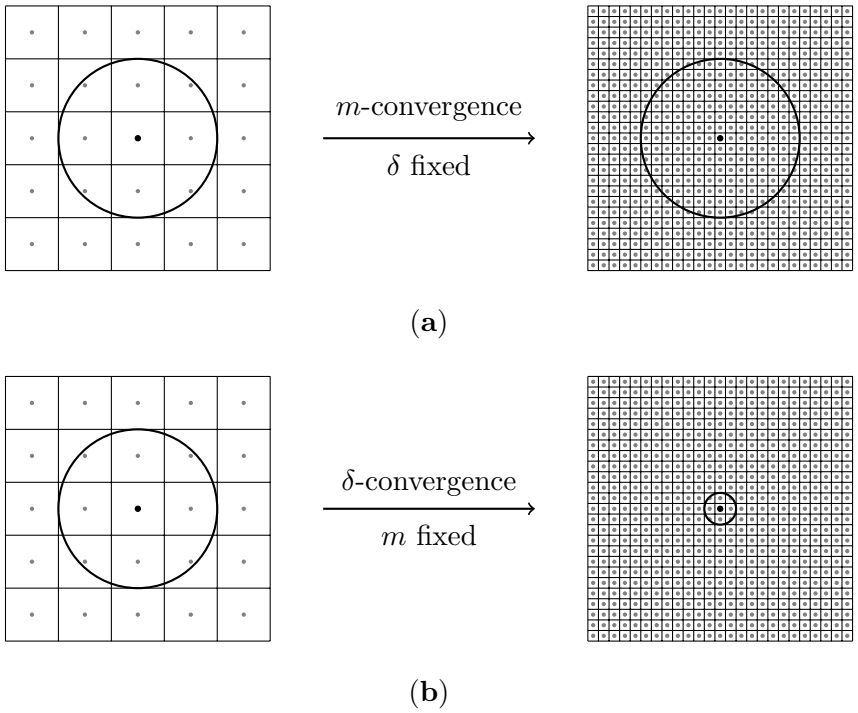

FIGURE 3.6: Graphical descriptions for (a) m-convergence and (b) δ-convergence. (Ha and Bobaru, 2010)

$\underline{\mathbf{T}}[\boldsymbol{x}]\langle \boldsymbol{x}' - \boldsymbol{x}\rangle$ or as an external body force density through term $\mathbf{b}(\boldsymbol{x})$ in the ordinary state based governing equation.

Displacement constraints

Initial displacement fields can easily be introduced into the governing equation by altering the deformation vector state through the use of a prescribed displacement vector $\mathbf{U}_0$, where:

$$\mathbf{u}(\boldsymbol{x}) = \mathbf{U}_0. \tag{3.21}$$

Displacement constraints are normally prescribed through a fictitious boundary region $\mathcal{R}_c$, with a width of at least 2δ, to ensure that the material behaviour is captured properly. These boundary regions should also have exactly the same material properties as the region that is constrained.

Uniform pressure through bond interactions

The fact that the force scalar state has already been split into a dilitational and deviatoric term makes it quite easy to introduce an extension that can account for uniform effective pressure. This can be applied directly in the force scalar state field. Since this

boundary condition will only contribute to the dilitaional deformation, it can simply be added to the peridynamic pressure from (3.8).

$$p = -k\theta + \lambda p_f \tag{3.22}$$

In this added term p_f represents the effective pressure (e.g. pore pressure from fluid leakoff) and λ is a pressure coefficient. It should be noted that this added term is positive, since the sign convention for tension in peridynamics is positive. The applied fluid pressure will create tension in the bond interactions causing bulk expansion of the material (Turner, 2013).

External body force density

Load application through externally applied loads, like uniform pressure and point loads, must be approached in a different manner when using the peridynamic theory than in classical solid mechanics. This characteristic is mainly due to the non-locality of the peridynamic theory, where not only neighbouring interactions can be utilized to apply a load, but all material point interaction in the specified horizon. In solid mechanics, one can apply a traction on a continuous surface of a certain domain, but when non-local theories are considered, the interaction through which the load is applied is not through a surface, but all volumes contained in the horizon. In this sense a traction on a surface can not be implemented directly in the peridynamic theory, as it does not directly appear in the governing equation (3.20).

To illustrate this, consider a region Ω divided into two fictitious domains Ω^+ and Ω^-, on which an external force is exerted. In order for equilibrium to be satisfied, a net force $\mathbf{F}^+$ exerted on Ω^- by Ω^+ has to exist. In classical solid mechanics, this force can be obtained by integrating a traction $\mathbf{T}$ over the intersecting surface area $\delta\Omega$.

$$\mathbf{F} = \int_{\delta\Omega} \mathbf{T} dA \tag{3.23}$$

Since the interaction zone spans beyond the plane of the the nearest neighbours in the peridynamic governing equation, the net force $\mathbf{F}^+$ has to be obtained by integrating the force densities $\mathbf{L}(\boldsymbol{x})$ over the volume of all points in Ω^+.

$$\mathbf{F} = \int_{\Omega^+} \mathbf{L}(\boldsymbol{x}) dV \tag{3.24}$$

Where $\mathbf{L}(\boldsymbol{x})$ defines the force densities acting on the material points in Ω^+.

$$\mathbf{L}(\boldsymbol{x}) = \int_{\Omega^-} \left[\mathbf{t}(\mathbf{u}' - \mathbf{u}, \boldsymbol{x}' - \boldsymbol{x}) - \mathbf{t}'(\mathbf{u} - \mathbf{u}', \boldsymbol{x} - \boldsymbol{x}')\right] dV \tag{3.25}$$

If the volume of Ω^- is zero, the resulting integration will also lead to zero, thus surface tractions and point forces can not be applied as boundary conditions in the peridynamic theory, since they have no volume (Madenci and Oterkus, 2014).

Due to the above mentioned, external force contributions can only be applied as a body force density field $\mathbf{b}(\boldsymbol{x})$. This external contribution can be applied through a fictitious boundary region $\mathcal{R}_l$ with a thickness of at least 2δ, to make sure that all applied force is accounted for. For coarse discretizations, these fictitious regions can have a great effect on the accuracy of the solution and it will be analysed and discussed in this research.

3.3.3 Damage model

The most interesting feature about the peridynamic theory is the ability to predict damage and fracture without any external criteria or enrichment functions. Although many damage models exist, the one in this thesis is approached by including a stretch parameter s, where:

$$s(\boldsymbol{\xi}) = \frac{(\underline{y} - \underline{x})\langle\boldsymbol{\xi}\rangle}{\underline{x}\langle\boldsymbol{\xi}\rangle} = \frac{\underline{e}\langle\boldsymbol{\xi}\rangle}{\underline{x}\langle\boldsymbol{\xi}\rangle}, \tag{3.26}$$

denotes the stretch of a bond $\boldsymbol{\xi}$. In order for damage to occur, the bond $\boldsymbol{\xi}$ has to stretch beyond a certain point where the material will yield or fail, due to the bond stretch exceeding the yield or tensile strain capacity of the material. This point is called the critical stretch s_c and it can be used to either weaken the bond stiffness, in the case of an elastic-plastic material or eliminate the bond stiffness, in the case of linear elastic brittle failure. For brittle fracture, this can be done by using a boolean bond damage function function $\mu_d(\boldsymbol{\xi})$, where:

$$\mu_d(\boldsymbol{\xi}) = \begin{cases} 1 & \text{if } s(\boldsymbol{\xi}) < s_c \\ 0 & \text{otherwise.} \end{cases} \tag{3.27}$$

In this sense, s_c can be seen as a material property, based on the length scale, mechanical properties and the critical strain energy release rate of the material.

To quantify damage, Silling and Askari (2005) proposed that it should be seen as the ratio of the number of broken bonds to the original amount of bonds in a neighbourhood. The damage for a material point $\boldsymbol{x}$, can then be expressed as:

$$\phi(\boldsymbol{x}) = 1 - \frac{\int_{\mathcal{H}_{\boldsymbol{x}}} \mu_d(\boldsymbol{x}, \boldsymbol{\xi}) dV_{\boldsymbol{\xi}}}{\int_{\mathcal{H}_{\boldsymbol{x}}} dV_{\boldsymbol{\xi}}}, \tag{3.28}$$

where $0 < \mu_d(\xi) < 1$, implying that a damage value of 0 will indicate that all bonds connected to the material point $\boldsymbol{x}$ are still intact and a value of 1, that will indicate all bonds have been severed. In this sense, a material point should always have a damage factor less than 1, otherwise it is entirely disconnected from the material region, which will destabilize the stiffness matrix, causing numerical divergence. Some techniques have, however, been implemented to keep the stiffness matrix stable, these will be discussed in Chapter 4.

In order for a fracture to form, all bonds in a horizon crossing the plane of fracture need to be severed. For instance, if a fracture plane passes through the centre of a horizon $\mathcal{H}_{\boldsymbol{x}}$, the damage value $\phi(\boldsymbol{x})$ should be very close to 0.5, if the material points in $\mathcal{H}_{\boldsymbol{x}}$ are distributed uniformly. In this sense a damage value in the region of $0.3 - 0.5$ would be a clear indicator that some fracture plane has formed.

In order to obtain the critical stretch s_c, Silling and Askari (2005) shows the critical energy release rate G_c in terms of the bond-based theory.

$$G_c = \int_0^{\delta} \left\{ \int_0^{2\pi} \int_z^{\delta} \int_0^{cos^{-1}z/\xi} \left(\frac{1}{2} c\xi s_c^2 \xi \right) \sin\phi d\phi d\xi d\theta \right\} dz = \frac{1}{2} c s_c^2 \left(\frac{\delta^5 \pi}{5} \right) \tag{3.29}$$

Where G_c is a summation of the work done, to terminate all bonds crossing the fracture surface. In this case, c represents a micropotential (N/m^6), that defines the stiffness of the bond interactions.

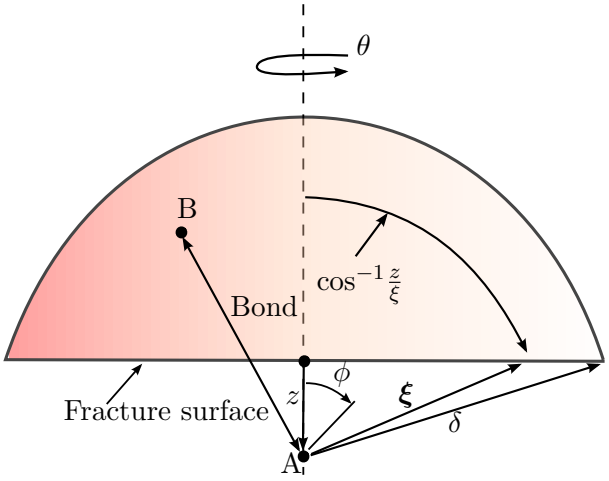

FIGURE 3.7: The energy release rate can be computed by summing over all bonds (AB) that cross the fracture surface Silling and Askari (2005).

From (3.29), the critical stretch can be written in terms of G_c (Madenci and Oterkus, 2014; Silling and Askari, 2005), for the 3D as well as the 2D case.

$$s_c = \begin{cases} \sqrt{\dfrac{G_c}{(3\mu + (\frac{3}{4})^4(\kappa - \frac{5\mu}{3}))\delta}} & 3D \\ \sqrt{\dfrac{G_c}{(\frac{6}{\pi}\mu + \frac{16}{2\pi^2}(\kappa - 2\mu))\delta}} & 2D \end{cases} \tag{3.30}$$

3.3.4 Numerical solution

Stiffness matrix

In order to obtain the numerical solution for the peridynamic system of equations, a stiffness matrix $\mathbf{K}$ has to be assembled in order to represent the stiffness contribution of each material point. It should be noted that other methods exist, where no stiffness matrix is required and these will not be presented due to the scope of this work. Equation (3.18) in Section 3.2.5 shows that the force density state for a certain material point $\boldsymbol{x}_k$, can be obtained by deriving the strain energy micropotentials with respect to the deformed scalar state $\underline{y}$. This representation is very simplified and put in context of one material point only. In general, over the global system the force vector state $\underline{\mathbf{T}}$ can be represented as:

$$\underline{\mathbf{T}}[\boldsymbol{x}] = \nabla W(\underline{\mathbf{Y}}[\boldsymbol{x}], \boldsymbol{x}), \tag{3.31}$$

where ∇ refers to the Frêchet derivative of the strain energy density function W, with respect to the deformation vector state $\underline{\mathbf{Y}}$ (Silling et al., 2007). In the same way, when taking the second Frêchet derivative of W with respect to $\underline{\mathbf{Y}}$, the modulus double state $\underline{\underline{\mathbb{K}}}$ can be obtained as:

$$\underline{\underline{\mathbb{K}}}[\boldsymbol{x}] = \nabla\nabla W(\underline{\mathbf{Y}}[\boldsymbol{x}], \boldsymbol{x}), \tag{3.32}$$

where $\underline{\underline{\mathbb{K}}}$ can be seen as analogous to the fourth order elasticity tensor in the classical theory. In essence, $\underline{\underline{\mathbb{K}}}$ represents an array of matrices which is then assembled according to the global index of each material point, to form a global stiffness matrix $\mathbf{K}$ (Mitchell, 2011*a*,*b*).

The method mentioned above, will be the analytically correct way to compute the stiffness matrix $\mathbf{K}$, but obtaining the second Frêchet derivative of the energy density function is a very complicated task. To simplify this, one can simply perturb every neighbour

of every material point, one at a time, by using a finite differencing scheme. In this way, the stiffness of each material interaction can be obtained and stored in the global stiffness matrix.

Solution techniques

Since the peridynamic theory is based on a governing equation which involves dynamic failure, explicit transient time integration is the most popular scheme to obtain the numerical solution. On the other hand, when a quasi-static problem is considered, a different approach needs to be taken. Although time integration can be used to solve a quasi-static problem by using Adaptive Dynamic Relaxation (ADR) (Kilic and Madenci, 2010; Underwood, 1983). When using ADR, the peridynamic equation of motion is rewritten as a set of differential equations:

$$\mathbf{D}\ddot{\mathbf{U}}(\mathbf{X},t) + c_f\mathbf{D}\dot{\mathbf{U}}(\mathbf{X},t) = \mathbf{F}(\mathbf{U},\mathbf{U}',\mathbf{X},\mathbf{X}'), \tag{3.33}$$

where $\mathbf{D}$ is a fictitious diagonal density matrix and c_f a fictitious damping term implemented to get the dynamic solution to converge to a steady state solution as fast as possible. The diagonal density matrix can be obtained from the stiffness matrix $\mathbf{K}$, compiled from the system of material point interactions and the damping coefficient can be be obtained as a function of the current displacement $\mathbf{U}$ and $\mathbf{K}$.

Another approach is to implicitly solve the static equation by building a stiffness matrix from bond interactions and solving for the displacements where:

$$\mathbf{K}\mathbf{U}(\mathbf{X}) = \mathbf{F}(\mathbf{U},\mathbf{X}). \tag{3.34}$$

Two system solution techniques will be used in this research, namely the Conjugate Gradient (CG) solver (Hestenes and Stiefel, 1952) and the General Minimal Residual (GMRES) solver (Saad and Schultz, 1986). These are available in the Belos library (Bavier et al., 2014). The main difference between these solution techniques is that the CG solver can only solve symmetric matrices and the GMRES solver can solve non-symmetric matrices. Since the CG solver only solves symmetric matrices, the solution process is more efficient and convergence is faster. However, large amounts of damage can result in loss of positive definiteness of the stiffness matrix, which causes divergence in the CG solver. The CG solver is a useful tool to obtain displacement solutions, however, when large scale damage is simulated a more robust solver, such as the GMRES solver, will better fit the purpose.

Chapter 4

Numerical Implementation

4.1 Model and assumptions

In theory, the peridynamic model should have a great advantage over other numerical models, since the governing equation is designed to deal with fracture related issues. Although the mathematical concept is sound, very little literature exists where the theory is successfully applied to fluid driven fracture related problems. Because of this, extensive research is still required to find a suitable method to successfully apply the peridynamic theory. For this reason, the model that is described here is based on very simplified conditions, to ensure that the basic framework of the model can be verified systematically. In time, this will lead to a more robust model that can accurately predict fluid driven fracture.

As discussed in Chapter 2, LEFM can be assumed on the basis of Small Scaled Yielding (SSY) and in this particular case, given that the micro cracking region around the fracture tip is very small compared to the rest of the formation, it is quite clear that the scale of yielding is very small compared to linear elastic deformation. In this case, only linear elastic brittle fracture propagation will be assumed.

The peridynamic model is based on a 2D plane strain formulation, where it is assumed that Mode I fracture propagation will be the governing fracture mode (Asadi et al., 2013). This assumption can be made when considering an infinite homogeneous material at very high confining pressure. Since displacement is very restricted in these conditions, it is assumed that the only displacement worth mentioning is that which is caused by the opposing crack faces opening in Mode I fracture propagation. Mode II and Mode III fracture propagation will only show in a heterogeneous material, where there is already a presence of natural flaws. In addition a vast number of experimental observations,

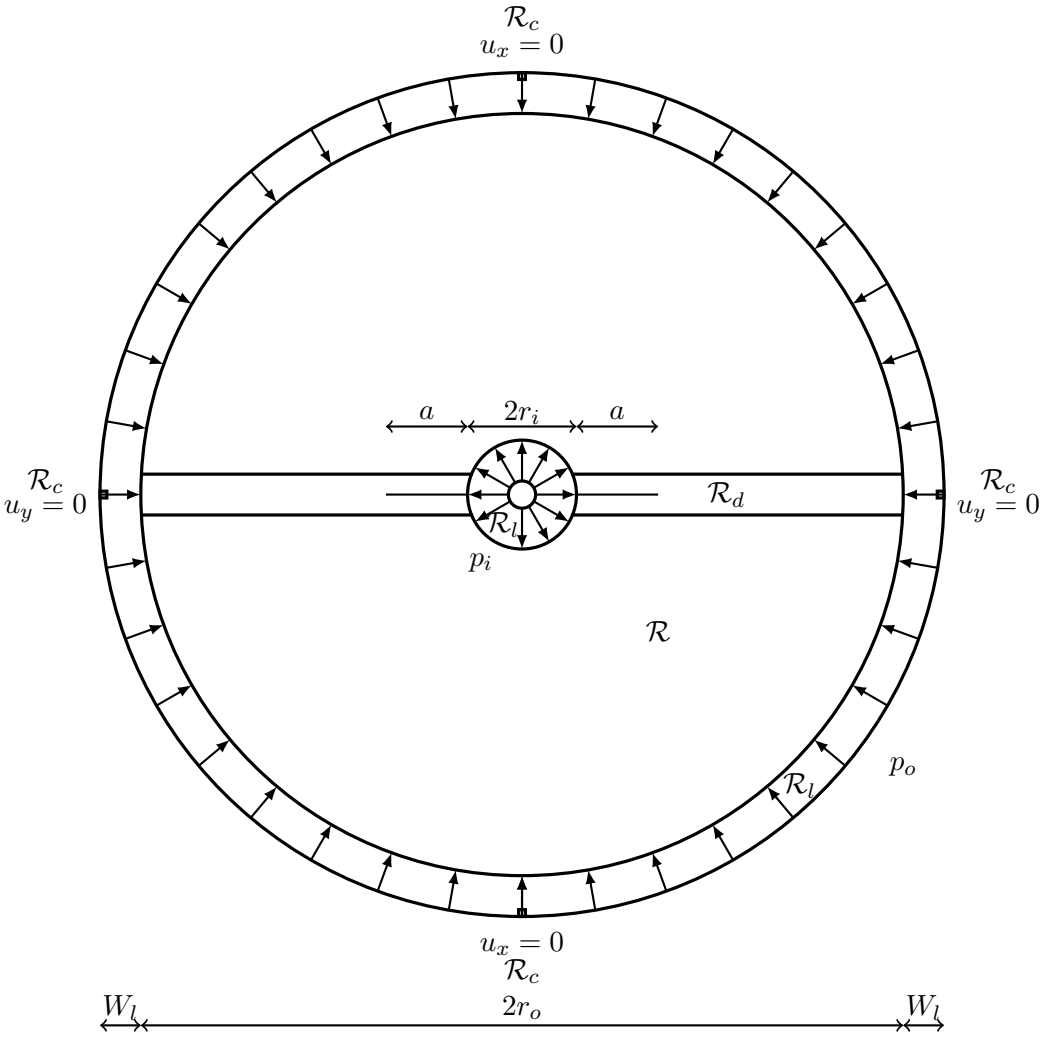

FIGURE 4.1: Geometry for the peridynamic model.

as summarised by Kazerani (2011), indicate that Mode I tensile fracture is indeed the governing mode for rock materials, even in situations where Mode II loading is applied.

4.1.1 Geometry and boundary conditions

The peridynamic model is based on standard core specimen dimensions, such as used in laboratory sleeved fracture experiments (Brenne et al., 2013) and can be considered as a simplified version of the Rummel & Winter model, where the far field stresses are equal in both directions and can be represented by a radial confining pressure. The geometry of the model is illustrated in Figure 4.1.

The parameters in Figure 4.1 can be described as follows: where r_i is the borehole radius, r_o the outer radius of the sample, a the initial crack length, p_i the internal pressure applied on the surface of the borehole and p_o the far field confining pressure applied on the outside surface of the cylinder. Both p_i and p_o are applied as body

loads through the region $\mathcal{R}_l$ with a width equivalent to the horizon diameter $W_l = 2\delta$. Displacement boundary conditions u_x and u_y are applied through the boundary regions $\mathcal{R}_c$, to constrain the body against rotation. Furthermore, the specimen can be divided into two material regions, where $\mathcal{R}$ denotes the material region where no damage can occur and $\mathcal{R}_d$, the material region where the damage model is implemented. It should be noted that not all forms of loading in this research require external fictitious boundary conditions and in this case the geometry stays the same, except for omitting all load regions $\mathcal{R}_l$. When using the Rummel & Winter analytic model for a circular plate of finite radius, it should also be noted that the analytical solution will only be valid for an initial crack length $a < (r_o - r_i)/10$ (r_i and r_o as defined in Figure 4.1). This is because the boundary conditions for an infinite plate and the thick walled cylinder differ, where the amount of constraint in the thick walled cylinder decreases as the crack length increases, the amount of constraint in the infinite plate stays the same. The a-limit is the zone where the simplified Rummel & Winter solution is not valid, due to the difference between a thick walled cylinder and an infinite plate and this will further be discussed in Chapter 5. Geometric and material parameters will be given in each section, where a different variant of the basic model is explained. Various other geometries that were used for verification will be presented in Chapter 5. These consist of simple block tests and variations of the geometry shown in Figure 4.1.

4.1.2 Discretization

When the discretization of the geometry is considered, the damage region $\mathcal{R}_d$ is shortened for fracture initiation and kept as in figure 4.1 for fracture propagation. The reason for shortening $\mathcal{R}_d$ is mainly to include less refinement in the model, since the damage zones are more refined in order to capture a better resolution for fracture propagation. To ensure minimum error, the damage region is refined to a length scale that would best represent the material and the influence of the initial crack tip. For shale rock, the average particle size is in the region of $60\,\mu m$, thus a refinement in the region of $\Delta = 0.02 - 0.05\,mm$ would best represent this material. Another factor is the initial crack length a, where the Rummel & Winter hydraulic fracturing model suggest that when a gets very small, the breaking pressure needed for initial fracture increases quite dramatically. To capture this phenomena, the refinement in the damage area near the inner radius of the cylinder should be at least as small as the average particle size in order to get a good resolution of the effects of small a.

Due to the refinement needed for this particular model, non-uniform mesh refinement has to be implemented with a varying horizon size. The effects that this might have on the resulting solution will be quantified in a radial displacement test as discussed in

Chapter 5. Another approach to minimising the effects of a varying horizon size will be to ensure a smooth transition in material point size, as this will limit the amount of numerical integration error over the horizon. To achieve this, all cell shape quality values will at least be kept in the region of 0.98. All of the above can be neglected when using the internal force stencil method, described in Section 4.2.3 and an irregularly discretized geometry will be used in this regard, to prove that all inaccuracies due to non-local behaviour can be eliminated. Since irregularities will amplify the error that can normally be associated with a non-local theory, the irregular discretization will serve as a verification measure for the internal force stencil method.

4.1.3 Material parameters

Material parameters that will be used in this specific model, include the bulk modulus K, shear modulus μ and the critical energy release rate G_c. These material parameters can be obtained in various ways. The bulk and shear modulus can be obtained from uni-axial and tri-axial tests, which gives the static modulus of elasticity E_{stat} (Further denoted as E) and Poisson ratio ν. From these parameters, the following relations exist to calculate the bulk and shear modulus:

$$k = \frac{E}{3(1-2\nu)} \tag{4.1}$$

and for plane strain:

$$\kappa = \frac{E}{2(1-\nu)} \tag{4.2}$$

and:

$$\mu = \frac{E}{2(1+\nu)}. \tag{4.3}$$

Another approach, is to measure the ultra-sonic compressional wave (p-wave) velocity v_p (Horsrud, 2007), which combined with the dry bulk density (ρ_d) provides the p-wave modulus M:

$$M = \rho_d {v_p}^2 \tag{4.4}$$

and by solving (4.5) and (4.6), a very accurate representation of the true bulk modulus and shear modulus can be obtained. This method is especially useful for in-situ testing conditions.

$$k = M - \frac{4\mu}{3} \tag{4.5}$$

$$\mu = \frac{3kE}{9k - E} \tag{4.6}$$

For the fracture mechanics material properties, a large variety of tests exist to obtain the fracture toughness (K_{IC}) value of the specific material. Some of these perform better in the field of rock fracture mechanics, when considering the time and difficulties associated with the preparation of each specimen. Of these, the most practical would be the core based tests, like the chevron notched short rod (SR), the hollow pressurised cylinder (PC), the disc shaped compact specimen (DS(T)) and the single edge cracked or chevron edge cracked round-bar-in-bending (SECRBB, CENRBB) (Ingraffea et al., 1976). Each of these test methods have been calibrated with the appropriate geometric functions, to obtain the K_{IC} value from experimental results.

When the K_{IC} value of the material is known, the G_{IC} value can be calculated from (4.7), which is derived from the stress intensity approach.

$$G_{IC} = \frac{{K_{IC}}^2}{E} \tag{4.7}$$

4.1.4 Critical stretch

The peridynamic stretch (s) can be related to the classical strain tensor ($\boldsymbol{\epsilon}$) for a bond vector $\boldsymbol{\xi}$, by:

$$s(\boldsymbol{\xi}) = \frac{\underline{e}\,\langle \boldsymbol{\xi} \rangle}{\underline{x}\,\langle \boldsymbol{\xi} \rangle} \equiv \frac{\partial u(\boldsymbol{\xi})}{\partial \boldsymbol{\xi}} = \boldsymbol{\epsilon}^{\boldsymbol{\xi}}, \tag{4.8}$$

where $\underline{e}$ is the extension scalar state, $\underline{x}$ the reference position scalar state and u a displacement function. In addition, the critical stretch parameter s_c can also be seen as the maximum tensile strain (ϵ_t) that a material can withstand. This would be the optimum way to attain s_c when modelling an experimental problem, but when considering the theoretical behaviour of homogeneous materials under any condition, s_c can be obtained by using the critical energy release rate (G_{IC}) as a material property in (3.29), as described in Chapter 3.

4.2 Load application

From Chapter 3, it is clear that load application on a peridynamic solid, especially when considering tractions on a surface and point forces, should be approached in a different manner than in classical solid mechanics. In this section, three different approaches to the application of surface pressure to the inside of a borehole wall will be explained. These methods will be analysed in order to obtain the best candidate for use on the peridynamic damage model, which will ultimately conclude the research objective.

4.2.1 Pressure on a surface

Since it is impractical to apply a surface traction on a peridynamic solid, the aim is to apply an identical body force density $\mathbf{f}$ through a material region $\mathcal{R}_l$ (see Figure 4.1) which is in contact with the "surface" where the traction is required. The net force exerted through region $\mathcal{R}_l$ should be equal to that of the surface traction $\mathbf{T}$. From the divergence theorem, (4.9) can be obtained.

$$\int_{\mathcal{R}_l} \mathbf{f}\, dV = \int_{\delta\mathcal{R}_l} \mathbf{T}\, dA \tag{4.9}$$

When assuming that $\mathcal{R}_l$ is a full cylinder with a unit height, the line integral can be split into two surfaces, where r_i is the radius of the inner ring surface and r_o the radius of the outer ring surface. By using a cylindrical coordinate system, (4.9) can be evaluated as follows:

$$\begin{aligned} \int_0^1 \int_0^{2\pi} \int_{r_i}^{r_o} \mathbf{f} r\, dr d\theta dz &= \int_0^1 \int_0^{2\pi} \mathbf{T} r_o\, d\theta dz \\ \pi \left(r_o^2 - r_i^2\right) \mathbf{f} &= 2\pi r_i \mathbf{T} \\ \mathbf{f} &= \frac{2\mathbf{T} r_o}{\left(r_o^2 - r_i^2\right)}. \end{aligned} \tag{4.10}$$

The constant body force density $\mathbf{f}$ can now be applied over $\mathcal{R}_l$, in order to simulate a constant pressure distribution over the inner surface of the cylinder material region $\mathcal{R}$. It should be noted that the material properties for both $\mathcal{R}_l$ and $\mathcal{R}$ remain the same and since it is not entirely clear whether $\mathcal{R}_l$ should be internally located in $\mathcal{R}$ as part of the solid, or externally located next to $\mathcal{R}$ as an additional boundary block. The extra material stiffness contribution by $\mathcal{R}_l$ might have significant effects, depending on the coarseness of the discretization.

4.2.2 Body force field through entire domain

When considering the difficulties and error associated with the application of an external force on a peridynamic solid, through a boundary condition, an energy minimization method was devised to eliminate external loads on boundaries. The aim of this method is to eliminate variables, such as load region stiffness, introduced when using boundary conditions and in effect have a more direct approach to load application, in order to verify the damage model. Achieving exact solutions for load displacement problems when using peridynamics, is in itself a difficult task. Thus, implementing a more direct method should decrease the chance for an inaccurate displacement solution and in effect have a less detrimental effect on the damage prediction capabilities of the model.

The approach to obtain a more accurate displacement solution, is to apply a body force density field $\mathbf{f}(r)$ over $\mathcal{R}$, which can be derived from the analytic stress field $\boldsymbol{\sigma}(r)$. The body force density can be obtained by taking the divergence of the analytic stress field.

$$\begin{aligned}\mathbf{f}(r) &= \nabla \bullet \sigma_{rr}(r)\mathbf{n} \\ &= \frac{1}{r}\frac{\partial(r\sigma_{rr}(r))}{\partial r}\mathbf{n}\end{aligned} \tag{4.11}$$

Where the analytic stress field, as a function of r applied only in the direction of r, can be obtained by:

$$\sigma_{rr}(r) = \frac{r_i^2 p_i}{r_0^2 - r_i^2}\left(1 - \frac{r_0^2}{r^2}\right) \tag{4.12}$$

and $\mathbf{n}$ denotes the direction in cylindrical coordinates, where:

$$\mathbf{n} = \begin{Bmatrix} 1 \\ 0 \\ 0 \end{Bmatrix}. \tag{4.13}$$

The final body force density function applied over $\mathcal{R}$ can then be taken as:

$$\mathbf{f}(r) = \frac{r_i^2 p_i (r^2 + r_0^2)}{r^3(r_0^2 - r_i^2)}\mathbf{n}. \tag{4.14}$$

4.2.3 Internal force stencil through entire domain

When applying the peridynamic theory through the meshless approach, a range of variables exist that can have an effect on the displacement solution. For instance, the discretization of the continuous solid will yield an error in the order of δ^2. Irregularities in cell shapes and sizes can cause numerical integration error. In addition, an inaccurate representation of the cylindrical horizon shape at surfaces can induce some form of error. When considering all these variables, it becomes challenging to obtain an accurate solution for complex problems, by using the peridynamic theory. In response to this, it was decided to quantify this error in terms of an internal force density stencil $\mathbf{f}_s$ (where the term stencil is used in order to define all error associated with using a certain discretization), which is obtained when applying a prescribed analytic displacement field $u_a(r)$ to the peridynamic governing equation.

$$\mathbf{f}_s = \mathcal{L}u_a(r) \tag{4.15}$$

Where $\mathcal{L}$ denotes the peridynamic operator and can be seen as the right hand side of (3.18) minus the body force contribution $\mathbf{b}(\boldsymbol{x}, t)$, operating on the displacement field. This resulting internal force density stencil ($\mathbf{f}_s$) will then contain all error contributions resulting from δ^2 and surface effects.

$$\mathbf{f}_s = \mathbf{f}(r) + \lambda_s(r)\mathbf{f}_e \tag{4.16}$$

Where $\mathbf{f}(r)$ is the analytic body force density field as a function of r, $\mathbf{f}_e$ is the error stencil and $\lambda_s(r)$ a scaling function. In this way the error can be quantified by comparing $\mathbf{f}$ to $\mathbf{f}_s$ for a simple problem and when fracture is introduced, the applied $\mathbf{f}$ will be scaled accordingly with the internal force density error stencil where:

$$\mathbf{f}(r) = \mathbf{f}_s - \lambda_s(r)\mathbf{f}_e. \tag{4.17}$$

When considering the method of manufactured solutions, the method above is similar except that it is not entirely used as a verification tool and in addition to this a local analytical solution is used in a non-local system in order to define the needed internal forces that will best suit the non-local system. This method will eliminate most inaccuracies that accompany the peridynamic displacement solution and given that the displacement solution is very accurate, in turn the peridynamic damage model can be utilised to its full potential.

4.3 Implicit vs. explicit formulation

As explained in Chapter 3, the main difference between the implicit and explicit solution techniques, is that the implicit technique builds a stiffness matrix from material particle interactions and uses a block solver to solve for the displacement, where explicit integration is used to solve the dynamic equation by means of the finite difference method. Various properties of these methods will be discussed below, in terms of practicality for implementation in the solution of the sleeved hydraulic fracture model.

4.3.1 Time scales

When modelling in a quasi-static time frame, there is the advantage of choosing the time scale in which the load is applied. This allows the problem to be simulated in a short time frame, for when the analyst wishes to simulate dynamic fracture propagation in high resolution. In addition, it also allows the problem to be simulated in a long time frame, for when the analyst wishes to simulate a fracture size, corresponding to the amount of energy applied to the system, irrespective of the simulation time or path that the crack follows, to reach the ultimate state. When modelling sleeved hydraulic fracture, which is a stable form of brittle fracture, the time scale for a specimen to completely fail can easily move into the order of hundreds of seconds (Brenne et al., 2013). This is illustrated in Figure 4.2, which shows the experimental results obtained for sleeved hydraulic fracture, where P_{AE} (denoted as p_b in the rest of this thesis) is the fracture initiation pressure and P_b the maximum applied pressure until the specimen fails. Fracture events are measured through monitoring the amount of acoustic emissions per half second. This result is only for a standard size core specimen in a laboratory experiment, when real hydraulic fracturing operations are considered, the time scale can move to the range of hours (Machala et al., 2012).

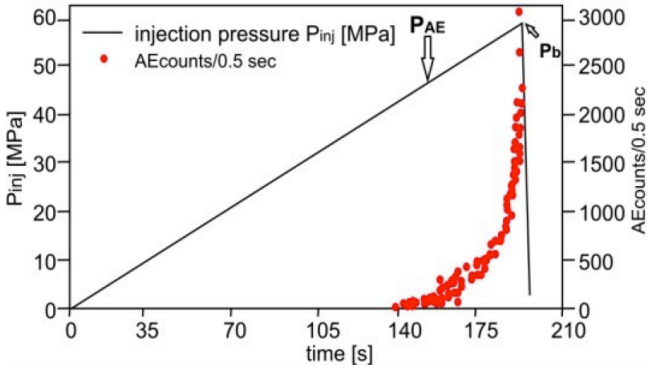

FIGURE 4.2: Acoustic emissions and applied pressure vs. time, for fracture propagation in a sleeved hydraulic fracturing experiment (Brenne et al., 2013).

4.3.2 Convergence

An implicit solution technique may require extra attention in the form of manually imposed conditions, since this is a very complicated procedure, factors such as loss of positive definiteness of the stiffness matrices or overly relaxed boundary conditions can have a big influence on numerical convergence. This is not advantageous with respect to the robustness of explicit integration, when large-scale damage or even disintegration of the geometry is considered. When considering stability of the solution technique, explicit integration is most applicable, but it comes at a high cost.

A non-symmetric stiffness matrix is normally encountered when material point interaction pairs do not share the same horizon, as depicted in Figure 4.3. This is only encountered when variable horizon sizes are used, for instance when using non-uniform refinement, or unstructured discretizations. The non-symmetric nature can be eliminated by mutually enforcing pairs of bonds to be included in their respective neighbourhoods. Caution should however be taken when doing this, since it essentially changes the shape of the horizon, which in turn introduces some amount of numerical integration error over the specific horizon.

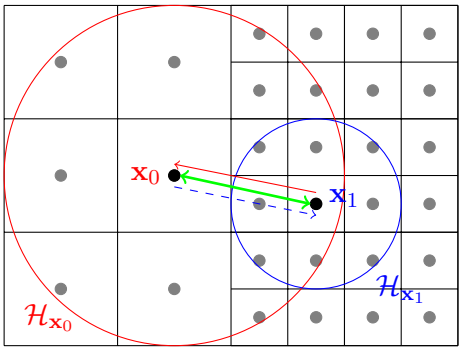

FIGURE 4.3: Bond pairs that do not share the same horizon.

When some material points sustain damage to the point where only one bond is still intact, the solution for the stiffness matrix loses positive definiteness, because there are no rotational constraints left at these material points. In effect these material points can spin freely as depicted in Figure 4.4. To solve this, material points are rotationally constrained in the case where only one bond is intact.

4.3.3 Computing efficiency

Since the explicit schemes are only conditionally stable for a certain maximum time step size, the amount of iterations before numerical convergence is reached, can increase

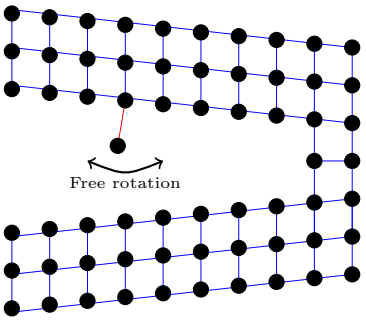

FIGURE 4.4: Material point with only one bond intact and no rotational constraint exists.

vastly with respect to the amount of iterations needed when implicitly solving for displacements. In this sense, the implicit solving technique will be more advantageous when problems such as sleeved hydraulic fracture is concerned. Even when ADR (Chapter 3) is used, the amount of iterations needed for convergence of a static problem is still two orders of magnitude more than the amount of iterations needed for an energy minimization technique, such as the implicit CG solver, as illustrated in Figure 4.5. With this in mind, it is evident that the implicit solution technique is best suited for the problem at hand.

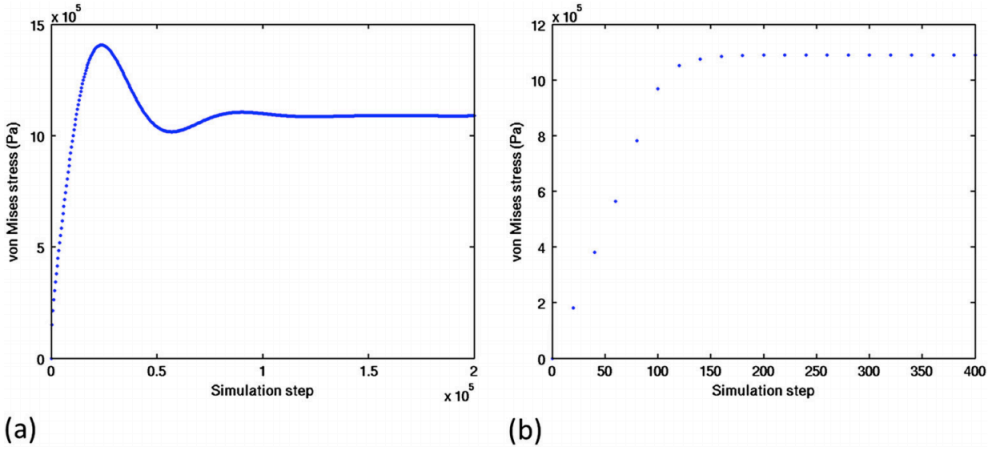

FIGURE 4.5: Numerical convergence for (a) dynamic relaxation and (b) energy minimization (Le et al., 2014).

Another factor to consider is the type of convergence used to obtain the closest approximation to the analytical solution. Chapter 3 discusses the difference between δ-convergence and m-convergence and it can be shown through the number of material point interactions needed for a certain level of refinement, that m-convergence is more expensive than δ-convergence. In Figure 4.6, the refinement of a 1x1 mm square plate is considered, where the number of material point interactions for each convergence type is plotted as a function of the refined grid spacing Δ.

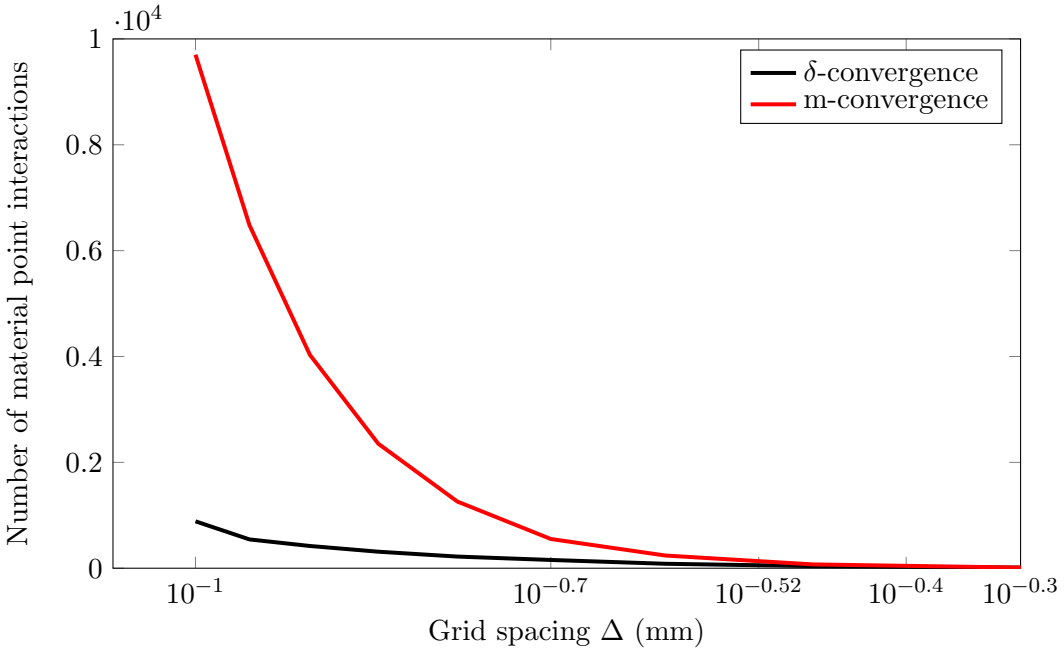

FIGURE 4.6: Number of material interactions as a function of grid spacing Δ for a 1x1mm plate.

4.4 The effect of model dimensionality

From Section 4.3 above, it is clear that the peridynamic theory can be computationally very expensive. Consequently, where applicable, models need to be simplified to two dimensional plane strain and plane stress problems. Since peridynamics is a non-local theory, where each material point is influenced by the strain energy density over a certain horizon around it, the shape of this horizon is very important. When the shape of this horizon changes, the effective strain energy density also changes and this causes some alterations in the derivation of the governing force density function. In addition, other behavioural changes can occur, due to the fact that the amount of material point interactions for each horizon level increase much faster in $\mathbb{R}^3$ than in $\mathbb{R}^2$. These can be observed through "surface" effects (Kilic, 2008; Madenci and Oterkus, 2014), or otherwise known as "skin" effects (Ha and Bobaru, 2011) and numerical integration error, when computing the weighted volume for each material point (Le et al., 2014).

4.4.1 Dilatation and shear parameters

The peridynamic force scalar state function $\underline{t}$, as described in Chapter 3, represents the force density state of all neighbouring material point interactions for a certain point in $\mathbb{R}^3$, where the constant α is derived by equalizing the peridynamic and classical strain energy densities (Silling et al., 2007). When this constant is considered in $\mathbb{R}^2$, for plane

stress and plane strain, it should be noted that instead of calculating the strain energy density over a spherical volume, it should be calculated over a cylindrical volume, where material points would lie on a flat plane resembling the entire thickness of the solid body. As a result of this, $\underline{t}$ should be derived from a cylindrical volume instead of a spherical volume. Additionally, since the strain tensor differs from plane strain to plane stress, different force scalar state functions can be obtained for each. In this case the focus will lie on plane strain.

The full derivation of the plain strain force scalar state $\underline{t}$ can be obtained in Appendix A. The derivation in Appendix A yields a force scalar state function:

$$\underline{t} = \frac{2k'\theta}{q}\underline{\omega}\,\underline{x} + \alpha\underline{\omega}\,\underline{e}^d, \tag{4.18}$$

where

$$k' = k + \frac{\mu}{3} \tag{4.19}$$

and

$$\alpha = \frac{8\mu}{q}. \tag{4.20}$$

In (4.19) and (4.20), k' represents the 2D plane strain peridynamic bulk modulus, k the classical 3D bulk modulus, μ the peridynamic and classical shear modulus, α the deviatoric constant and q the weighted volume.

4.4.2 Surface effects

The peridynamic governing equation is valid when it is assumed that the region over which integration takes place is completely embedded in the solid. However, when this region is intersected by either a surface or an interface, this assumption does not hold and in effect, the displacements obtained for material points with intersected neighbourhoods become non-physical. This phenomenon is referred to as surface effects. For instance, material point $\boldsymbol{x}_2$ and material point $\boldsymbol{x}_3$ in Figure 4.7, both have surfaces or interfaces intersecting their horizons. At these intersections, the material properties change, which will in effect change the strain energy density for the part of the volume that is intersected.

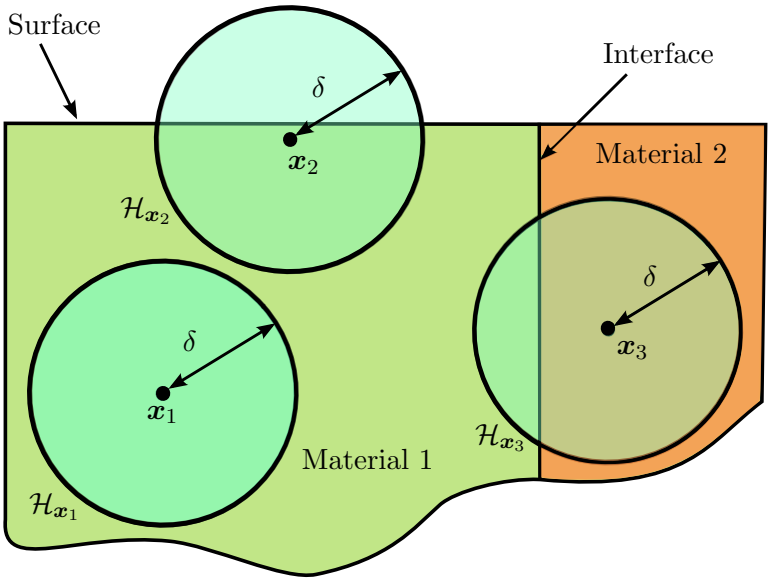

FIGURE 4.7: Surface and interface effects (Kilic, 2008).

Kilic (2008) proposed a solution where an uni-axial tension is applied on the body, after which measurement of the difference in force density of material points close to the surface and material points completely embedded in the solid is used as a scaling parameter. This method is accurate in numerically removing surface effects, however, an initial uni-axial tension would not necessarily give accurate directional dependent force densities when considering very complex geometries.

In this research, a method is used where the number of interactions in a neighbourhood is taken as a measurement of whether a point is close to a surface. A scaling factor is introduced as the number of interactions in a neighbourhood, divided by the maximum number of interactions recorded for any given single neighbourhood contained in the entire solid. In effect, when a neighbourhood intersects with a surface, the scaling factor will be less than one and reduce the resulting stiffness contributions from neighbouring material points. This method does not address the problem of interfaces with different material properties, but will indeed aid in the correction of surface effects for complex geometries.

4.4.3 Volume correction

In the derivation of the peridynamic governing equation (Chapter 3), it is shown that the infinite summation form can be rewritten in an integral form when assuming that the material points are infinitesimally small. If this assumption holds, the amount of error when computing the volumes of material points close to the horizon boundary would tend toward zero. This is however not the case, when applying the theory to coarser

discretizations, where material point volumes have finite size, as shown in Figure 4.8(a). In this case, only the cells where the centre point is inside the horizon, will contribute to the weighted volume for a certain cell. This is, in fact, not a true representation of the real weighted volume of a cell, since material points just inside the boundary will contribute too much volume and material points just outside the boundary will not contribute any volume, although part of their volume overlaps with the horizon.

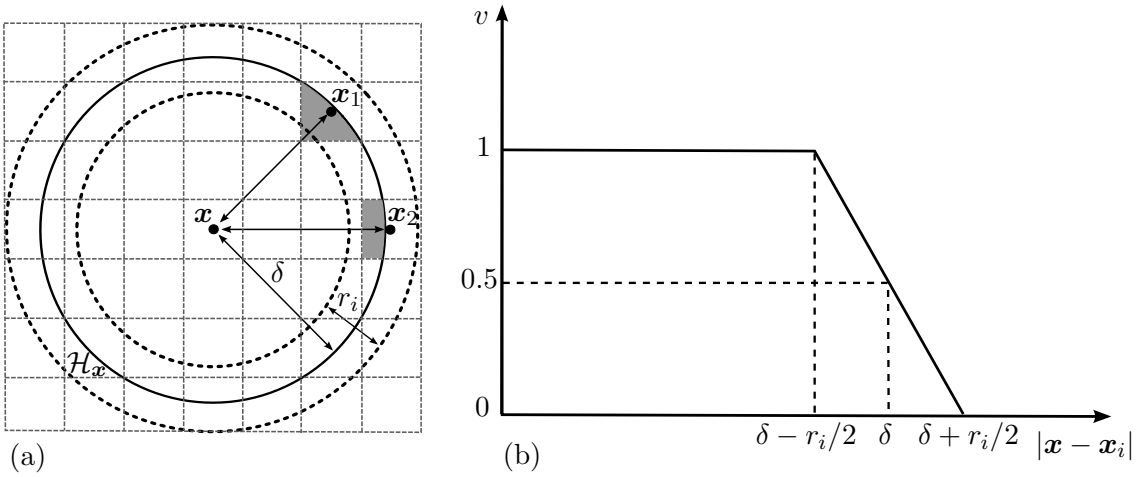

FIGURE 4.8: (a) 2D diagram showing discrete material points, where material point $\boldsymbol{x}_1$ is not fully included in $\mathcal{H}_{\boldsymbol{x}}$ and material point $\boldsymbol{x}_2$ is excluded but shares volume with $\mathcal{H}_{\boldsymbol{x}}$. (b) Volume fraction as a function of distance (Le et al., 2014).

In order to minimise this weighted volume error, Le et al. (2014) proposed a method where a linearly decreasing function of the distance $|\boldsymbol{x} - \boldsymbol{x}_i|$ provides a volume fraction ν for each material point situated in the zone $\delta \pm r_i/2$, as seen in Figure 4.8(b), where r_i denotes the cell radius of the i'th material point.

$$\nu(\boldsymbol{x} - \boldsymbol{x}_i) = \begin{cases} 1 & \text{if} \leq \delta - \frac{r_i}{2} \\ \frac{1}{2} + \frac{\delta - |\boldsymbol{x} - \boldsymbol{x}_i|}{r_i} & \text{if } \delta - \frac{r_i}{2} < |\boldsymbol{x} - \boldsymbol{x}_i| < \delta + \frac{r_i}{2} \\ 0 & \text{if} \geq \delta + \frac{r_i}{2} \end{cases} \tag{4.21}$$

When the weighted volume q is calculated, for every instance a material point $\boldsymbol{x}_i$ is included in the zone for volume correction, the volume fraction $\nu(\boldsymbol{x} - \boldsymbol{x}_i)$ is merely multiplied by the volume of $\boldsymbol{x}_i$.

4.5 Mesh dependency

When considering Sections 4.4.2 and 4.4.3 above, it is evident that accuracy of the horizon, and the volume it contains, is an integral part of accurate peridynamic modelling.

Consequently, the question of the effect of alternate cell shapes and non-uniform discretizations can be raised. This issue is very seldom discussed in the literature. On the other hand, for the underlying purpose of this research, it is very important to understand the effects of choosing alternate cell shapes and non-uniform refinement, as it is of the very nature of a radial problem to rely on alternate meshing regimes and non-uniform refinement. Possible effects on displacements and the fracture propagation path will be discussed bellow.

4.5.1 Displacement

In Section 4.4.3 it was demonstrated that for finite cell sizes, a volume correction factor has to be implemented in order to obtain the correct numerical volume integration for each neighbourhood and subsequently obtaining the correct weighted volume for each material point. When volume correction is ignored, it can be shown that when δ increases, the weighted volume increases in a stepwise fashion. Where every step can be seen as a horizon level and this stepwise increase is simply due to more material points being contained in the horizon. When considering a uniform quadrilateral and triangular discretization, where all material points have a unit size, Figure 4.9 shows that the horizon levels differ largely as δ increases.

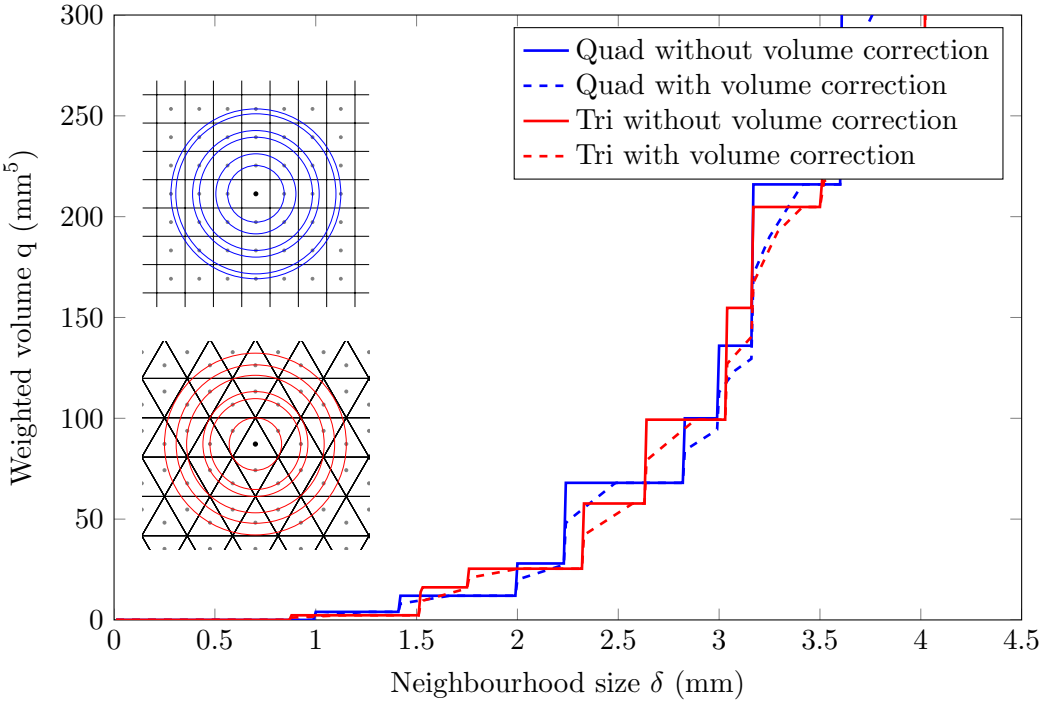

FIGURE 4.9: Weighted volume q as a function of horizon size δ for quadrilateral and triangular structured grids, with and without volume correction.

This difference of weighted volume values, demonstrates the large amount of error that can creep in without volumetric correction and indicates how different cell shapes can have an effect on the rate of convergence to the classical solution. In contrast to this, when volumetric correction is applied, it can be seen that the weighted volume increases more gradually and in effect increases the rate of convergence, as will be illustrated in Chapter 5.

4.5.2 Fracture propagation path

When the fracture propagation path is concerned and local neighbourhood sizes are implemented, structured meshing regimes can have an influence on the direction for fracture propagation, due to the symmetry of bond directions for each neighbourhood. This effect can be observed even with triangular discretization, as in Figure 4.10, which shows an instance of a triangularly discretized square plate with a local neighbourhood size under damage dependent force description. In this case, damage dependent force prescription is used to drive the crack in a similar way as a fluid under pressure, where a force is prescribed to a material point wherever a bond has been severed. This effect does however vanish as a result of numerical round off when the neighbourhood is of a more non-local nature.

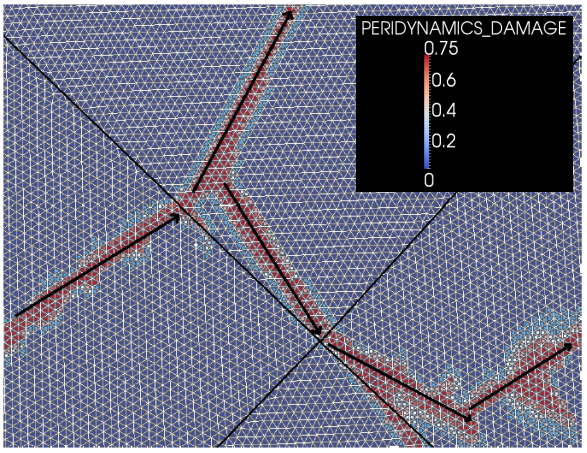

FIGURE 4.10: Mesh dependence occurs whenever a structured discretization is used with a local neighbourhood size.

Random fracture propagation can, however, be obtained for local neighbourhoods, when using irregular discretizations, such as delaunay triangulation, as in Figure 4.11, where the same plate and force prescription is used as in Figure 4.10. Care should however be taken when selecting the horizon size for these irregular disctretizations, as variable horizon sizes might influence symmetry of the stiffness matrix and volume correction might be impaired when a big variation exist in material point volumes.

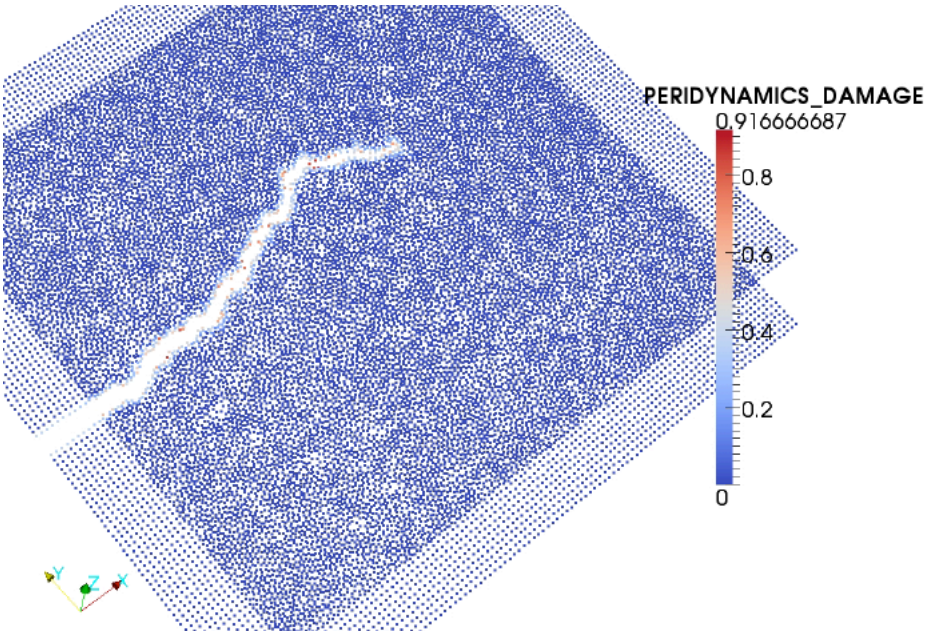

FIGURE 4.11: Random fracture when using delaunay triangulation.

4.6 Summary

In summary, the proposed peridynamic model for sleeved fracture will be based on the geometry of a standard thick walled cylinder and the governing formulation will be based on 2D plane strain. Mode I fracture will be considered as the governing mode of fracture and internal borehole pressure will be applied through three different pressure application techniques. The geometry will be discretized with quadrilaterals for fracture initiation and Delaunay triangles for fracture propagation. Non-uniform refinement, based on grain size, will be applied near the borehole. Material parameters includes the bulk modulus κ and shear modulus μ, based on p-wave measurements for fracture propagation and arbitrarily chosen for fracture initiation. The critical stretch will be derived from the critical energy release rate and if calibration is needed, it will be done by using the critical stretch factor f_s. Volume correction will be applied in all displacement verification models. All models will have a quasi-static time frame and will be solved implicitly, by either the CG or GMRES solution techniques. The code that will be used for all models is called *mingus* by Turner (2012).

Chapter 5

Verification of Benchmark Block Test

This Chapter consists of all verification tests that were completed, in order to, firstly understand the behaviour of a non-local theory and secondly, verify that the theory can be applied to obtain an accurate displacement solution. An in depth discussion on these results will follow in Chapter 7.

In order to compare the peridynamic damage model with analytical solutions from LEFM, it is crucial that the basic physics of the problem is captured accurately. There will be no use in verifying the peridynamic damage model if it is based on the wrong displacement solution, thus the block test will serve as a set of benchmark tests that will indicate if the current formulation is capable of capturing the constitutive law in a linear elastic material for very simplistic geometries. Essentially the purpose of this test is to use a non-local theory and determine if it will converge to the local solution. The first step will be to test the three dimensional version of the peridynamic model, as the two dimensional plane strain model is derived from the three dimensional version. Secondly, the plane strain formulation will be tested for various effects that can cause error in the displacement solution. These tests will then serve as the basic verification, to demonstrate the effects of alterations in the form of discretization and refinement.

5.1 3D

The aim of the 3D block test is mainly to verify the peridynamic displacement solution for a coarse discretization with only local neighbourhood size.

5.1.1 Test properties

A simple cube consisting of a homogeneous isotropic linear elastic material is used. The loading consists of a distributed tensile stress σ_{33} in the positive z-direction, applied as a body force through the region $\mathcal{R}_l$ acting on the region $\mathcal{R}$. The block is constrained in the z-direction through region $\mathcal{R}_c$. A schematic representation for the geometry of the problem is shown in Figure 5.1 and the geometrical and material parameters can be obtained in Table 5.1.

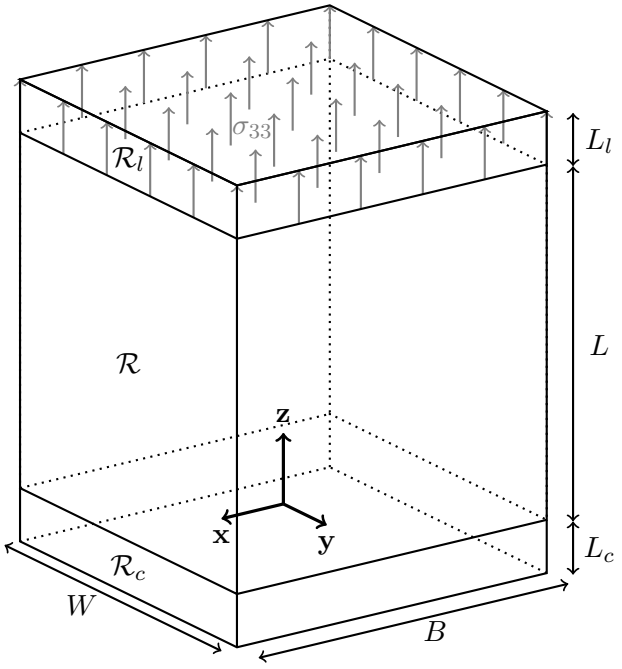

FIGURE 5.1: Geometry for 3D block, with applied tensile stress σ_{33}.

The analytic solution can be obtained by using basic stress strain relations, where the displacement in the z-direction parallel to the applied stress can be obtained by:

$$u_y(z) = \frac{1}{E}(\sigma_{33} z) \tag{5.1}$$

and the displacement in the x and y-direction, tangent to the applied stress by:

$$u_x(x) = u_y(y) = \frac{1}{E}(-\nu\sigma_{33} x). \tag{5.2}$$

It should be noted that all displacement values will be measured through the centre of the material region $\mathcal{R}$ and parallel to the respective axis.

TABLE 5.1: Test properties for 3D cube.

Parameter	Value	
Width	10	mm
Breadth	10	mm
Length	10	mm
L_c	1.5	mm
L_l	1.5	mm
Δ	0.5	mm
E	100	GPa
ν	0.25	
K	66.667	GPa
μ	40	GPa
σ_{33}	10	MPa

5.1.2 Results

Displacement values for the 3D block test can be obtained in Figure 5.2, where it is evident that the peridynamic solution shows good correlation with the analytic solution. It should however be noted that some error exist near boundary regions $\mathcal{R}_l$ and $\mathcal{R}_d$. This is most likely a result of surface effects. In addition to this, some form of oscillation in the displacement solution is evident and this is most likely the effect of zero energy modes in the implicit solution.

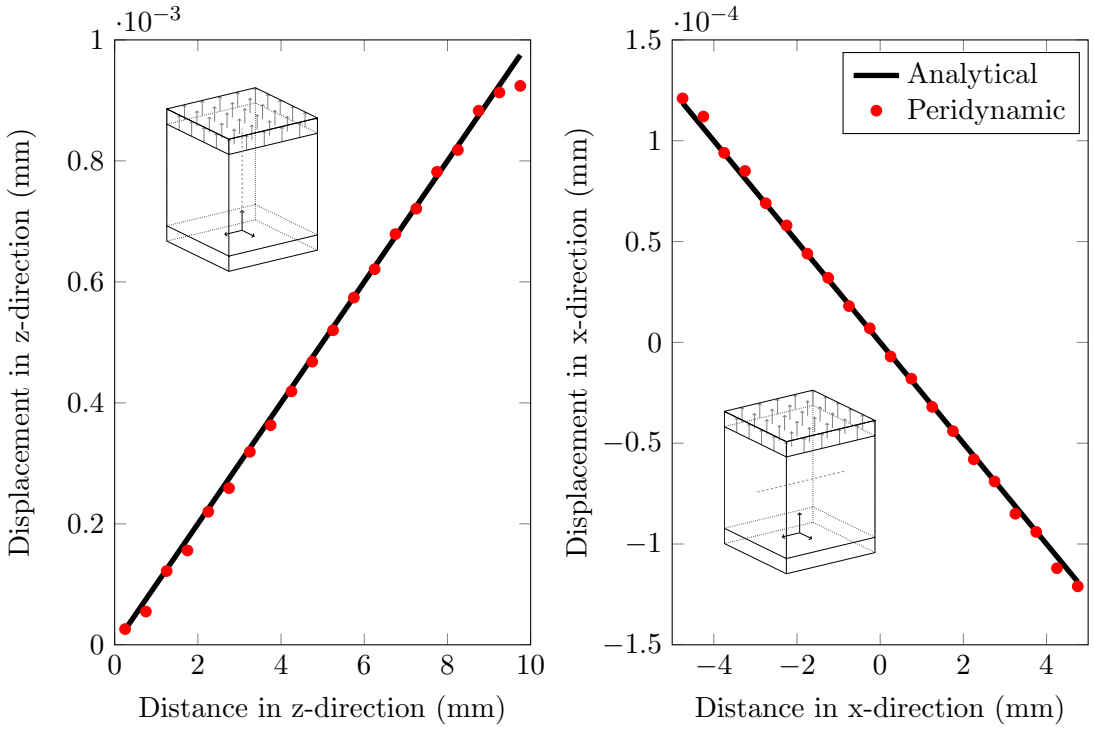

FIGURE 5.2: Displacement in the z and x-direction along the z and x-axis respectively.

5.2 2D plane strain

The 2D plain strain block test will have various functions in verifying that the quasi-static implicit peridynamic approach can yield accurate results for displacements in 2D plane strain. Firstly, m-convergence will be tested to acquire a horizon size to cell radius ratio which can best mimic the classical solution to the problem. Secondly, δ-convergence will be tested, to get the optimum resolution for the discretized solid. The effect of a varying poison ratio as well as non-uniform refinement will also be analysed. Finally, the implications of using different cell shapes, such as triangular shapes will be analysed, as random triangulation is a very useful tool when considering complex geometries.

5.2.1 Test properties

A simple square plate with unit thickness will be used for the 2D plane strain test. The bottom region $\mathcal{R}_c$ of the plate is constrained in the y-direction and a uniformly distributed tensile stress σ_{22} will act in the positive y-direction on the top region $\mathcal{R}_l$ as can be seen in Figure 5.3.

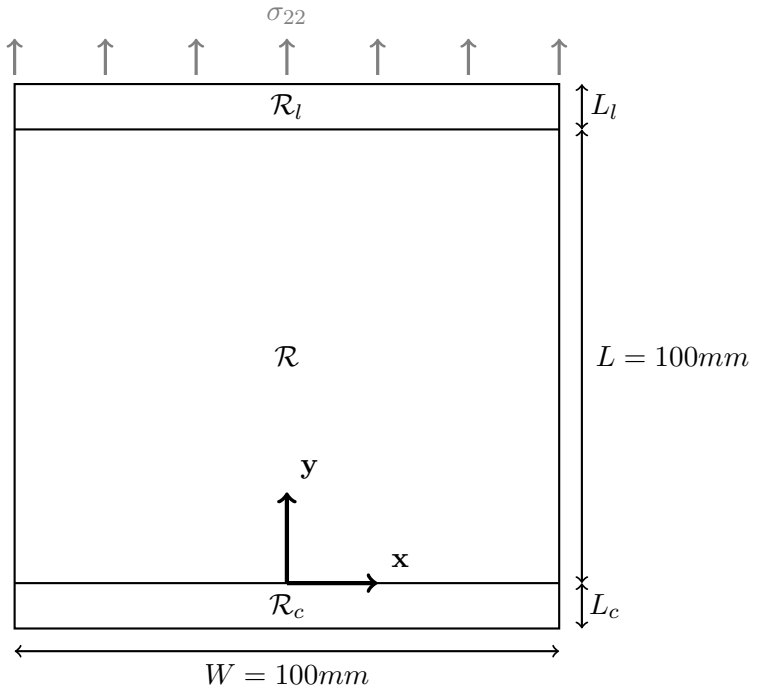

FIGURE 5.3: Geometry for square plate under tensile pressure σ_{22}.

The analytic solution can be obtained by using simple stress strain relations in 2D plane strain, where the displacement in the y-direction parallel to the applied stress can be obtained by:

$$u_y(y) = \frac{1}{E}\left[(1+\nu)(1-\nu)\sigma_{22}y\right] \tag{5.3}$$

and the displacement in the x-direction, tangent to the stress by:

$$u_x(x) = \frac{1}{E}\left[-\nu(1+\nu)\sigma_{22}x\right]. \tag{5.4}$$

Material and geometric properties for the square plate can be obtained in Table 5.2. It should however be kept in mind that the Poisson ratio will vary in Section 5.2.4.

TABLE 5.2: Test properties for square plate.

Parameter	Value	
Width	100	mm
Length	100	mm
L_c	12	mm
L_l	12	mm
Δ	0.5-4	mm
E	100	GPa
ν	0.25	
K	66.667	GPa
μ	40	GPa
σ_{22}	10	MPa

5.2.2 Convergence to classical solution

Firstly m-convergence is analysed by keeping $\delta = 4mm$ and varying the cell radius r to give m ranging from 2 to 8 where $m = \delta/r$. Convergence is verified by calculating the displacement in the y-direction on the x-axis intercept and the displacement in the x-direction on the y-axis intercept. The volume correction method was implemented in all 2D peridynamic models. For an indication of the effect that this method can have on the speed of convergence, Figure 5.4 shows the displacement solution for m-convergence without volume correction, while the solution with volume correction can be obtained in Figure 5.5.

From Figure 5.4 and 5.5, it can be seen that a m ratio of $m = 5$ gives a close representation of the classic solution even when the volume correction function is not implemented and this ratio is then used in the δ-convergence where δ tends to zero. Convergence is again verified by calculating the displacements as can be obtained in Figure 5.6, where it can be seen that the peridynamic displacement solution gradually converges to the analytic solution.

From Figure 5.7 it can be seen that convergence is not monotonic when no volume correction technique is implemented as it jumps around. In contrast, when the volume correction technique is implemented it can be seen that convergence is more smooth.

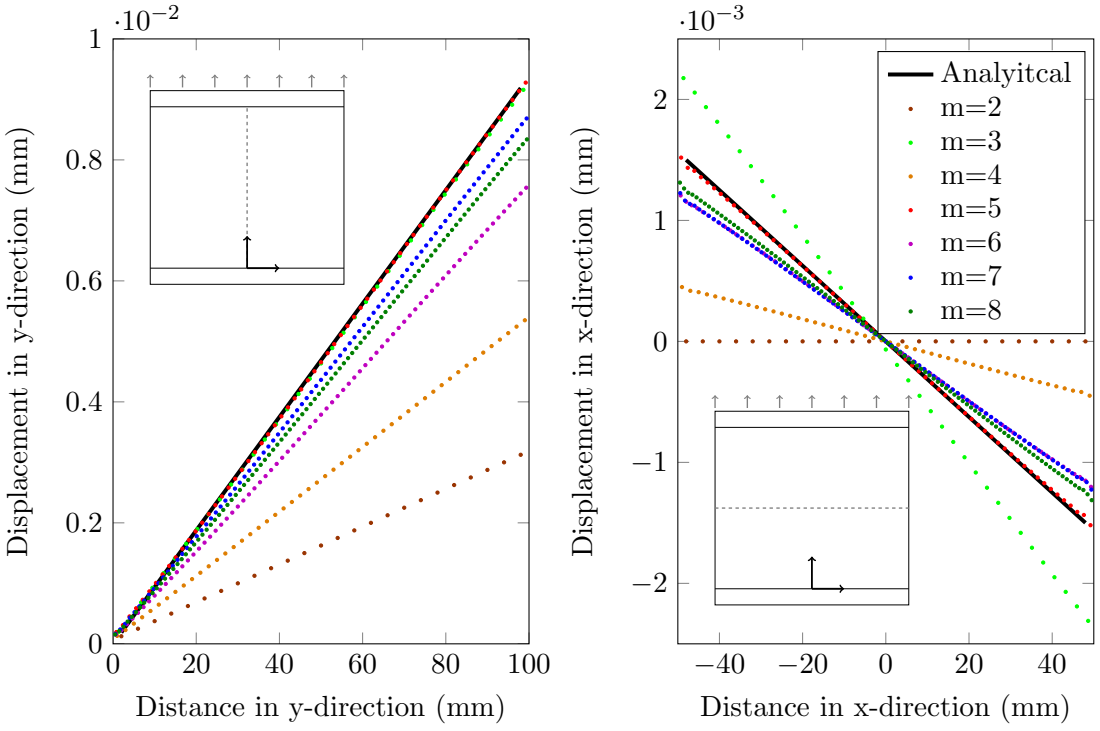

FIGURE 5.4: m-convergence of displacement solution in the y and x-direction, where $\delta = 4.0$ is fixed and no volume correction method used.

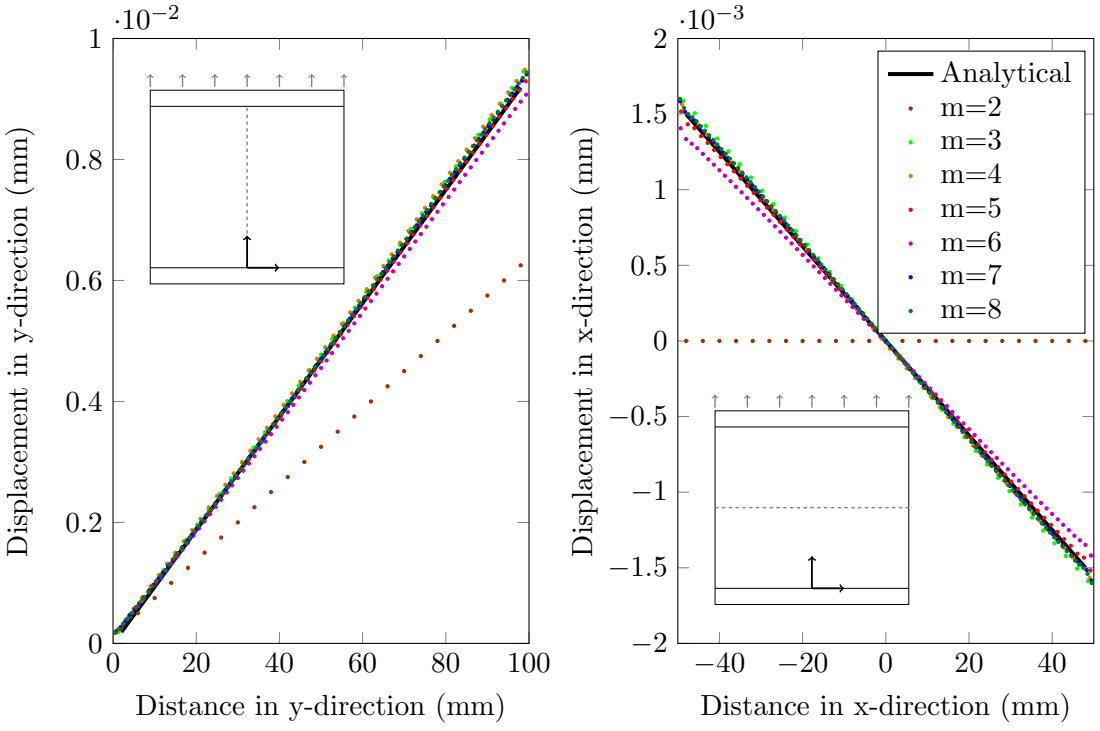

FIGURE 5.5: m-convergence for displacement in the y and x-direction where $\delta = 4.0$ is fixed.

Overall it would be rather challenging to quantify the rate of convergence due to the discontinuity of the convergence plot.

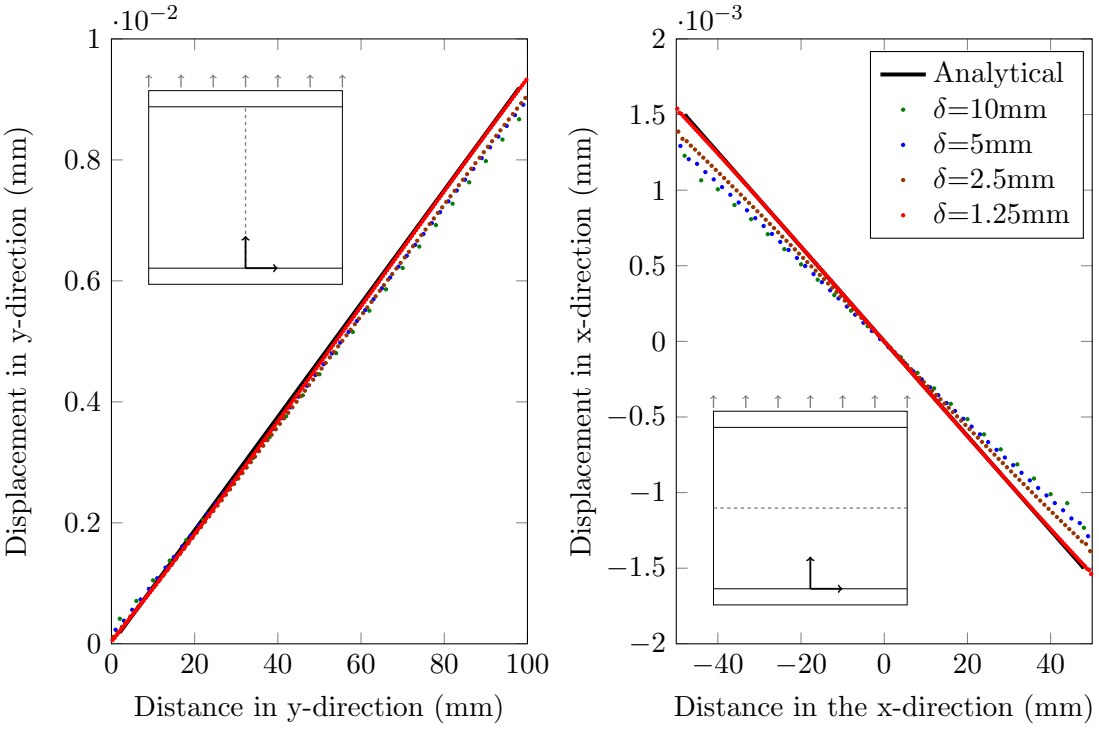

FIGURE 5.6: δ convergence of displacement solution in y and x-direction, where $m = 5$ is fixed.

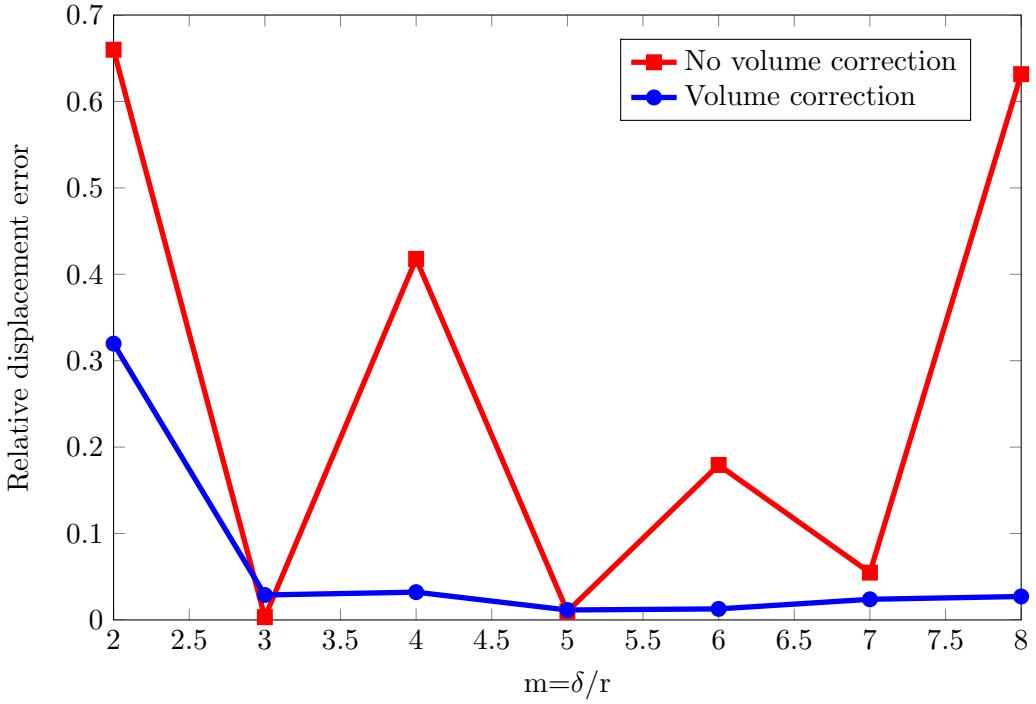

FIGURE 5.7: Convergence of relative displacement error as a function of m.

5.2.3 Non-uniform refinement

When modelling problems where stress concentrations exist in large geometries, it is inevitable that non-uniform refinement will have to be used. In this section, the square plate will have a refined patch of 50 by 50 mm situated at the centre of the plate, in order to show if any inaccuracies occur due to non-uniform refinement. The refinement of the patch will be so that Δ is equal to half of that of the rest of the plate. The zone of interest in this test will be the transition zone from the unrefined to refined region. Figure 5.8 shows the displacement solution of a uniform and non-uniform refined discretization, where it can be observed that when the material point spacing refines, the solution is more accurate and that no significant effects are present as a result of the transition zone.

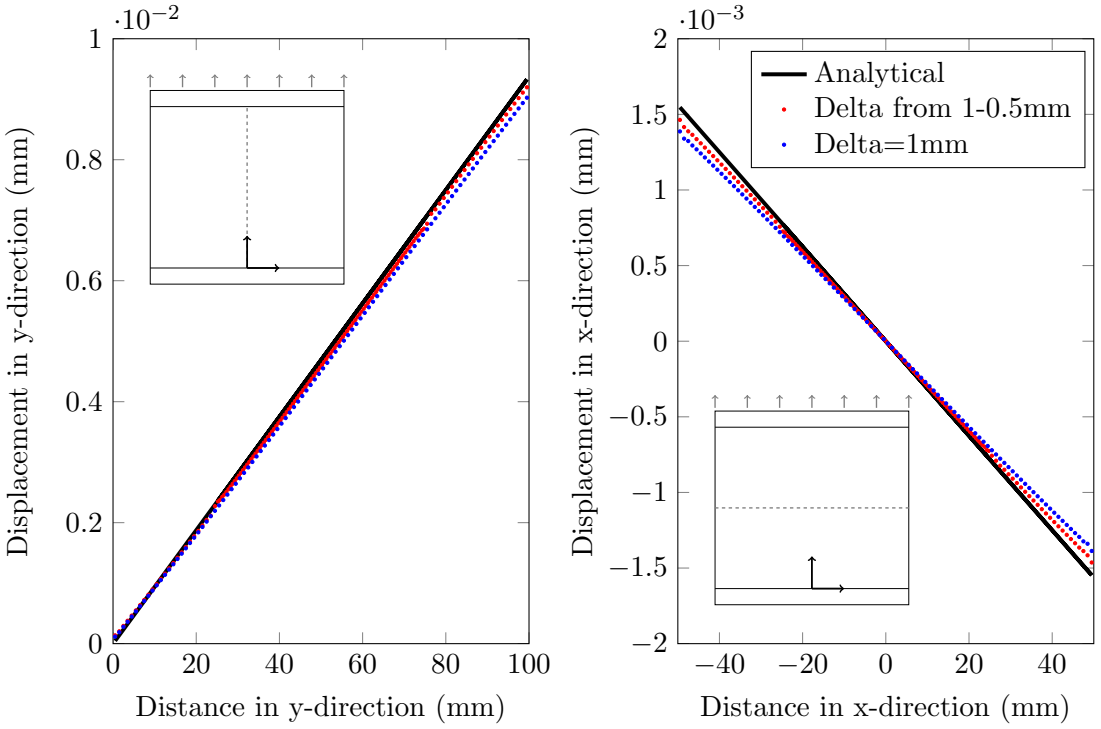

FIGURE 5.8: Displacement in x and y-direction for plate with non-uniform refinement.

5.2.4 Effect of Poisson ratio

By considering different Poisson ratios, a good indication of the ability of the numerical model to capture the constitutive properties of the material can be attained. In this section, the square plate problem will be solved for a range of Poisson ratios with a constant modulus of elasticity. The maximum displacement values from the peridynamic model will be verified by displacement values obtained from the analytical 2D plane strain solution. Test parameters are kept as in Table 5.2 with $m = 5$ and $\Delta = 1.6$mm.

The set of material properties can be obtained in Table 5.3 and the resulting displacement values in the x and y-direction can be obtained in Figure 5.9, where it can be observed that some inaccuracy occurs in the y-displacement values when $\nu > 0.35$.

TABLE 5.3: Material properties for varying Poisson ratio.

$E = 100$ GPa		
ν	K(GPa)	μ(GPa)
0.05	37.037	47.619
0.10	41.667	45.455
0.15	47.619	43.478
0.20	55.556	41.667
0.25	66.667	40.000
0.30	83.333	38.462
0.35	111.111	37.037
0.40	166.667	35.714
0.45	333.333	34.483

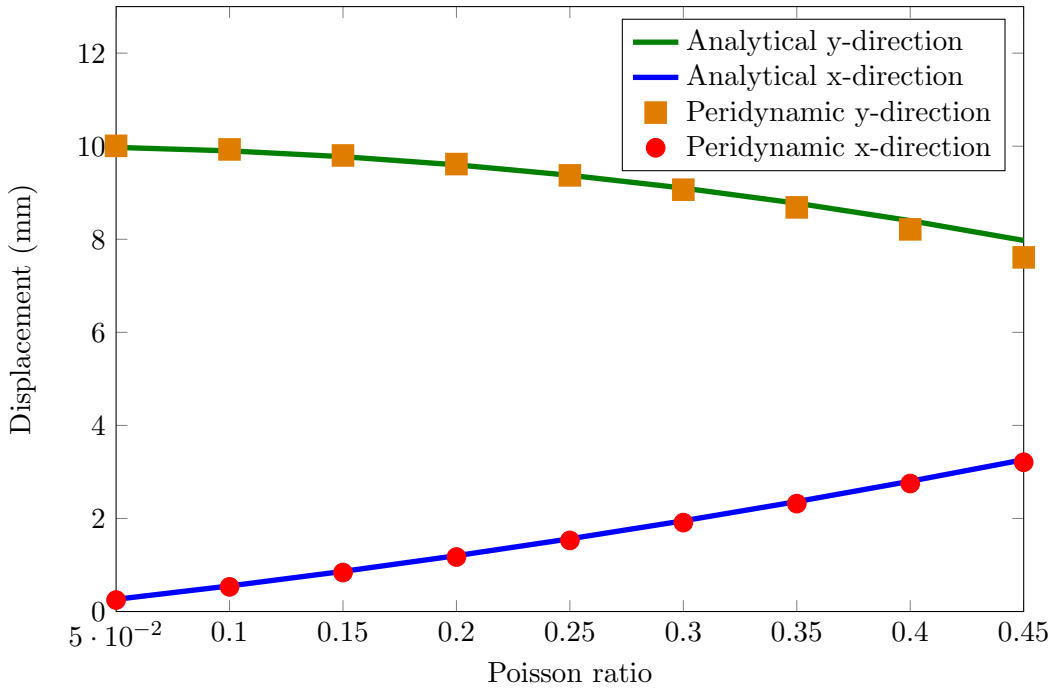

FIGURE 5.9: Maximum analytic and peridynamic displacement vs. Poisson ratio.

5.2.5 Effect of different cell shapes

Modelling of fracture propagation requires some type of perturbation or irregular discretization in order to break symmetry. Especially when fractures propagate according to the meshing scheme, special cell shapes like Delaunay triangles can be used to completely randomise the discretization and ensure random fracture propagation as discussed in Chapter 4. For this test, the material region ($\mathcal{R}$) is discretized into Delaunay triangles

with an average $\Delta = 1.6$mm and the load and constraint regions ($\mathcal{R}_l$ and $\mathcal{R}_c$) are kept to quadrilaterals with $\Delta = 1.6$mm and $m = 5$ for all regions (see Figure 5.3). In order to compare the effect of triangular cell shapes with quadrilateral cell shapes, another simulation is completed, where $\mathcal{R}$ is discretized exactly the same as $\mathcal{R}_l$ and $\mathcal{R}_c$. The displacement solution for both quadrilateral and Delaunay triangulation can be obtained in Figure 5.10.

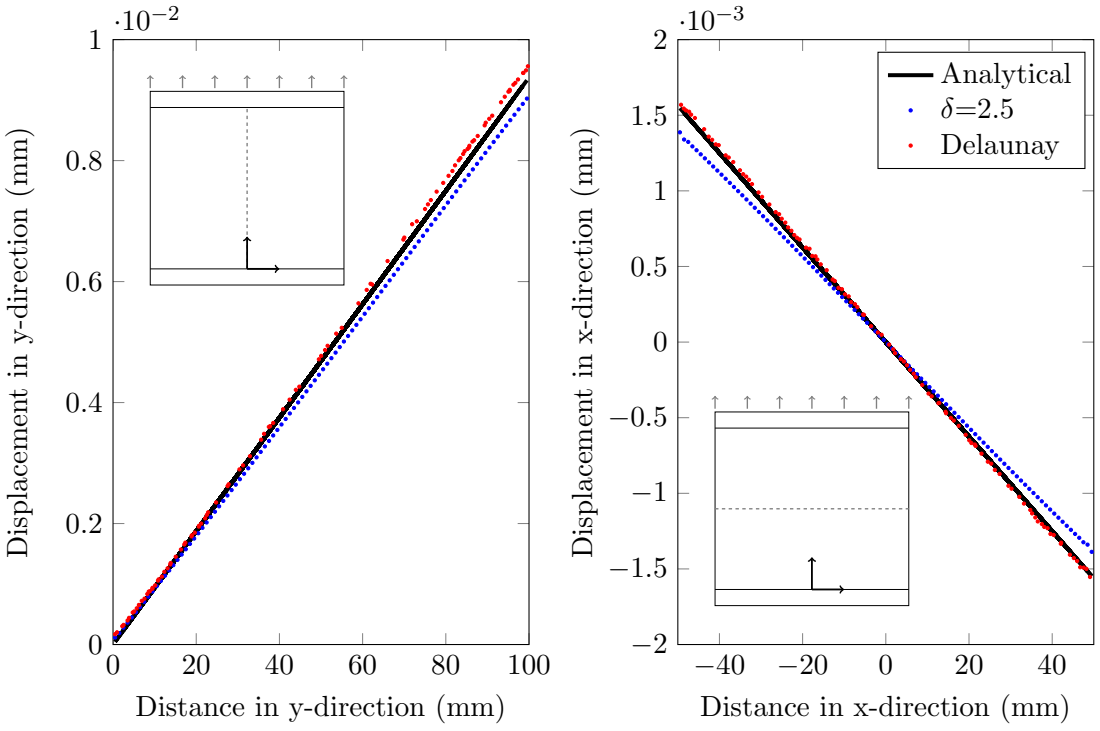

FIGURE 5.10: Displacement in x and y-direction for plates with quadrilateral and random triangular cell shapes.

Chapter 6

Implementation on Hydraulic Sleeved Fracture Model

This Chapter will contain the displacement solution, as well as, the fracture initiation and propagation solutions obtained by implementing the peridynamic formulation on the hydraulic sleeved fracture model. The displacement solution will be implemented on a thick walled cylinder with the same dimensions as the sleeved hydraulic fracture model. All results that are displayed in this Chapter will be discussed in detail in Chapter 7.

6.1 Thick walled cylinder test

The purpose of the thick walled cylinder test is ultimately to clarify whether the displacement solution, which governs the peridynamic damage model, is accurate enough to ensure that the damage model is not negatively affected by unrelated issues. Various methods for loading the cylinder with a pressure field as discussed in Chapter 4 were tested. This section will expand on the findings and how these findings will ultimately be implemented to ensure the most accurate displacement data, when verifying the damage model with the Rummel & Winter model. Since the aim of this research is to find a damage model that can be governed by the same equation that holds the constitutive relationship for the material. Results obtained from the block test will also be implemented in this section.

6.1.1 Test properties

A thick walled cylinder will be used in the following test, where the dimensions are directly based on a standard core sample of unit thickness, as will be used when verifying fracture initiation with the Rummel & Winter hydraulic fracturing model. Three different load application schemes as described in chapter 4 will be tested and analysed. Results for these methods will be presented in separate sections.

For this test, only the radial displacement u_r is required, to verify if the correct displacement can be obtained by using a certain load application scheme. Figure 6.1 shows a schematic for the classic thick walled cylinder problem that will be used for the analytical solution. Moreover, (6.1)-(6.4) represents the solutions for analytic stress and displacement functions σ_r, σ_θ and u_r that will be used in load application and displacement verification. It should be noted that the thickness of this specific representation is not to scale, due to graphical purposes. The peridynamic model for this test is based on the model from Figure 4.1 in Chapter 4, except, the initial crack will be ignored in order to find the continuous displacement field. In this initial test, the peridynamic model will only be subjected to internal pressure p_i. The material and geometric properties for the thick walled cylinder can be obtained in Table 6.1.

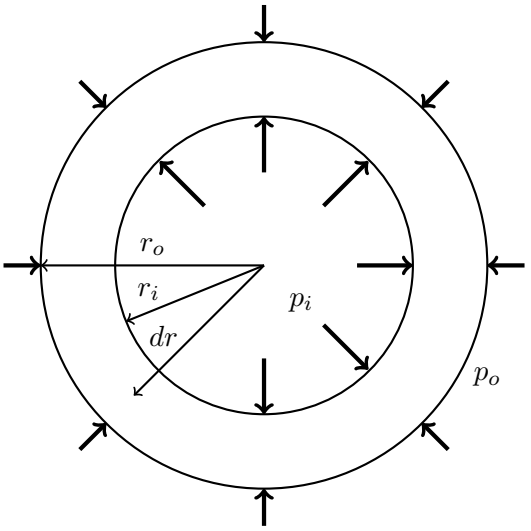

FIGURE 6.1: Thick walled cylinder with internal and external pressure p_i and p_o.

$$\sigma_r = \frac{r_i^2 - r_o^2 p_o}{r_o^2 - r_i^2} + \frac{r_i^2 r_o^2 (p_o - p_i)}{dr^2 (r_o^2 - r_i^2)} \tag{6.1}$$

$$\sigma_\theta = \frac{r_i^2 - r_o^2 p_o}{r_o^2 - r_i^2} - \frac{r_i^2 r_o^2 (p_o - p_i)}{dr^2 (r_o^2 - r_i^2)} \tag{6.2}$$

$$\epsilon_r = \frac{1}{E}(\sigma_r - \nu\sigma_\theta) \tag{6.3}$$

$$u_r = \frac{1-\nu}{E}\frac{(r_i^2 p_i - r_o^2 p_o)dr}{r_o^2 - r_i^2} + \frac{1+\nu}{E}\frac{(p_i - p_o)r_i^2 r_o^2}{(r_o^2 - r_i^2)dr} \tag{6.4}$$

TABLE 6.1: Test properties for thick walled cylinder.

Parameter	Value	
r_i	2	mm
r_o	30	mm
E	100	GPa
ν	0.25	
K	66.667	GPa
μ	40	GPa
p_i	10	MPa
p_o	0	MPa

6.1.2 Pressure through boundary region

When applying a surface pressure normal to the inner wall of the thick walled cylinder, through the body force region $\mathcal{R}_l$, it should be noted that this body force region will also contribute to the stiffness of the thick walled cylinder. This extra stiffness should be accounted for when using an external body force region. One-way of achieving this is to initially only consider the body force region $\mathcal{R}_l$ and apply an increasing prescribed displacement over this region. The internal force density can then be obtained as a function of displacement. When this function is known, it can simply be added to the initial body force region when simulating the thick walled cylinder problem. Figure 6.2 illustrates the displacements obtained, when the extra stiffness of the body force region was accounted for.

6.1.3 Body force field through entire region

By loading the cylinder region $\mathcal{R}$ with a body force, the loading region $\mathcal{R}_l$ can be omitted in this section. This procedure is essentially an energy minimising method that eliminates uncertainties due to the loading region. As discussed in Chapter 4, a body force field will be applied according to the analytic stress field solution. Results for the case of non-uniform refinement and the case of a constant horizon are shown in Figure 6.3.

6.1.4 Internal force stencil through entire region

When considering a non-local theory, like peridynamics, the discretization of a continuous solid will always induce some numerical error in the order of δ^2, when accounting for

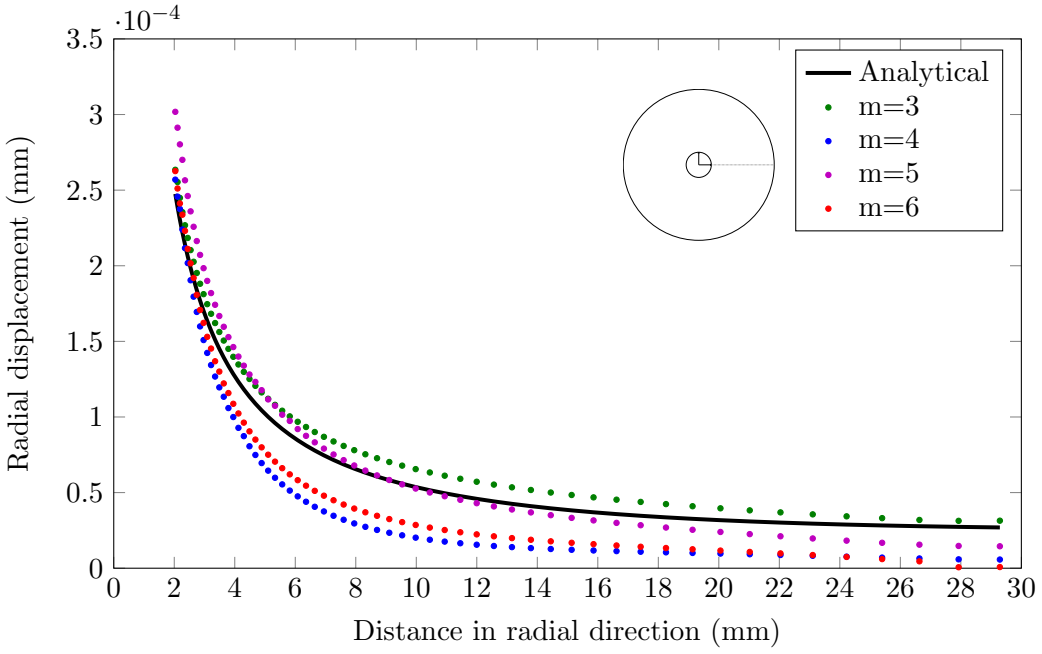

FIGURE 6.2: Radial displacements for thick walled cylinder when accounting for body force region ($\mathcal{R}_l$) stiffness.

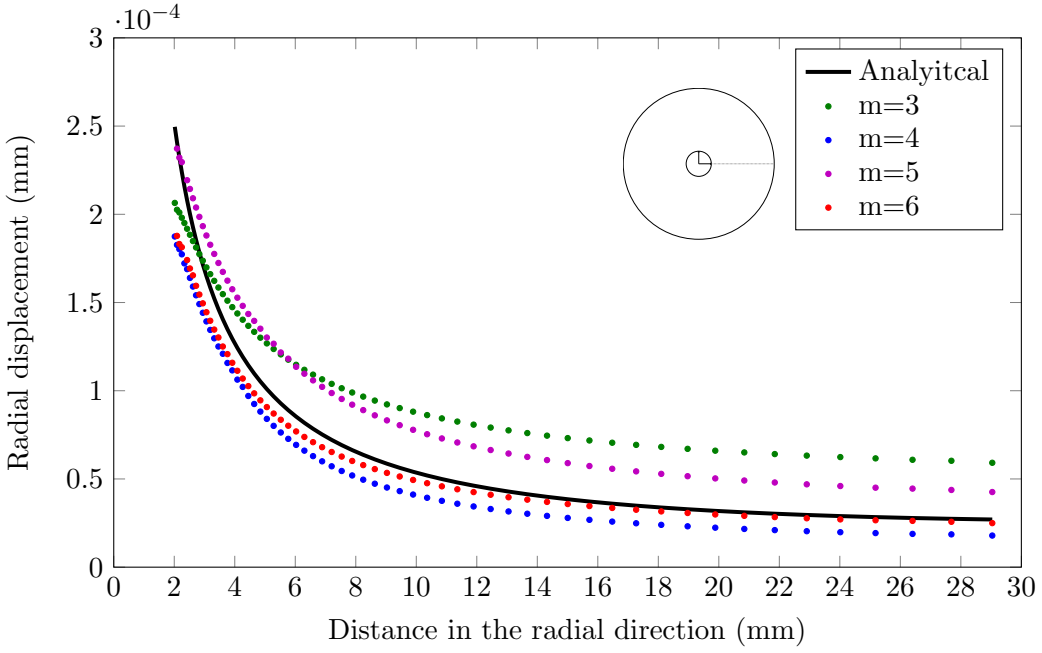

FIGURE 6.3: Radial displacements from body force density field for different m values vs. analytic displacement.

the fact that finite material volumes and interaction distances are implemented. In comparison to classic solid mechanics methods, like the FEM, where the solid is considered continuous, this can be largely minimized. Although accurate displacement solutions were obtained from the peridynamic approach, the idea is to eliminate the displacement error associated with the discretization of the solid, as well as, the non-locality of the

solution and to keep the damage prediction capabilities. In order to achieve this, the internal force stencil method was utilized, where the applied body force field is constantly updated with an analytic (or FEM in future work) solution, to rectify any displacement error. This process was discussed in Chapter 3. For a irregularly discretized geometry as shown in Figure 6.4(a), the force density error stencil ($\mathbf{f}_e$) is illustrated in Figure 6.4(b). Since the applied body force function is updated by the analytic field, the radial displacement solution for the peridynamic model will be exactly the same as for the analytic solution (see Figure 6.5).

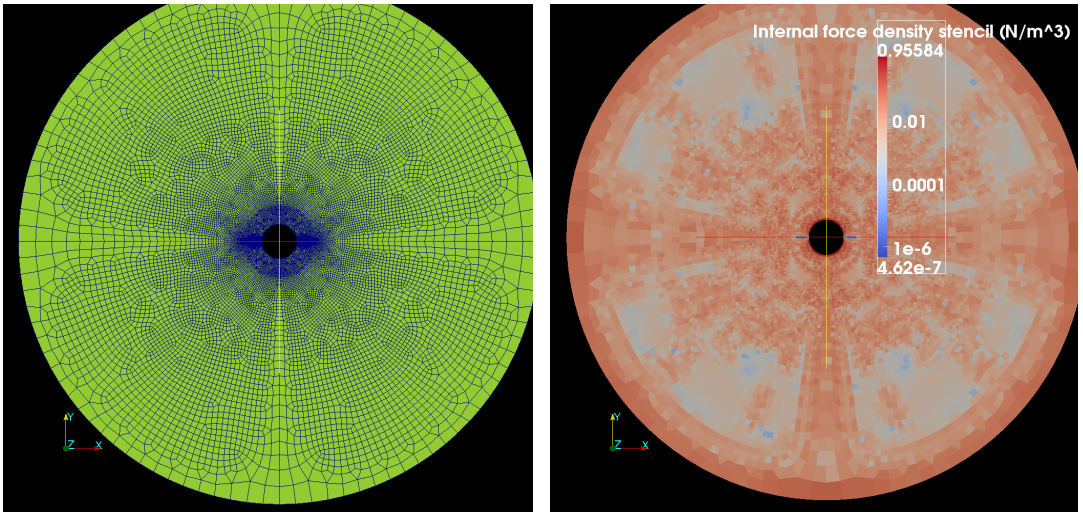

FIGURE 6.4: (a)Irregularly discretized thick walled cylinder, with (b) the respective internal force density error stencil.

6.2 Damage modelling

The final and main aim of this research is to investigate the applicability of the peridynamic damage model, to predict sleeved hydraulic fracture. This section will present the results obtained from the peridynamic approach. Firstly, the analytic model parameters will be described with an analytic solution to the problem and other factors that can have an influence on the solution. Then the implementation of the peridynamic model and the parameters used will be described. Lastly, the results for fracture initiation compared to the Rummel & Winter model and fracture propagation compared to laboratory tests will be presented.

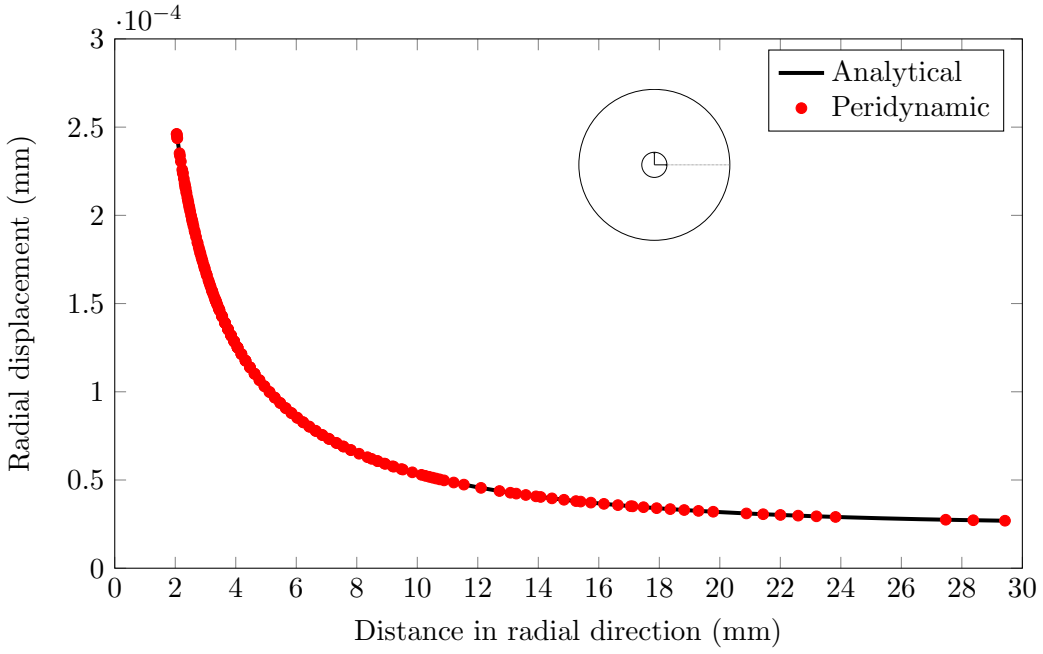

FIGURE 6.5: Radial displacements for thick walled cylinder with internal body force stencil loading.

6.2.1 Simplified Rummel & Winter solution

The Rummel & Winter hydraulic fracturing model is developed to predict breaking pressure, by assuming a borehole in an infinite plate. As a result of this assumption, some alterations are needed in order to establish whether it would be the correct analytical tool for the verification process. To establish this, it has to be indicated that the stress intensity fields in the vicinity of the crack tip of a thick walled cylinder are equal to that of an infinite plate. Brenne et al. (2013) illustrated this by obtaining a stress intensity value for both of the above instances by means of FEA. The difference in stress intensity fields can be obtained in Figure 6.6 and according to the results obtained, the stress intensity fields for sleeved fracture (SMF) in the thick walled cylinder are very similar to those of an infinite plate, given that $a < (r_o - r_i)/10$. However, for un-sleeved fracture (MF), this is not the case, as the difference in stress intensity around the tip is evident, even from small values of a and increases rapidly as a increase.

Figure 6.7 illustrates the solution for the Rummel & Winter hydraulic fracturing model for sleeved fracturing. From this solution, it is evident that breaking pressure (p_b) increases as a increases for sleeved fracture. This will lead to fracture arrest, or stable fracture propagation in the sleeved model, which will be discussed under fracture propagation. The focus for fracture initiation will lie in the zone where a is very small and where p_b undertakes an exponential increase. The peridynamic model should be able

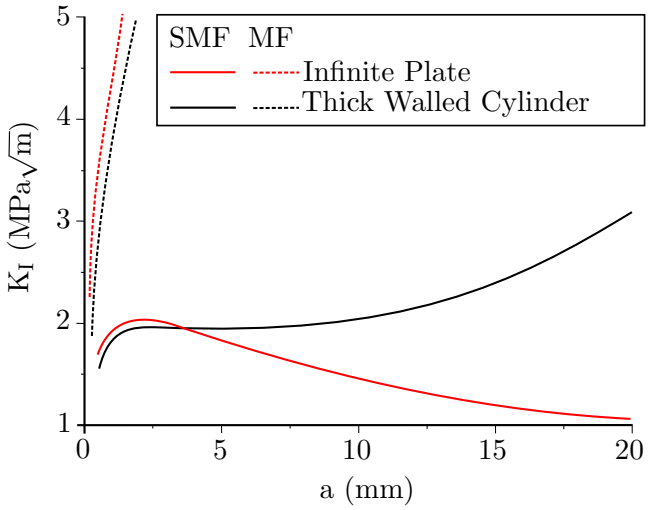

FIGURE 6.6: Stress intensity fields for an infinite plate and a hollow cylinder as a function of initial crack length (Brenne et al., 2013).

to capture this behaviour near the borehole and this will be verified under the fracture initiation section.

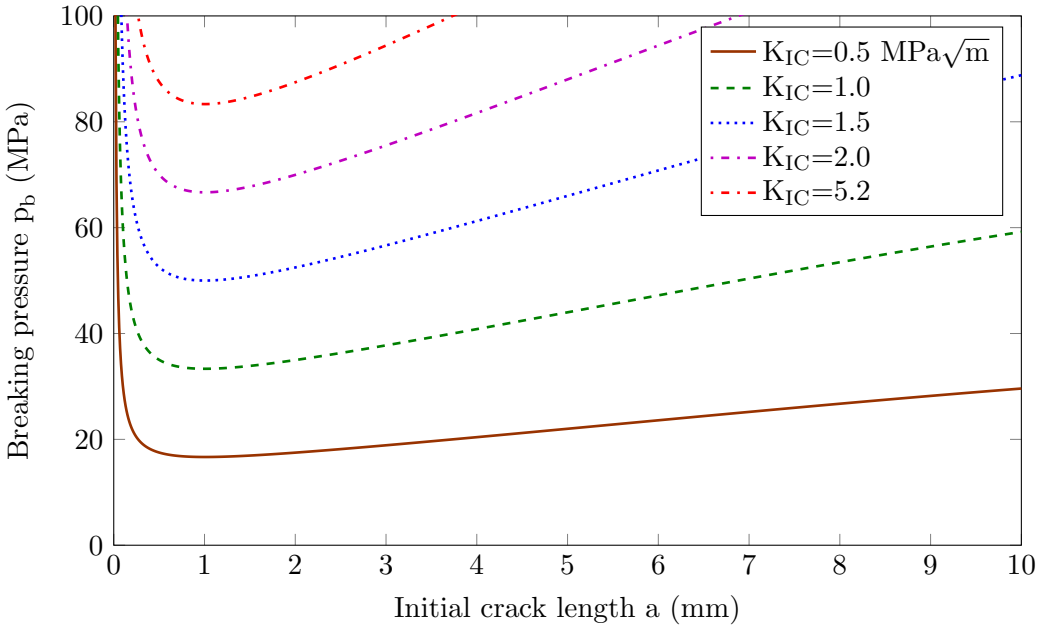

FIGURE 6.7: Breaking pressure values as a function of initial crack length according to the Rummel & Winter hydraulic fracture model.

6.2.2 Peridynamic solution

For the peridynamic solution, the model from Figure 4.1 in Chapter 4 was used with the internal force stencil loading approach. Although the error on the analytic solution for other loading approaches was not sufficient, the goal for crack initiation was to test only the damage model. When a is very small, the solution provided by the internal

force stencil approach is very accurate. In order to capture the exponential breaking pressure when a tends to zero, the refinement near the borehole had to be the same as the average grain size (D) for the material to give a good resolution. In this case the grid spacing (Δ) was selected so that the average grain size would fall between the cell size and neighbourhood size as illustrated in Figure 6.8. The horizon was taken as a function of the cell radius, since of extensive non-uniform refinement near the fracture tip region.

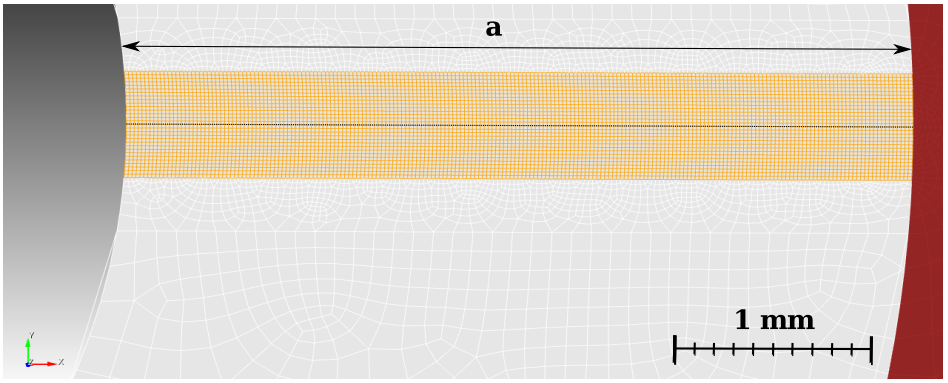

FIGURE 6.8: Near borehole refinement of discretization.

Material and geometric properties for the peridynamic solution are shown in Table 6.2. It should be noted that a stretch factor f_s was implemented in order to calibrate the peridynamic values to the corrected critical stretch s_{cc} value where:

$$s_{cc} = f_s s_c. \tag{6.5}$$

TABLE 6.2: Test properties for fracture initiation.

Parameter	Value	
r_i	2	mm
r_o	30	mm
Δ	0.02	mm
δ	4R	mm
D	0.05	mm
E	100	GPa
ν	0.25	
K	66.667	GPa
μ	40	GPa
K_{IC}	1	MPa$\sqrt{\text{m}}$
s_{cc}	9.5x10^{-6}	mm
p_i	1	MPa/s
p_o	0	MPa

6.2.3 Fracture initiation

When verifying the peridynamic model with the Rummel & Winter hydraulic fracturing model, the region close to the borehole where a tends to zero is of most interest, as this region presents the crack tip behaviour which is unique to cylindrical specimens with sleeved fracture. The results obtained for the breaking pressure according to the Rummel & Winter model and the peridynamic approximation can be obtained in Figure 6.9. Seeing that a has a limiting value (a-limit), where the simplified Rummel & Winter solution is not valid, due to the difference between a thick walled cylinder and an infinite plate. For a specimen where $r_o = 30$mm and $r_i = 2$mm, the limiting value for a is 2.8mm.

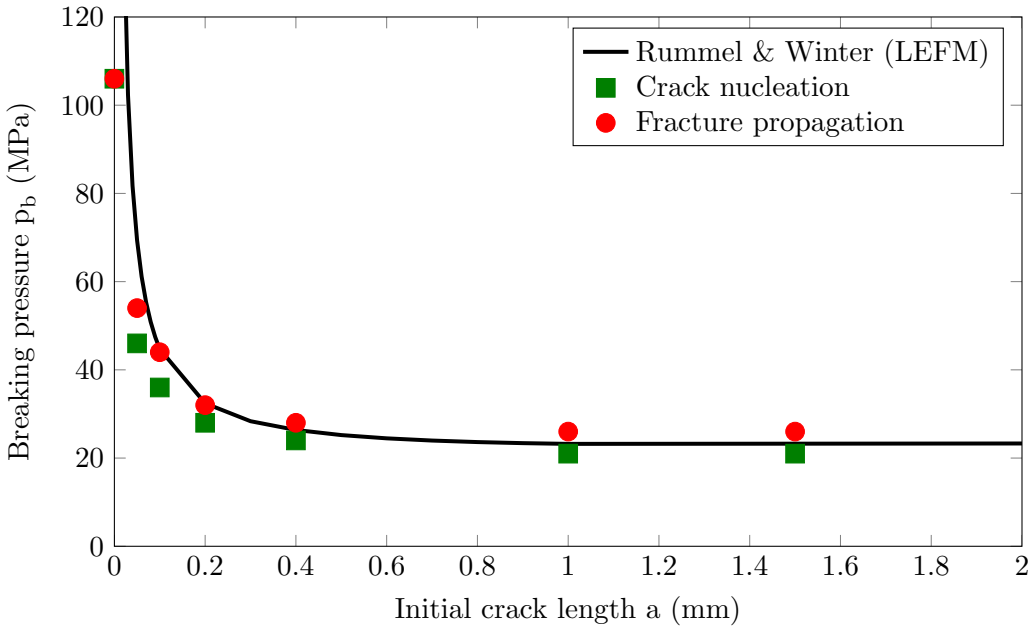

FIGURE 6.9: Breaking pressure as a function of initial crack length according to the Rummel & Winter model and the peridynamic approximation.

The breaking pressures obtained from the peridynamic model are given in *crack nucleation* or *fracture propagation* values and this is mainly the difference between damage in the form of one or two bonds breaking as a result of stress concentration and an aperture forming, which clearly defines a plane that separates material interactions.

From Figure 6.9, it is clear that the peridynamic solution for fracture initiation indeed captures the exponential breaking pressure increase when the crack length a tends to zero. This is quite significant in verifying the peridynamic damage prediction capabilities as no form of fracture criteria, except for the corrected critical stretch s_{cc}, is introduced in the peridynamic framework and regardless of this, the correlation with the analytic LEFM model is quite accurate. Another observation that should be noted is that the peridynamic breaking pressure value for a initial crack length of zero has a finite value

of 106 MPa, where the Rummel & Winter approach suggests a infinitely large breaking pressure value.

6.2.4 Fracture propagation

When considering fracture propagation, the zone of interest changes to the whole damage region $\mathcal{R}_d$. The horizon will again be a function of the cell radius. Since very large displacements occur through crack opening, the internal force stencil load application method will only be valid if the applied body force field is generated by a constantly evolving source, such as a FEM model. Another aspect that should be noted, is the amount of damage sustained for an implicit quasi-static model, where the fictitious time steps were kept in the order of tens of milliseconds. Figure 6.11 illustrates three different stages in a peridynamic sleeved hydraulic fracture simulation on a marble specimen. The first stage is at the onset of fracture initiation, followed by the second stage where the final fracture arrest has taken place and then the final stage where the specimen fails.

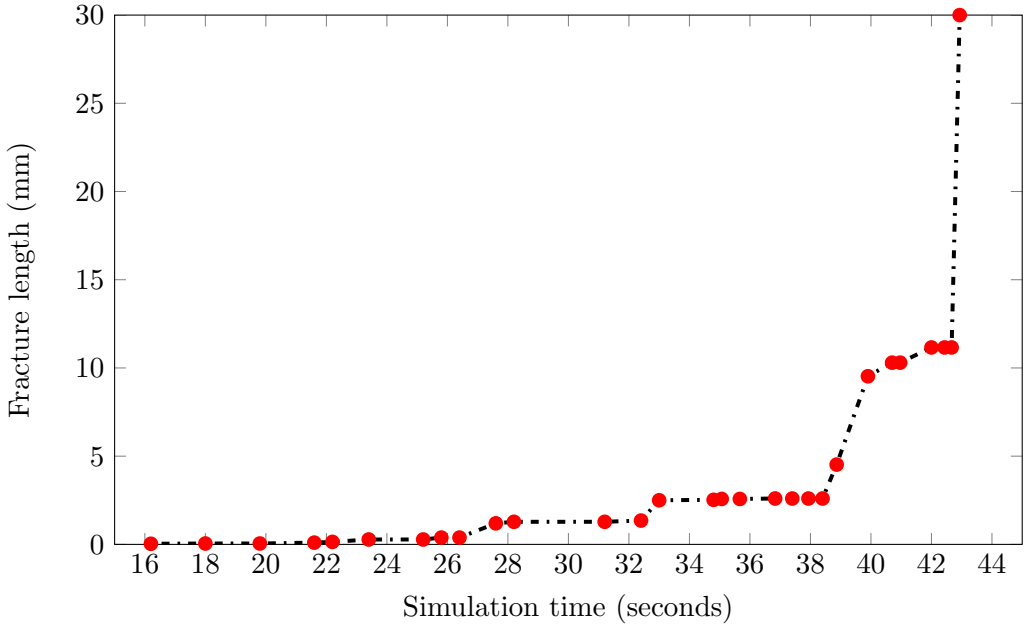

FIGURE 6.10: Peridynamic solution for stable fracture propagation rate.

In Figure 6.10, the sudden jump in crack length at a simulation time of 43 seconds is clearly illustrated. Verification of fracture propagation is however challenging in the sense that no analytical model has the capabilities to predict fracture length increase from an applied pressure. Validation through laboratory experiments would be a better measure of the behaviour expected from stable brittle fracture. Experimental and numerical results obtained from Asadi et al. (2013), indicate that stable fracture is normally encountered until the fracture length (a) is a third of the specimen radius. From

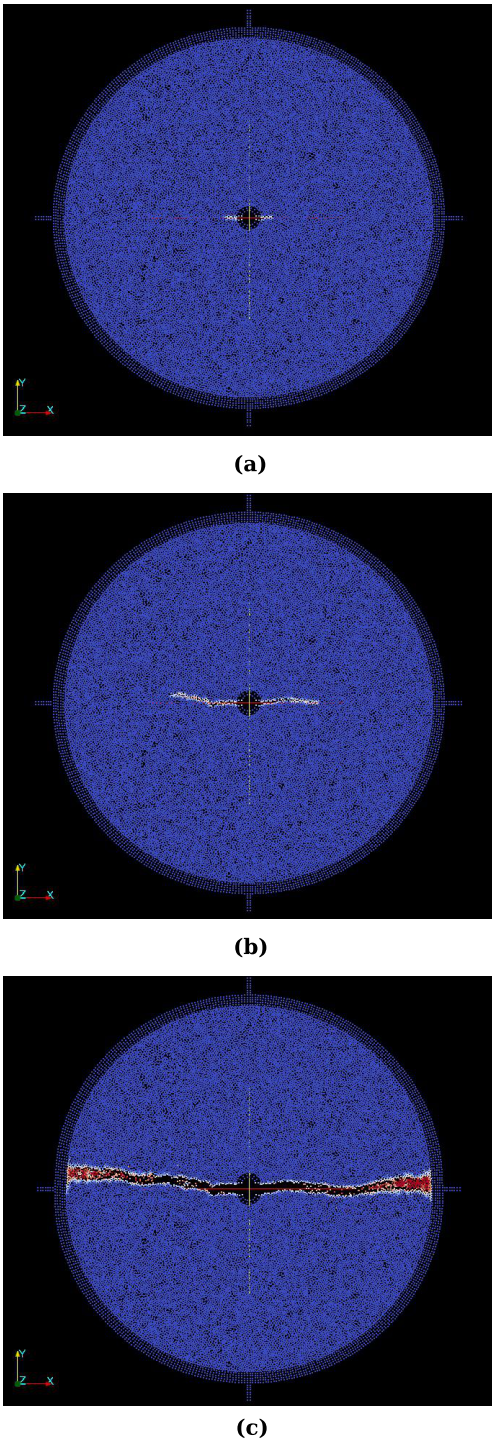

FIGURE 6.11: (a) Fracture initiation. (b) Final fracture arrest before unstable fracture. (c) Ultimate failure of the specimen.

Figure 6.10, it is clear that unstable fracture propagation starts, the moment when the fracture length exceeds a third of the specimen diameter.

Chapter 7

Discussion

7.1 Convergence to the classic solution

When studying the literature on peridynamics, it is evident that the ability to unify damage prediction with constitutive behaviour for a material under the same governing equation is a great advantage in comparison to other methods where damage is implemented as an extension to the governing equation. It should however always be clear that the peridynamic theory is non-local and this can pose many challenges in the ability to produce the classical constitutive relationship for an ordinary material. This can be a great hurdle for the analyst, when unknown to the world of non-local mechanics. When seen in contrast to local mechanics, where only the material properties are a variable in characterising material behaviour, non-local mechanics is significantly more complex, when considering that the discretization and horizon size can also change how a certain material behaves. In this section, the types of convergence to the classical solution will be discussed based on findings through the course of this research.

7.1.1 Convergence with fixed horizon size (m-convergence)

It was suggested from test results, regarding m-convergence rates, that the peridynamic solution does indeed converge to the classical solution when volume correction is not accounted for. For dilatational purposes, even a m value as low as 3, gave a close approximation to the classical solution. However, it was also evident when deviatoric behaviour was taken in account, the solution only really started converging from $m \geq 5$ for the square plate. This shows that the optimum value should be $m = 5$, when using the volume correction algorithm as described in this thesis. When implementing the volume correction method, very accurate solutions were obtained when $m > 5$. The

volume correction method was found to be a major factor in making the peridynamic model more robust in terms of selecting the neighbourhood size and the number of material points contained in a neighbourhood. Comparison of m-convergence results, from solutions that implemented the volume correction algorithm and solutions that did not implement the volume correction, showed that much better convergence was obtained for lower m values, where volume correction was used. This indicates the importance of more accurate numerical integration over the material horizon.

7.1.2 Convergence with fixed m ratio (δ-convergence)

From the results obtained, it was demonstrated that δ-convergence is useful when accurate solutions are needed. When considering the effect of m-convergence and δ-convergence on the amount of processing power required to obtain a solution, it is clear from Chapter 4, that refinement in the case where the number of interactions for each material stays constant (δ-convergence), is much less process intensive than when the number of interactions grows with each refinement step. This illustrates how important it is to get m-convergence accurate at a low value, in order to make full use of the low processing demand when using δ-convergence. Overall, the displacement solution constantly converged to a reasonable approximation of the analytic solution and it was observed that δ-convergence is a more stable approach to converge to the analytic solution, which makes sense, since the neighbourhood level stays constant in δ-convergence.

When inspecting the difference between m and δ-convergence, it was also noted that the rate of convergence for m-convergence is much faster than for δ-convergence and when m is not chosen to best represent the classical solution, that δ would never converge to the classical solution. This indicates the importance of choosing the correct m value for a specific problem.

7.2 Spatial discretization and mesh dependency

Since the peridynamic formulation is integral based, it requires numerical integration over a certain region, like the peridynamic horizon ($\mathcal{H}$), which can introduce numerical integration errors, when this region is irregular. These irregularities in the horizon can be an attribute of non-uniform refinement, or when material points are discretized in a random fashion, such as Delaunay triangulation. When considering coarse discretizations, the numerical error can become sufficiently large and to account for this, various techniques, like volume correction and stiffness correction can be implemented to smooth out the numerical error associated with irregularities. This section will discuss

two sources of irregularities that have been encountered in this research and how the implementation of correction methods has improved the solution.

7.2.1 Non-uniform refinement

Non-uniform refinement is essential when dealing with large complex geometries, especially radial geometries. The application of non-uniform refinement can either be in a smooth fashion, where the spacing between material points gradually decreases, or in an abrupt fashion where a transition zone divides the coarse discretization from the finer discretization. The transition zone is of importance, since this is the zone where irregularities occur, such as material points that does not have mutual interaction (see Figure 4.3) and neighbourhoods that have more interactions than the average in the system. When no correction methods were applied, it was found that the refinement had to be applied as smooth as possible, in order to keep the horizon level (see Section 4.5.1.) constant. Otherwise, there would be large residuals on the interaction zones, which causes jumps in the displacement.

The first method that was applied in order to correct the stiffness contribution of the material point is the same as in Section 4.4.2, where it is treated as a surface effect and the second is the volume correction method as in Section 4.4.3. Good results were obtained from these methods, when tested on non-uniform refinement with an abrupt transition zone, where material point spacing was halved. Instead of showing jumps on the transition zone, the displacement solution obtained increasing convergence to the analytical solution. When compared with a solution with only uniform refinement, the non-uniform refinement showed a closer resemblance to the analytic solution. This indicates that the correct implementation of uniform refinement will not only give a more accurate solution in the refined region, but also improves the global solution.

7.2.2 Different cell shapes

When fracture propagation is considered, often the fracture path can be influenced by a structured discretization and this can be avoided by using a random discretization technique, such as Delaunay triangulation. Another advantage of using randomised discretizations, is the fact that a good element shape quality can be obtained for literally any level of complexity. In some cases, where structured discretizations were used in complex geometries, the warping of the discretization had detrimental effects on the displacement solution. Tests done on random Delaunay discretizations did however indicate that a large numerical integration error could be encountered when not using volume correction functions. Due to each cell having a slightly different size, the horizon

boundary can become largely irregular, giving a faulty representation of the cylindrical horizon.

By using the volume correction method, the irregular boundary is smoothed and a better approximation of the cylindrical shape for the horizon can be obtained. The block test on the random triangular discretization showed a very accurate approximation to the analytical result and when used in fracture propagation, a random fracture was obtained.

7.3 Alternative loading techniques

The nature of radial pressure loading of a borehole has proven to be a challenging aspect of the peridynamic sleeved hydraulic fracture model. No literature has yet been published to the authors knowledge on the subject of radial pressure loading for a quasi-static implicit peridynamic model. Because of this, various approaches to radial loading in the form of analytical force density fields and internal force stencils by using error estimation were developed and implemented.

7.3.1 Body force through entire domain

When applying a body force through the entire domain, it was found that the error was mainly introduced through the loading function. Radial pressure loading with a body force, suffer from the effect of varying cell size and shape quality. From the results obtained, by introducing pressure loading with a body force, it is evident that the effects of irregularities prove to be detrimental to the accuracy of the solution. Thus, it is clear that the load application technique has to be developed further. The technique applied in this research, is not sufficient to apply in damage verification.

7.3.2 Internal force stencil through entire domain

Due to the inaccuracy of the results obtained from models that implemented body force loading, it was decided to employ a technique where the load contains the error stencil. As a result, this will eliminate most problem aspects of the non-local theory, such as integration error. The displacement result obtained from this method was, as expected, equal to the exact analytic solution. This method has the inherent disadvantage, that the internal force field from an analytic or other numerical method, like the FEM, is needed in order to accurately implement the damage model. However, it can be used as an effective coupling method, when running in parallel with FEM software. In this way, the accuracy of the FEM software can be combined with the peridynamic ability

to naturally predict fracture propagation. Since, the verification of the damage model is the main objective in this research, it was decided to implement the internal force stencil method, to acquire the most accurate displacement result possible.

7.4 Damage modelling

The ultimate aim of the peridynamic model is to accurately represent sleeved hydraulic fracture propagation. Since most of the work in this research is based on finding an accurate displacement solution and characterizing robustness issues associated with implementing the peridynamic theory, the following section will focus on the more advantageous aspects of the peridynamic theory. Damage modelling is inherently what the peridynamic theory was designed to excel in. Although accurate displacement solutions can be troublesome to obtain, the peridynamic damage model has a very simplified approach and can be seen as a natural extension of the theory. Fracture initiation is the main verification tool, due to the inability of analytic models to accurately capture fracture propagation and because of this, the fracture propagation results will be compared to experimental tests.

7.4.1 Fracture initiation

Verification of the fracture initiation model was done by comparing the resulting breaking pressures, as a function of initial crack size, to those obtained when using the Rummel & Winter hydraulic fracture model. The results that were obtained illustrate that the peridynamic damage model does indeed capture the exponential increase of breaking pressure as the initial crack length approaches zero. Apart from this, it can also be observed that some error exists when a goes to zero. Since the Rummel & Winter hydraulic fracture model is formulated on the basis of LEFM, the breaking pressure will increase to infinity when a approaches zero. This is a non-physical phenomenon, since no material can withstand infinite stress. When considering the crack tip, the peridynamic theory predicts a cusp-like crack tip, where the LEFM approach predicts a parabolic crack tip. As a result of this, the peridynamic theory has a more realistic approach to the crack tip, thus the difference observed in breaking pressure can well be an artefact of a non-physical stress representation captured by LEFM when then a tends to zero.

7.4.2 Fracture propagation

Fracture propagation prediction can be challenging when considering an implicit quasi-static peridynamic model. The reason behind an implicit model is the interest in the length and direction of the propagated fracture, when a specific amount of energy is allocated to the system. In this sense, none of the dynamics of fracture propagation is captured, for instance, propagation speed or wave dispersion through the solid. Although these dynamic effects are not captured in an implicit quasi-static model, it is still advantageous in the sense that it is not bound to all the attributes that accompanies the dynamic solution, for instance minute time steps and slow convergence rates. Since the implicit solution is obtained through complex solvers, which are sensitive to non-symmetric stiffness matrices and overly relaxed boundary conditions, maintaining numerical convergence proves to be challenging when considering large amounts of damage. Methods, which are described in Section 4.3.2, were used to ensure stability of the stiffness matrix. Although some penalty in the form of inaccurate displacement may occur from the use of these methods, the resulting solution proved to be interesting. Validation of the peridynamic model was done by comparing the point at which unstable fracture starts with experimental results. From the results obtained, it is clear that ultimate failure of the hydraulic sleeved fracture model can be captured with an implicit quasi-static peridynamic formulation. In addition to this, the point where unstable fracture started, agreed with experimental results obtained from the literature, which state that, for a standard sleeved hydraulic fracture sample, unstable fracture propagation is captured when the crack length reaches a third of the outer radius of the specimen.

Chapter 8

Conclusion

This chapter will conclude on the results obtained from the verification of the peridynamic model. Considering the displacement verification, as well as, the challenges associated with using a non-local theory to capture the constitutive material behaviour of a linear elastic material. Since the simulation of fracture initiation and propagation is the main objective in this research, the suitability of the peridynamic model for fluid induced fracture will also be discussed in context of the results that were obtained in this research. Lastly, some ideas for further research and application of the peridynamic model, in the field of fluid induced fracture, will be discussed.

8.1 Findings obtained from verification of the peridynamic model

8.1.1 Displacement solutions

Displacement verification tests were performed on three types of geometries, namely the 3D cube, the 2D plate and the thick walled cylinder. The 3D cube was only tested on an affine hexagonal discretization, with a uniform tensile stress applied in the z-direction. An accurate displacement solution was obtained for the coarsely discretized model according to the analytic solution. This indicates that the 3D peridynamic formulation is capable of capturing the constitutive behaviour of the material.

The 2D plate was tested under various conditions, ranging from m-convergence, δ-convergence, non-uniform refinement and varying cell shapes. In all of these tests, the plate was placed under a uniform tensile stress in the y-direction, with the assumption of 2D plane strain, since no strain was permitted out of plane. The peridynamic solution

converged to a reasonable approximation of the analytic solution for a m value of 5. When δ-convergence was implemented, the peridynamic solution converged to a reasonable approximation of the analytical solution. This indicates that the 2D plane strain peridynamic formulation does indeed converge to the analytical solution. Non-uniform refinement tests were conducted to analyse the effect of abrupt changes in material point interaction distance, when volumetric correction was implemented. The resulting solution verified that no displacement jumps were present at transition zones and that the global displacement solution improved when non-uniform refinement was applied. This indicates that, with the proper correction procedure, non-uniform refinement could be applied without suffering a displacement penalty at transition zones. Different cell shapes, in the form of Delaunay triangulation, were implemented to analyse the effect of varying cell sizes and material point interaction distances. This test was conducted due to the need for irregular discretizations, for complex geometries and random fracture propagation. The resulting solution verified that no excess residuals formed at larger cell clusters. This indicates that irregular discretizations can successfully be implemented when using the 2D plane strain peridynamic formulation, which is especially useful when considering complex geometries.

The thick walled cylinder was tested under three different loading conditions, namely a surface traction applied through a external pressure block, a body force distribution through the entire cylinder and an internal force stencil obtained from the analytical solution. The horizon size was taken as a function of the cell radius in all tests. Results from all loading schemes that used external residual contributions, such as body force, deviated quite largely from the analytical solution. This concluded that the usage of external force contributions would not be suitable for verification of the peridynamic damage model. In lieu of this, the internal force stencil method was applied to give zero deviation on the analytical solution.

8.1.2 Difficulties associated with non-local theories

While implementing the peridynamic formulation in 3D, as well as in 2D plane strain, some difficulties associated with the behaviour of non-local theories were encountered. These difficulties were characterised as the degree of non-locality, integration error due to surface effects, as well as, irregular discretizations and lastly, the application of a traction on a peridynamic surface. Two techniques were implemented to address the difficulties related to choosing the correct degree of non-locality and minimising integration error over incomplete or irregular horizons. These were the volume correction technique and the scaling of interaction contributions by the number of interactions

per horizon. Results obtained when implementing these techniques, revealed a great improvement in solution accuracy. This concludes that these error minimisation techniques are very effective and important when considering coarser peridynamic discretizations. A body force field was applied to the peridynamic solid in order to simulate a traction on a surface. Results obtained from using a body force field, proved to only be accurate when the body force was applied over an affine quadrilateral discretization. This concludes that a traction can be imposed on a peridynamic solid, through using a body force field and that more research is necessary in order to improve body force loading over a non-uniform discretization.

8.2 Suitability of the peridynamic model for fluid induced fracture

Fracture initiation was implemented through the usage of the internal force stencil technique and verification was done by comparing breaking pressure values with the Rummel & Winter hydraulic fracturing model. Results obtained, indicated that the peridynamic formulation did indeed capture the exponential behaviour of breaking pressure for a small initial fracture, as indicated by the analytical solution. This concludes that the peridynamic formulation can be used to accurately model fracture tip behaviour, given that an accurate displacement solution can be obtained.

Fracture propagation was implemented by the usage of a body force loading region for pressure application, since the internal force stencil technique was only deemed valid for small initial cracks, when using an analytical displacement source. Random propagation of the fracture throughout the specimen was successfully achieved by using the implicit quasi-static solution technique. Resulting fracture propagation captured the effect of boundary conditions, since unstable fracture occurred at the same fracture length obtained in experimental tests. This concludes that the implicit quasi-static peridynamic solution can be used to simulate large-scale damage and random fracture propagation. In addition, in conjunction with this, it shows that the fracture propagation regime, as steered by boundary conditions, can be captured realistically, without the need for external fracture criteria.

When considering the peridynamic formulation for fluid induced fracture propagation, it should be noted that loading will be in the form of tractions on borehole surfaces, for materials with very low permeability and body force flux, when introducing pore pressure due to fluid leak off. Both of these loading techniques will be challenging when considering the results obtained in this research, however, the peridynamic damage

model proved to be useful and accurate when considering fracture. In lieu of this, a large potential still exist to implement the peridynamic model for complex fluid induced fracture problems.

8.3 Further research

8.3.1 Dynamic pressure load application on fracture walls

When considering the concluding remarks, it is clear that an effective technique for the application of a traction on a non-uniformly discretized region is the most important subject for further research. Adding to this will be the development of a dynamic load application function on the fracture walls, which will evolve as the fracture propagates through the peridynamic solid. This will give the ability to not only model sleeved hydraulic fracture, but also un-sleeved hydraulic fracture, which is a step closer to simulation of real hydraulic fracturing operations.

8.3.2 Characterisation and implementation of fluid leak off through a pore pressure model

Fluid leak off is always a factor in hydraulic fracturing operations and implementation of a fluid leak off function can be done through modifying the peridynamic dilatational parameter, in the governing equation. Since the effect of pore pressure is directly applied in the governing equation, no coupling methods need to be implemented and this reduces the complexity of the model. A pore pressure model with the capability to accurately capture fluid leak off will greatly aid in the capabilities of the peridynamic model, to simulate real hydraulic fracturing operations and other phenomena, like pumping in pavements and dam wall fracture.

8.3.3 Coupling of peridynamics and the Finite Element Method

The capabilities of the FEM to accurately predict complex displacement solutions can be implemented in the internal force stencil approach, described in this thesis. In this way an accurate displacement field, as well as, an accurate damage model can be implemented in parallel to benefit from both methods. This would require an update on the FEM discretization for each instance in which fracture propagation occurs in the peridynamic model. In effect, this would produce more accurate results than the usage of the analytic solution in the internal force stencil method.

Appendix A

Derivation of the 2D plane strain peridynamic formulation

The following derivation will be divided into two sections, considering dilatation and deviatoric extension for the 2D ordinary state based peridynamic formulation. Expressions are taken directly from Silling et al. (2007), since the same technique is used in this derivation.

A.1 Dilatation in 2D

In Silling et al. (2007), the weighted volume, dilatation and deviatoric extension for a peridynamic horizon are all integrated over a spherical volume, whereas in 2D plane strain, the horizon resembles a disc instead of spherical volume. Thus, in the 2D derivation, these three components will be integrated over a cylindrical volume of unit thickness. From Silling et al. (2007) Eq. (105), the force scalar state for a linear peridynamic solid in 3D is given by:

$$\underline{t} = \frac{3k\theta}{q}\underline{\omega}\,\underline{x} + \alpha\underline{\omega}\,\underline{e}^{d} \tag{A.1}$$

where, k is the bulk modulus, θ the dilatation, q the weighted volume, $\underline{x}$ the reference bond length, α the shear parameter that will be derived in this Appendix, $\underline{e}^{d}$ the deviatoric extension and the influence function $\underline{\omega}$, which is a scalar state operating on a bond vector $\boldsymbol{\xi}$ and determines the shape of the horizon. In this derivation $\underline{\omega}\,\langle\boldsymbol{\xi}\rangle$ will have a unit value, since the horizon is based on a symmetrical cylindrical shape, and will only

be denoted as $\underline{\omega}$ in order to preserve neatness. In Figure A.1, a graphical representation of the extension state $\underline{e}$ as well as the dilatation (volumetric strain) $\theta \approx \Delta V/V_0$ is illustrated for a displacement of $\mathbf{u}$.

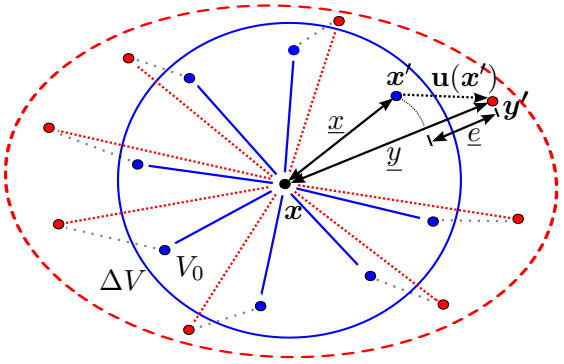

FIGURE A.1: Peridynamic extension and dilatation.

When small isotropic deformations are considered, θ can be seen as the volumetric strain. In the classical theory, the volumetric strain is based on the trace of the strain tensor $\boldsymbol{\epsilon}$:

$$\frac{\Delta V}{V_0} = Trace[\boldsymbol{\epsilon}] = \epsilon_{ii} + \epsilon_{jj} + \epsilon_{kk} \tag{A.2}$$

and when considering a hydrostatic strain $\epsilon_0 = \epsilon_{11} = \epsilon_{22} = \epsilon_{33}$:

$$Trace[\boldsymbol{\epsilon}_{3D}] = \epsilon_0 + \epsilon_0 + \epsilon_0 = 3\epsilon_0 \quad \text{and} \quad Trace[\boldsymbol{\epsilon}_{2D\,plane\,strain}] = \epsilon_0 + \epsilon_0 + 0 = 2\epsilon_0. \tag{A.3}$$

From (A.3), it follows that $\theta = 3\epsilon_0$ for 3D and $\theta = 2\epsilon_0$ for 2D, resulting in an expression for $\theta(\underline{e})$ as:

$$\theta(\underline{e})_{3D} = \frac{3}{q}(\underline{\omega}\,\underline{x}) \bullet \underline{e} \quad \text{and} \quad \theta(\underline{e})_{2D\,plane\,strain} = \frac{2}{q}(\underline{\omega}\,\underline{x}) \bullet \underline{e}. \tag{A.4}$$

To prove this, firstly the extension state $\underline{e}$ can be written in terms of the initial bond length $\underline{x}$ with a strain ϵ_0 operating on it.

$$\underline{e} = \underline{y} - \underline{x} = \underline{x}\epsilon_0 \tag{A.5}$$

Since $\theta(\underline{e})$ is a function of the weighted volume q, a new expression for q must be derived in terms of a cylinder with unit thickness.

$$
\begin{aligned}
q &= \underline{w}\,\underline{x} \bullet \underline{x} \\
&= \int_{\mathcal{H}} \underline{\omega}\,\underline{x} \bullet \underline{x}\, dV_\xi \\
&= \int_0^\delta \int_0^{2\pi} \int_0^1 \underline{\omega} r^2 r\, dz d\theta dr \\
&= \int_0^\delta 2\pi \underline{\omega} r^3\, dr
\end{aligned} \tag{A.6}
$$

Lastly, the proposed $\theta(\underline{e})$ will be evaluated over a cylinder with unit thickness and by substituting in (A.5) and (A.6), it can be shown in (A.7) that the proposed function for $\theta(\underline{e})$ is suitable for a cylinder with unit thickness. For the purpose of clarity it should be noted that $\underline{x} = |\underline{\mathbf{X}}\,\langle \boldsymbol{\xi} \rangle\,| = |\boldsymbol{\xi}|$.

$$
\begin{aligned}
\theta(\underline{e}) &= \frac{2}{q}(\underline{\omega}\,\underline{x}) \bullet \underline{e} \\
&= \frac{2}{q} \int_{\mathcal{H}} \underline{\omega}\,\underline{x}\,\underline{e}\, dV_\xi \\
&= \frac{2}{q} \int_{\mathcal{H}} \underline{\omega}\,\underline{x}\,\epsilon_0 \underline{x}\, dV_\xi \\
&= \frac{2}{q} \int_{\mathcal{H}} \underline{\omega}\,|\boldsymbol{\xi}|\,\epsilon_0 |\boldsymbol{\xi}|\, dV_\xi \\
&= \frac{2}{q} \int_0^\delta \int_0^{2\pi} \int_0^1 \underline{\omega} r \epsilon_0 r\, r\, dz d\theta dr \\
&= \frac{2}{q} \int_0^\delta \int_0^{2\pi} \int_0^1 \underline{\omega} \epsilon_0 r^3\, dz d\theta dr \\
&= \frac{2}{q} \int_0^\delta 2\pi \underline{\omega} \epsilon_0 r^3\, dr \\
&= \frac{2}{q} \epsilon_0 q \\
&= 2\epsilon_0
\end{aligned} \tag{A.7}
$$

When considering the change in the representation of $\theta(\underline{e})$, (A.1) for 2D plane strain can now be rewritten as:

$$
\underline{t} = \frac{2k'\theta}{q} \underline{\omega}\,\underline{x} + \alpha \underline{\omega}\,\underline{e}^d, \tag{A.8}
$$

where:

$$k' = k + \frac{\mu}{3}. \tag{A.9}$$

Since k represents the bulk modulus, which is exactly the same in the classical theory, the only parameter left to be defined is α, which needs to be related to the shear parameter μ from the classical theory.

A.2 Deviatoric extension in 2D

In order to find α, the strain energy density from the classical theory will be equalized with the strain energy density from the peridynamic approach. Since α is based on deviatoric extension, only strain energy density contributions from deviatoric extension will be accounted for. From Silling et al. (2007) Eq. (104), the peridynamic elastic strain energy density due to deviatoric extension is given by:

$$W(\underline{e}^d) = \frac{\alpha}{2}(\underline{\omega}\,\underline{e}^d) \bullet \underline{e}^d, \tag{A.10}$$

where the deviatoric extension corresponding to classical shear strain can be obtained from Silling et al. (2007) Eq. (107) as:

$$\underline{e}^d\langle\boldsymbol{\xi}\rangle = \frac{\epsilon^d_{ij}\xi_i\xi_j}{|\boldsymbol{\xi}|} = \frac{1}{|\boldsymbol{\xi}|}\sum_{i,j=1,2}\epsilon^d_{ij}\xi_i\xi_j \tag{A.11}$$

and the peridynamic elastic energy density over a cylinder of unit thickness can be evaluated as:

$$\begin{aligned}
W(\underline{e}^d) &= \frac{\alpha}{2}\int_{\mathcal{H}} \underline{\omega}\langle\boldsymbol{\xi}\rangle \left(\underline{e}^d\langle\boldsymbol{\xi}\rangle\right)^2 dV_\xi \\
&= \frac{\alpha}{2}\int_{\mathcal{H}} \underline{\omega}\langle\boldsymbol{\xi}\rangle \left[\frac{1}{|\boldsymbol{\xi}|}\sum_{i,j=1,2}\epsilon^d_{ij}\xi_i\xi_j\right]\left[\frac{1}{|\boldsymbol{\xi}|}\sum_{k,l=1,2}\epsilon^d_{kl}\xi_k\xi_l\right] dV_\xi \\
&= \frac{\alpha}{2}\int_{\mathcal{H}} \frac{\underline{\omega}\langle\boldsymbol{\xi}\rangle}{|\boldsymbol{\xi}|^2}\Big[(\epsilon^d_{11})^2(\xi_1)^4 + (\epsilon^d_{22})^2(\xi_2)^4 + 4(\epsilon^d_{12})^2(\xi_1)^2(\xi_2)^2 \\
&\quad + 2\epsilon^d_{11}\epsilon^d_{22}(\xi_1)^2(\xi_2)^2 + 4\epsilon^d_{11}\epsilon^d_{12}(\xi_1)^3\xi_2 + 2\epsilon^d_{22}\epsilon^d_{12}\xi_1(\xi_2)^3\Big]\, dV_\xi.
\end{aligned} \tag{A.12}$$

For simplicity, the volume integrals included in (A.12), will be separately evaluated. Since $\underline{\omega}$ is circular, i,j,k and l can have one of two combinations that would not integrate to zero, such as i=j=k=l:

$$\begin{aligned}\int_{\mathcal{H}} \frac{\underline{\omega}\langle\boldsymbol{\xi}\rangle}{|\boldsymbol{\xi}|^2}\xi_1^4\, dV_\xi &= \int_0^\delta\int_0^{2\pi}\int_0^1 \frac{\underline{\omega}}{r^2} r^4\cos^4\theta\, r\, dz d\theta dr \\ &= \int_0^\delta\int_0^{2\pi}\int_0^1 \underline{\omega} r^3\cos^4\theta\, dz d\theta dr \\ &= \frac{3\pi}{4}\int_0^\delta \underline{\omega} r^3\, dr \\ &= \frac{3q}{8}, \end{aligned} \tag{A.13}$$

or i=k=1, j=l=2:

$$\begin{aligned}\int_{\mathcal{H}} \frac{\underline{\omega}\langle\boldsymbol{\xi}\rangle}{|\boldsymbol{\xi}|^2}\xi_1^2\xi_2^2\, dV_\xi &= \int_0^\delta\int_0^{2\pi}\int_0^1 \frac{\underline{\omega}}{r^2} r^2\cos^2\theta\, r^2\sin^2\theta\, r\, dz d\theta dr \\ &= \int_0^\delta\int_0^{2\pi}\int_0^1 \underline{\omega} r^3\cos^2\theta\sin^2\theta\, dz d\theta dr \\ &= \frac{\pi}{4}\int_0^\delta \underline{\omega} r^3\, dr \\ &= \frac{q}{8}. \end{aligned} \tag{A.14}$$

When combining (A.12), (A.13) and (A.14), the peridynamic elastic energy density can be given as:

$$W(\epsilon^d) = \frac{\alpha}{2}\left[\frac{2q}{8}\sum_{i,j=1,2}\epsilon_{ij}^d\epsilon_{ij}^d + \frac{q}{8}\left(\sum_{i=1,2}\epsilon_{ii}^d\right)^2\right] \tag{A.15}$$

and using $\epsilon_{ii}^d = 0$,

$$W(\epsilon^d) = \frac{\alpha q}{8}\epsilon_{ij}^d\epsilon_{kl}^d. \tag{A.16}$$

The elastic strain energy density from the classical theory can be given as:

$$W(\epsilon^d) = \mu\epsilon_{ij}^d\epsilon_{kl}^d, \tag{A.17}$$

and when substituting (A.16) into (A.17), the constant α can be obtained as:

$$\alpha = \frac{8\mu}{q}. \tag{A.18}$$

By substituting (A.18) into (A.8), the scalar state force function for 2D plane strain can now be rewritten as:

$$\underline{t} = \frac{2k\theta}{q}\underline{\omega}\,\underline{x} + \frac{8\mu}{q}\underline{\omega}\,\underline{e}^d, \tag{A.19}$$

where the deviatoric stretch $\underline{e}^d$ can be represented by the stretch $\underline{e}$ (see Figure A.1) and the dilatational stretch $\underline{e}^i$ as:

$$\underline{e}^d = \underline{e} - \underline{e}^i = (\underline{y} - \underline{x}) - \frac{\theta \underline{x}}{2}. \tag{A.20}$$

By substituting (A.20) into (A.19), the scalar state force function can be simplified as a function of the dilatation θ, material parameters, k and μ, as well as, the reference and deformed states $\underline{x}$ and $\underline{y}$.

$$\begin{aligned}
\underline{t} &= \frac{2k'\theta}{q}\underline{\omega}\,\underline{x} + \alpha\underline{\omega}\,\underline{e}^d \\
&= \frac{2k'\theta}{q}\underline{\omega}\,\underline{x} + \alpha\underline{\omega}\left[(\underline{y} - \underline{x}) - \frac{\theta\underline{x}}{2}\right] \\
&= \frac{2k'\theta}{q}\underline{\omega}\,\underline{x} - \alpha\underline{\omega}\frac{\theta\underline{x}}{2} + \alpha\underline{\omega}(\underline{y} - \underline{x}) \\
&= \underline{\omega}\theta\underline{x}\left(\frac{2k'}{q} - \frac{\alpha}{2}\right) + \alpha\underline{\omega}(\underline{y} - \underline{x}) \\
&= \underline{\omega}\theta\underline{x}\left(\frac{2k'}{q} - \frac{4\mu}{q}\right) + \frac{8\mu\underline{\omega}}{q}(\underline{y} - \underline{x})
\end{aligned} \tag{A.21}$$

References

Alder, B. J. and Wainwright, T. E. (1959), 'Studies in molecular dynamics. i. general method', *J. Chem. Phys* .

Anderson, T. L. (2000), *Fracture Mechanics Fundamentals and Applications*, second edn, CRC Press, Inc.

Asadi, S., Javan, M. M., Bohloli, B. and Mutabashiani, S. (2013), 'Experimental, numerical and analytical investigation the initiation and propagation of hydraulic fracturing (case study: Sarvak lime stone)', *World Applied Sciences Journal* **22**(5), 637–646.

ASTM E 399 (2009), Standard test method for linear-elastic plane-strain fracture toughness kic of metallic materials, Technical report, American Society for Testing and Materials.

Atkinson, B. K. (1991), *Fracture Mechanics of Rock*, Acedemic press geology, Acedemic Press, London.

Bavier, E., Hoemmen, M., Rajamanickam, S. and Thornquist, H. (2014), Amesos2 and belos: Direct and iterative solvers for large sparse linear systems. Scientific Programming.

Belytschko, T. and Black, T. (1999), 'Elastic crack growth in finite elements with minimal remeshing', *International Journal for Numerical Methods in Engineering* **45**(5), 601–620.

Bobaru, F. and Ha, Y. D. (2011), 'Adaptive refinement and multiscale modeling in 2d peridynamics', *Journal for Multiscale Computational Engineering* **9**(6), 635–659.

Bobaru, F. and Wenke, H. (2012), 'The meaning, selection, and use of the peridynamic horizon and its relation to crack branching in brittle materials', *International Journal of Fracture* **167**, 215–222.

Bobaru, F., Yang, M., Alves, L. F., Silling, S. A., Askari, E. and Xu, J. (2009), 'Convergence, adaptive refinement, and scaling in 1d peridynamics', *Int. J. Numer. Meth. Engng.* **77**, 852–877.

Branch, T., Ritter, O., Weckmann, U., Sachsenhofer, R. F. and Scgilling, F. (2007), The whtehill formation - a high conductivity marker horizon in the karoo basin, Technical report, Geological Society of South Africa.

Brandtzaeg, A. (1927), Failure of material composed of non isotropic elements.

Brenne, S., Moleda, M., Stockhert, F. and Alber, M. (2013), 'Hydraulic and sleeve fracturing laboratory experiments on 6 rock types', *Effective and Sustainable Hydraulic Fracturing* .

Bueckner, H. F. (1958), 'Propagation of cracks and the energy of elastic deformation', *Trans. Am. Soc. Mech. Eng.* **80E**, 1225–1230.

Chen, Z. (2013), 'An abaqus implementation of the xfem for hydraulic fracture problems', *Effective and Sustainable Hydraulic Fracturing* pp. 725–739.

Crouch, S. L. and Starfield, A. M. (1983), *Boundary Element Methods in Solid Mechanics*, George Allen & Unwin Ltd.

Cundall, P. A. (1971), A computer model for simulating progressive, large scale movements in blocky rock systems, *in* 'Proceedings of the International Symposium on Rock Fracture'.

Eringen, A. C., Speziale, C. G. and Kim, B. S. (1977), 'Crack-tip problem in non-local elasticity', *J. Mech. Phys. Solids* .

Evans, I. (1961), 'The tensile strength of coal', *Colliery Engineering* **38**, 428–434.

Geertsma, J. and de Klerk, F. (1969), A rapid method of predicting width and extent of hydraulically induced fractures., Technical report, J Pet Tech.

Griffith, A. A. (1921), 'The phenomenon of rupture and flow in solids', *Phil. Trans. R. Soc. London* **Series A**(221), 163–198.

Ha, Y. D. and Bobaru, F. (2010), 'Studies of dynamic crack propagation and crack branching with peridynamics', *International Journal of Fracture* **162**, 229–244.

Ha, Y. D. and Bobaru, F. (2011), 'Characteristics of dynamic brittle fracture captured with peridynamics', *Engineering Fracture Mechanics* **78**, 1156–1168.

Henke, S. F. and Shanbhag, S. (2014), 'Mesh sensitivity in peridynamic simulations', *Computer Physics Communications* .

Hestenes, M. R. and Stiefel, E. (1952), 'Methods of conjugate gradients for solving linear systems', *Journal of Research of the National Bureau of Standards* **49**(6), 409–436.

Hilleborg, A., Modeer, M. and Peterson, P. (1976), 'Analysis of crack formation and crack growth in concrete by means of fracture mechanics and finite elements', *Cem Conc Res* .

Hoagland, R. G., Hahn, G. T. and Rosenfield, A. R. (1973), 'Influence of microstructure on fracture propagation in rock', *Rock Mechanics* .

Horsrud, P. (2007), Estimating mechanical properties of shale from empirical correlations, Technical report, SPE Drilling and Completion.

Inglis, C. E. (1913), 'Stresses in a plate due to the presence of cracks and sharp corners', *Trans. Institute Naval Architects* **LV**, 219–230.

Ingraffea, A. R., Heuze, F. and Ko, H. Y. (1976), 'Fracture propagation in rock: Laboratory tests and finite element analysis', *Proc. 17th U.S. Symposium on Rock Mechanics, Snowbird, Utah* pp. 5C4 – 1, 5C4 – 6.

Irwin, G. R. (1957), 'Analysis of stresses and strains near the end of a crack.', *J. Appl. Mech.* **24**, 361.

Israelachvili, J. N. (1992), *Intermolecular and Surface Forces*, second edn, Academic Press.

Jo, H. and Hurt, R. (2013), 'Testing and review of various displacment discontinuity elements for lefm crack problems', *Effective and Sustainable Hydraulic Fracturing* pp. 831–853.

Kazerani, T. (2011), Micromechanical Study of Rock Fracture and Fragmentation under Dynamic Loads using Discrete Element Method, PhD thesis, Swiss Federal Institute of Technology at Lausanne, Batiment GC DI-414, Station 18, 1015, Lausanne, Switzerland.

Kilic, B. (2008), Peridynamic theory for progressive failure prediction in homogeneous materials, PhD thesis, University of Arizona.

Kilic, B. and Madenci, E. (2010), 'An adaptive dynamic relaxation method for quasi-static simulations using the peridynamic theory', *Theor. Appl. Fract. Mech.* **53**, 194–201.

Kunin, I. A. (1983), Elastic media with microstructure ii: three-dimensional models, Berlin.

Le, Q. V., Chan, W. K. and Schwartz, J. (2014), 'A two-dimensional ordinary, state-based peridynamic model for linearly elastic solids', *Int. J. Numer. Meth. Engng* .

Machala, M., Drylie, S. and Keller, M. E. (2012), Leveraging experience to make the extraordinary ordinary: Hydraulic fracturing tight gas under hpht conditions, Technical report, Halliburton.

Madenci, E. and Oterkus, E. (2014), *Peridynamic Theory and Its Applications*, Springer.

Mitchell, J. A. (2011*a*), A nonlocal, ordinary, state-based plasticity model for peridynamics., SAND Report 2011-3166, Sandia National Laboratories, Albequerque, NM and Livermore, CA.

Mitchell, J. A. (2011*b*), A nonlocal, ordinary, state-based viscoelasticity model for peridynamics., SAND Report 2011-8064, Sandia National Laboratories, Albequerque, NM and Livermore, CA.

Montgomery, C. T. and Smith, M. B. (2010), Hydraulic fracturing, history of an enduring technology, *in* 'JPT', pp. 22–40.

Rashid, Y. R. (1968), 'Ultimate strength analysis of pre-stressed concrete pressure vessels', *Nuclear Engineering and Design* .

Rogula, D. (1983), Nonlocal theory of material media, Berlin.

Rummel, F. and Winter, R. B. (1982), Application of laboratory fracture mechanics data to hydraulic fracturing field tests, *in* 'Hydraulic Fracture and Geothermal Energy', 1st Japan-USA Symp., Sendai, Japan, pp. 495–501.

Saad, Y. and Schultz, M. H. (1986), 'Gmres: A generilazed minimal residual algorithm for solving nonsymetric linear systems', *SIAM J. Sci. Stat. Comput.* .

Seleson, P., Parks, M. L., Gunzburger, M. and Lehoucq, R. B. (2009), 'Peridynamics as an upscaling of molecular dynamics', *Multiscale Model. Simul.* pp. 204–227.

Silling, S. A. (2000), 'Reformulation of elasticity theory for discontinuities and long-range forces', *Journal of the Mechanics and Physics of Solids* **48**, 175–209.

Silling, S. A. and Askari, E. (2005), 'A meshfree method based on the peridynamic model of solid mechanics', *Computers and Structures* **83**, 1526–1535.

Silling, S. A., Epton, M., Weckner, O., Xu, J. and Askari, E. (2007), Peridynamic states and constituive modeling., Technical report, Sandia National Laboratories, Albuquerque, New Mexico, USA.

Silling, S. A. and Lehoucq, R. B. (2010b), Peridynamic theory of solid mechanics, Technical report, Sandia National Laboratories.

Silling, S. A., Weckner, O., Askari, E. and Bobaru, F. (2010a), 'Crack nucleation in a peridynamic solid', *Int J Fract* **162**, 219–227.

Stow, D. A. V. (2005), *Sedimentary Rocks in the Field*, 1st edn, Burlington, M.A.: Academic Press.

Turner, D. Z. (2012), mingus. Sandia Corporation.

Turner, D. Z. (2013), 'A nonlocal model for fluid-structure interaction with applications in hydraulic fracturing', *International Journal for Computational Methods in Engineering Science and Mechanics* .

Underwood, P. (1983), 'Dynamic relaxation', *Comput. Meth. Trans. Anal.* .

Weber, N., Siebert, P., Willbrand, K., Feinendegen, M., Clauser, C. and Fries, T. P. (2013), 'The xfem with an explicit-implicit crack description for hydraulic fracture problems', *Effective and Sustainable Hydraulic Fracturing* pp. 711–723.

Westergaard, H. M. (1939), 'Bearing pressures and cracks', *Journal of Applied Mechanics* **6**, 49–53.

Whittaker, B. N., Singh, R. N. and Sun, G. (1992), *Rock Fracture Mechanics*, Elsevier Science Publishers, Sara Burghartstraat 25, Amsterdam, The Netherlands.

Williams, M. L. (1957), 'On the stress distribution at the base of a stationary crack', *Journal of Applied Mechanics* **24**, 109–114.

Xiphu, M. (2011), Petroleum potential of the karoo basin, Technical report, Petroleum Agency of South Africa.

Zhang, X., Lu, M. W. and Wegner, J. L. (2000), 'A 2-d meshless model for jointed rock structures.', *International Journal for Numerical Methods in Engineering* **47**(10), 1649–1661.